Ultrasonic Processing of Aluminum Alloys

Liang Zhang

Ultrasonic Processing of Aluminum Alloys

Proefschrift

ter verkrijging van de graad van doctor
aan de Technische Universiteit Delft,
op gezag van de Rector Magnificus prof. ir. K.C.A.M. Luyben,
voorzitter van het College voor Promoties,
in het openbaar te verdedigen op woensdag 13 maart 2013 om 15.00 uur

door

Liang Zhang
Master in Materials Science and Engineering
University of Science and Technology Beijing, China
geboren te JiangXi , China

Dit proefschrift is goedgekeurd door de promotor:
Prof. ir. L. Katgerman
Prof. dr. D. G. Eskin

Samenstelling promotiecommissie:

Rector Magnificus,   voorzitter
Prof. ir. L. Katgerman,   Technische Universiteit Delft, promotor
Prof. dr. D. G. Eskin,   Brunel University, U.K., promotor
Dr. A. Miroux,   Materials Innovation Institute
Prof. M. R. Jolly,   Cranfield University, U.K.
Prof. L. Zhuang,   University of Science and Technology Beijing, China
Dr. R. Sauermann,   Aleris Rolled Products, Germany
Prof. dr. I. M. Richardson,   Technische Universiteit Delft
Prof. dr. ir. J. Sietsma,   Technische Universiteit Delft, reservelid

Keywords: Ultrasonic processing, Solidification, Aluminum alloys, Microstructure, Casting properties

Contents

Chapter 1

Introduction

1.1 Aluminum alloys and their casting

Nowadays, aluminum alloys are not strange and mysterious materials in our daily life. They are widely used in many fields due to their good corrosion resistance, low density, high strength-to-weight ratio and high fracture toughness [1, 2]. Depending on the alloying elements added to aluminum, different types of aluminum alloys can be obtained, each of them having their own superior performance in many specific areas. For instance, Al-Cu alloys of the 2xxx series and Al-Zn-Mg-Cu alloys of the 7xxx series are usually used in aerospace industry because of the relatively high strength. Al-Mg alloys of 5xxx series with good corrosion resistance are very suitable for applications in corrosive atmospheres, e.g. construction and shipbuilding. Al-Si casting alloys and Al-Mg-Si alloys of 6xxx series are widely used in automotive industry due to their good castability, welding ability and mechanical properties.

The demand for aluminum alloys is still growing. But more importantly, it is accompanied by an increasing requirement for properties of aluminum products. Although several techniques related to deformation processing and heat treatment are developed to meet more and more stringent property requirements, the most important premise for applying these techniques is a high initial quality of as-cast products. Therefore, a perfect casting without defects has been the goal of engineers and foundry workers now, as it was for centuries.

Aluminum casting can be generally classified as shape casting or ingot/billet casting. Shape casting, such as pressure-assisted die casting, investment casting and gravity casting, is used for producing shaped components. Ingot casting mainly produces ingot or billet for further deformation processing, for instance, extrusion, stamping, or rolling .etc. The most common used ingot casting technology is direct chill casting (DC casting).

Several types of casting defect can occur when casting is preformed improperly in both shape casting and ingot casting, for instance, cracking, macrosegregation and porosity. These defects are detrimental to the properties of as-cast products, as well as the quality of semi- or finished products during further deformation. Therefore, the casting properties of aluminum alloys are crucial to determining the final quality of aluminum alloy products.

1.2 Casting properties of aluminum alloys

1.2.1 Microstructure

Microstructure control in aluminum casting has been a topic of study for many decades. The size and distribution of primary intermetallics, dendrite cell size or dendrite arm spacing, equiaxed grain size and occurrence of columnar grains are crucial for determining the final quality of casting products [3, 4].

Among these microstructural features, grain structure is of great importance, since the yield strength is directly related to the final grain structure of alloys [5]. In addition, a fine and uniform distribution of equiaxed grains is well known to benefit many other mechanical and technological properties of aluminum alloys, such as increasing fracture toughness and ductility, as well as improving the casting quality by minimizing shrinkage, hot tearing and

segregation [6, 7]. This is why many techniques of grain refinement have been developed for industrial application.

Generally, several factors affect grain structure of aluminum alloys through either influencing nucleation or growth of solid phases during solidification. One of well known factors is the presence of substrate particles in the melt, which either are deliberately introduced or are naturally present. In order to obtain a good effect of grain refinement in aluminum alloys, the melt is usually populated with substrates by the addition of chemical inoculants through Al-Ti-B and Al-Ti-C master alloys [6, 8], or by the fragmentation of primary dendrites and intermetallics induced by physico-mechanical methods, the most common of which are electromagnetic stirring [9, 10] and ultrasonic melt treatment [11, 12]. These particles might be able to act as nucleation sites for α-Al grains during solidification under the proper casting condition, and result in a uniformly fine, equiaxed grain structure.

Whether these particles can promote nucleation and growth of the solid phase, and thus create a good grain refinement effect, depends on the type and geometry of these particles, as well as on the temperature (undercooling) during solidification [13]. Firstly, the particles should have relatively good heterogeneous nucleation potency for the growing metal matrix. A small crystallographic registry between the nucleate particles and metal matrix is necessary for refinement. Secondly, the number of the particles should be sufficient in order to provide enough substrates, because the efficiency of deliberately added particles is usually very low under typical casting conditions [14]. The increasing number of particles in the melt usually results in a better grain refinement effect. Last but not least, the undercooling during solidification should be large enough to activate these particles as nucleation sites. According to the athermal heterogeneous nucleation theory, as the temperature decreases, the solid begins to form on the substrate particles and continue to grow along the substrate until the solid phase reaches the edge of the particle [15]. At this stage, the curvature of solid approaches the critical value R, where R is the radius of the particle. The geometrically limited undercooling ΔT_g, corresponding to a wetting angle of 90 degree, is given by

$$\Delta T_g = \frac{4\Gamma_{sl}}{R},$$ (1.1)

where Γ_{sl} is the Gibbs–Thomson coefficient between the stable embryo of the solid phase and the liquid, and does not depend on the particle. For Al, Γ_{sl} is 9.12×10^{-8} K m [15]. If undercooling is larger than ΔT_g, this solid can grow past the maximum curvature given by R. Otherwise, the solid embryo will stop at the edge of the substrates as further growth of the solid leads to a decrease in the curvature. The growth of this solid will continue if the undercooling becomes larger than ΔT_g. Thus, the undercooling of the melt to a lower temperature increases the number of effective nuclei, results in decreasing of grain size.

Typically, a higher undercooling can be achieved by higher cooling rate during casting, and also by the segregation of the solute in the melt during the solidification, which is called constitutional undercooling. This effect on grain refinement, which can be quantified by the growth restriction factor (GRF) Q, is another important factor for controlling the as-cast grain structure in aluminum alloy [16-19].

Generally, GRF represents the segregating power of all elements during solidification in the alloy. These segregating elements change the concentration in the liquid phase at the solid/liquid interface beyond the equilibrium concentration according to the phase diagram, preventing its further growth and, at the same time, lead to the formation of a constitutionally undercooled zone in front of the interface, which might activate the potent nucleants present there [16-19]. GRF Q is defined as $\sum_i m_i C_{0,i} (k_i - 1)$, where for each i element, m is the liquidus gradient, C_0 is the bulk alloy composition of the alloy, and k is the partition coefficient (C_S/C_L, where C_S and C_L are the compositions of the solid and liquid phases in the equilibrium). The segregation power of some common elements in aluminum was summarized in Refs [20, 21].

Through GRF Q, a simple relation between as cast grain size d and the alloy composition for a constant set of casting conditions is suggested by Easton and StJohn [22-24] as

$$d = a + \frac{b}{Q} , \tag{1.2}$$

The constant a is related to the maximum number of particles which are active nucleants and the gradient b determines the nucleant potency of the particles in the melt.

1.2.2 Macrosegregation

Macrosegregation is one of the major and irreversible defects in large castings and ingots, because this variation in composition ranges in scale that can reach meters and can not be mitigated through processes after solidification is completed [25, 26]. The change of concentration of alloying elements throughout the cross section of the billet/ingot results in thermal and mechanical properties variation, which impairs the quality of final products [26, 27].

The fundamental reason for macrosegregation is the partitioning of solute elements between liquid and solid phases during solidification [7, 25, 26]. The partition coefficient k, C_S/C_L, as we mentioned in previous section, is an indicator of segregation tendency of the alloying element. The farther this ratio from 1, the more sever the segregation of elements becomes. Most alloying elements in aluminum alloys have a lower solubility in the solid than in the liquid phase ($k<1$). Therefore, during solidification, these elements are rejected into the liquid phase. Subsequently, the relative movement of segregated liquid and solid during solidification results in the macrosegregation [26, 28, 29].

Besides the type of alloying elements, the degree of macrosegregation is also significantly controlled by process parameters and structures in aluminum alloys. Consider the major technology DC casting for instance. The casting speed [30-34], melt superheat [31, 32], billet/ingot dimensions [35-37], metal feeding system [38-40] and grain refiner [39, 41-44] all influence the degree of macrosegregation in DC casting. Generally, reducing the casting speed, limiting the size of billet/ingot and optimizing melt distribution system are known to have a good effect on the alleviation of macrosegregation, while the reports on the effect of melt superheat and grain refiner are sometimes contradicting.

To further understand how these parameters affect the macrosegregation in DC casting, three main relative movements between solid and liquid phase have to be considered. Here we distinguish the mushy and slurry zones as the two parts of the transition region during solidification corresponding to the different stages of solidification in DC casting of aluminum alloy. The border between the two zones is the coherency isotherm. The condition of coherency can be defined as the moment when solid grains begin to interact with each other [45]. The slurry zone is the region between liquidus and coherency isotherm, where solid grains float freely. The region between coherency isotherm and solidus is called the mushy zone, where the macroscopic movement of solid grains is fully restricted.

The first type of relative movement of the solid and liquid phases is the convection flow in the liquid and slurry zones of the casting, such as thermosolutal convection due to temperature and concentration gradients, which usually promotes the positive centerline segregation [28, 29, 46] and forced melt flow (e.g. pouring, stirring) [47, 48].

The second one is shrinkage-driven flow in the mushy zone. This flow is due to the pressure difference over the solidifying layer of the mushy zone and results in the negative centerline segregation [40, 49].

The third one is the movement and sedimentation/growth of solid fragments, which is usually called 'floating' grains. These solute-depleted grains accumulate in the center and usually promote the negative centerline segregation [32, 38, 50].

The final macrosegregation pattern observed in real casting billet/ingot is, therefore, a result of the combination of these relative movements of solid and liquid phases, which is affected by process parameters and structures in aluminum alloys.

1.2.3 Solidification shrinkage and thermal contraction

As one of the main features during casting, the contraction of aluminum alloys during and after solidification has a decisive effect on the quality of casting products. After being poured into the mold, the melt starts to shrink in the liquid state due to the falling temperature. This liquid shrinkage is usually not troublesome while the whole volume is liquid, because the compensation for this contraction by liquid melt is done without any difficulty [51].

As cooling progresses and the melt starts to solidify, the further shrinkage mainly comes from the solidification due to the density difference of liquid and solid phases. This is known as the solidification shrinkage. The crystal structure of alloys plays here an important role [52]. Usually, metals with densest crystal structure, such as faced-centered cubic (FCC) structure (e.g. Al and Cu) and hexagonal close packing (HCP) structure (e.g. Mg and Zn) have larger values of solidification shrinkage than metals with less closely packed body-centered cubic (BCC) structure (e.g. Fe). The temperature dependence of the density of liquid and solid phases also contributes to the reduction of volume but to a much less extend than the solidification shrinkage.

After solidification, the temperature dependence of the density of solid phase results in further contraction, which is called thermal contraction. Schematic illustration of these three shrinkage/contraction regimes is shown in Fig.1.1.
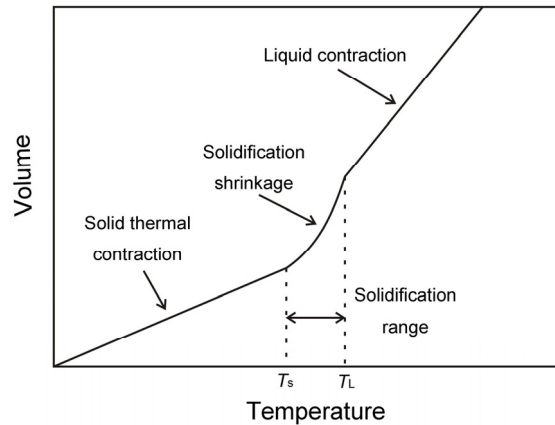
Figure 1.1 Schematic illustration of the three contraction regimes: in the liquid; during solidification; and in the solid [52].

In the early stage of solidification, where the rigid skeleton of solid phases is not formed, the thermal shrinkage can not manifest itself as the horizontal contraction of the casting and cause large problems. All volumetric changes appear as the decreasing level of the melt in the permanent mould or do not appear at all during DC casting, due to the continuous supply of the melt to the mould. However, several contraction defects can arise in the lower part of the solidification range. Most of defects occur in this stage from the failure of the liquid to compensate for the contraction, and sometimes also from the inability of the materials to withstand the development of stress/strain after the rigidity point, where a continuous dendrite network is formed [29, 53]. Among these defects related to contraction, the most common and harmful defects are shrinkage porosity and hot tearing, which usually happen close to the solidus, when the solid fraction is more than 0.9 [51, 54]. In this stage, the failure of interdendritic feeding results in the formation of distributed voids or microshrinkage between dendrite arms. Moreover, the large volume of contraction of aluminum alloys, combined with the extreme weakness of the dendrite network close to the solidus, makes hot tearing easy to occur [25].

As just mentioned above, two crucial factors cannot be ignored when considering the hot tearing susceptibility of aluminum alloys. The first one is contraction behavior in 'the vulnerable part of the solidification interval' during solidification, between the rigidity temperature and the solidus [54, 55]. Another is feeding ability of liquid, which can also be represented by the permeability of the mushy zone. In order to reduce the hot tearing tendency, a smaller concentration of stress/strain caused by contraction, or a smaller vulnerable solidification interval is required, as well as a better permeability of the mushy zone. Thus, the composition of alloys plays an important role in affecting the hot tearing susceptibility [55-63], since it does not only influence the solidification interval, but also

6

determines the fluidity of the liquid in this temperature range [64]. Usually, alloys with very short solidification range, including pure Al and those of near eutectic composition, show shorter vulnerable solidification interval and better liquid feeding ability (fluidity), thus, little tearing tendency. Alloys containing small amount of eutectic, with relative larger solidification range, inversely, are prone to tear [25].

Beside the composition, the cooling rate, casting temperature and temperature distribution also affect the hot tearing tendency. A lower cooling rate is reported to promote better feeding, and then reduce hot tearing susceptibility [65]. A higher casting temperature, usually, results in the coarsening of grain structure. As a consequence, on one hand, it increases the rigidity temperature, enlarging the vulnerable solidification interval. On the other hand, the coarsening of grain structure also means relative low tensile strength and ductility of a semisolid alloy. Thus, a high casting temperature usually leads to a larger hot tearing susceptibility [59]. However, the improvement of feeding ability caused by increasing casting temperature is also reported to inhibit the formation of hot tearing due to a better feeding of the melt [29]. Temperature distribution during solidification governs the distribution of mechanical properties and at the same time creates the pattern of stress-strain relationships due to differential contraction [25]. Tears are often located at changes in cross-section, where stress concentration is associated with locally delayed or accelerated cooling [25].

Some particles presented in the melt can induce hot tearing as well. The oxides particles or intermetallics formed during solidification potentially provide favorable locations for crack initiation and propagation [66]. In addition, these particles might block the feeding channels, thus reduce the permeability of the mushy zone, and initiate the hot tearing [67].

1.2.4 Fluidity

In aluminum shape casting, the term fluidity is most widely recognized to describe the ability of liquid metal to flow through mould passages and to fill all the interstices of the mold, providing sharp outlines and faithful reproduction of design details [25]. Thus, the fluidity of aluminum melt after pouring into the mold is crucial to determine whether the cast product will be properly formed, internally sound and free from defects.

In order to quantify the fluidity, a large number tests have been used, such as the spiral mould test [25, 51], the vacuum fluidity test [25, 51] and strip mould test [68]. Common to all tests is that the molten metal has to flow into a narrow channel. The measurement of the length in the channel filled by metal stream before it solidifies is usually used to represent the fluidity of molten metal.

Generally, the intrinsic fluid properties of the molten metal, such as viscosity, surface tension, thermal conductivity, specific heat, determine the fluidity of molten metal [69]. However, these physical properties are hard to obtain and use during real casting processes to estimate the fluidity. Therefore, in aluminum casting, the reported factors affecting the fluidity are mainly focused on the real casting parameters and the quality of the melt.

To understand how these factors influence the fluidity in aluminum casting, let us first have a look at the characteristic modes of solidification in the channel of a testing mold [7, 25, 51]. For alloys with planar solidification front from the mold wall (e.g. columnar structure),

as illustrated in Fig.1.2 (a), the stream can continue to flow in the channel until the moment when the opposing freezing fronts meet. In this case, almost 100% solidification is needed at one location for the flow to stop and usually this location is found near to the point of entry. When the crystallization become independent (e.g. equiaxed structure), as shown in Fig.1.2 (b), the flow of the melt is restricted by the growing of free crystals at the tip of the stream. When the grains start to impinge on each other at 40-60% solid fraction, the tip area stiffens, which provides the resistant to flow.
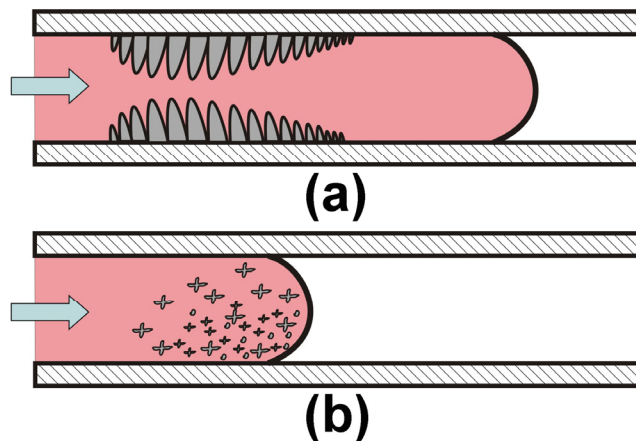
Figure 1.2 Flow and solidification of aluminum alloy in a fluidity channel: (a) alloys with planar solidification front from the mold wall (e.g. columnar structure); and (b) alloys with independent growing crystals (e.g. equiaxed structure). Modified from [7, 25, 51].

Due to these different modes of solidification, the composition is one of the major factors affecting the fluidity, since it determines the mode of solidification [3, 7, 51, 70, 71]. High fluidity is commonly found to be associated with pure metals and with the alloys of eutectic composition. A large solidification range results in a poor fluidity.

The effect of grain refiner on fluidity has two sides [72-77]. On one hand, the transition of columnar structure to equiaxed structure caused by grain refiner strongly decreases the fluidity of molten metal, as illustrated in Fig.1.2. However, further addition of the grain refiner results in the refinement of equiaxed grains. As a consequence, a higher solid fraction is required for the impingement of the equiaxed grains, thus, causing the increase in the fluidity.

The melt superheat and the quality of the melt also influence the fluidity of aluminum melt. A higher melt superheat is reported to cause a better fluidity due to the delayed onset of solidification [78, 79]. A good quality of the melt is important for increasing the fluidity of molten metal. Oxide films formed on the surface of aluminum melt and oxide inclusions in the melt can significantly raise surface tension and reduce the ability of molten metal to fill finer details in the shape casting [77, 80].

Apart from metal characteristics, the nature of the mold plays a key role in the fluidity of aluminum melt as well in the shape casting. Molds with lower heat diffusivity usually result in a better fluidity [81]. Similarly, the use of a preheated mold reduces the rate of heat removal, thus, increases the fluidity of molten metal [82]. Other mold characteristics, such as the roughness of the surface, coating on the mold are also reported to affect the fluidity. A smooth surface increases the fluidity through reducing frictional forces. A proper coating of the mold usually provides a positive effect on fluidity [83]. However, in the sand casting, the coating might also reduce the permeability of the mold, which causing the decrease of the fluidity [84].

1.2.5 Hydrogen Porosity

The formation of porosity during and after solidification in aluminum alloys is one of the major defects and detrimental to mechanical properties [25, 51]. The dissolved hydrogen (atomic H) in molten melt is considered as the main source of porosity in aluminum alloys [85]. During solidification, most of the dissolved hydrogen precipitates in molecular form due to the significant difference in hydrogen solubilities in liquid and solid aluminum, and then facilitates pore formation in aluminum alloys.

Four stages of hydrogen precipitation during solidification are summarized as follows [85]: (1) diffusion of hydrogen atoms within the molten pool; (2) formation of sub-critical nuclei as a function of time and cooling; (3) random emergence of stable precipitates that exceed the critical size required for sustained growth; and (4) continued growth as long as dissolved hydrogen atoms remain free to diffuse to the precipitated bubble. The final formation of hydrogen porosity is due to bubbles being trapped during solidification or to hydrogen filling and expanding shrinkage cavities.

Therefore, the hydrogen solubility in molten Al alloys is the major parameter determining the porosity. Every factor which results in the increasing hydrogen solubility or in creating a source of hydrogen will increase the initial content of hydrogen in the melt, thus increase the porosity. Among these factors are a higher melt superheat [86], more surface active alloying elements (e.g. Mg or Li, relative to non-surface active elements Cu, Zn and Si .etc.) in the melt [86-89] and a humid environment. Lower liquid cooling and solidification rates also increase the hydrogen pore volume fraction and size due to enhanced diffusion of hydrogen atoms [85]. High cooling rate may result in the formation of supersaturated hydrogen solution in solid aluminum. This hydrogen can then precipitate and form so-called secondary porosity in the solid phase.

In order to minimize the detrimental effect caused by hydrogen porosity defects, degassing processing is necessary in industrial aluminum castings. The most common method is the introduction of additional bubbles into the melt through injecting inert gas (such as Argon or Nitrogen) using lances, nozzles, porous plugs or rotors [90-92]. The formed hydrogen-free bubbles promote the diffusion of hydrogen from the molten aluminum into the bubbles due to a lower partial pressure of hydrogen inside. These bubbles float up and escape from the melt, which results in the removal of hydrogen. Vacuum degassing also can be used in aluminum melts [93, 94], however, due to high technical requirements and cost it is rarely applied in industry.

1.3 Ultrasonic processing

The research in ultrasonic processing for metallurgical application can be dated back to the 20th century. As early as in the 1930-1960s, several successful attempts were made using high-frequency ultrasound during casting processing by Seemann et al. in Germany [95], Eskin [11, 96, 97] and Abramov [12] in the Soviet Russia. The main reported benefits caused by high-power ultrasonics range from the suppression of columnar grain structure and grain refinement, to increasing homogeneity and reducing segregation, and also include melt degassing. These promising effects strongly reflect the features of ultrasonic waves in liquid metals.

1.3.1 Background of ultrasonic processing in liquid metals

The basic principle of ultrasonic processing/ultrasonic melt treatment (UST) for metallurgical application is introduction of acoustic waves with a frequency higher than 17 kHz into liquid metal. During ultrasonic processing, ultrasonic tool (sonotrode) must contact directly with the liquid metals since the ultrasonic waves are stress waves, which can only exist and transmit between the masses [98].

The most important and well-known phenomena during the propagation of high-frequencies ultrasonic waves in melts is cavitation. In an external ultrasonic field, gas cavities are produced at several weak sites, which are called 'cavitation nuclei', such as interfaces and pre-existing gas pockets, for instance, hydrogen in aluminum alloys [11, 12]. These bubbles grow during the negative pressure portion of the sound field, and collapse during intervals of increased pressure if the acoustic intensity is sufficiently high. The implosion of the bubbles results in intense local heating and high pressures with very short lifetimes, as well as violent liquid jets. It was reported that the pressure of hydraulic shock waves generated from the collapse may reach tens of thousands of MPa [11, 99, 100]. The temperature in cavities at the point of collapse may increase up to 1000 ˚C [101] and even up to the temperatures of the order of 10000 ˚C from calculations [102].

Another important feature of UST is acoustic streaming. The origin of streams relates to the ultrasonic momentum acquired by the liquid when it absorbs the wave [11]. These hydrodynamic flows occur both in the bulk of the liquid and near the walls, particles and other objects within oscillating ultrasonic fields [11]. The presence of these streams in the melt, on one hand, increases the homogeneity of the melt. On the other hand, they also influence the temperature distribution in a liquid bath.

1.3.2 Application of ultrasonic processing in casting

Numerous works on the application of high-power ultrasound in casting have been reported. The most well-known effect caused by ultrasonic processing is grain refinement. It was reported by several researchers that when ultrasonic processing was applied in liquid or semi-liquid metals, a significant refinement of grains can be achieved, as well as suppression of columnar grain structure and formation of globular grain structure. The suggested mechanisms range from affecting nucleation through local undercooling and wetting (activation) of substrates to fragmentation and transport of dendrites or primary intermetallics. The detail mechanisms are summarized in Table 1.1.

Through the summary in Table 1.1, one can clearly see that at least five mechanisms were proposed to explain the ultrasonic-aided grain refinement. Indeed, the behavior of liquid under cavitation is complex and difficult to study, especially in non-transparent liquid metals. The dominating mechanism of grain refinement depends on the stage where ultrasonic processing is applied (liquid stage or solidification range). In addition, these mechanisms have different grain refining abilities. For instance, the application of ultrasonic processing only in the liquid stage usually results in a limited grain refining effect, while a significant grain refinement can be achieved when it is applied in the solidification range [103]. Thus, the ultrasonic-aided grain refinement usually is considered to be the result of combination of several different mechanisms.

Ultrasonic processing is also used for other structural refinement, such as refinement of eutectic phases/primary particles in Al-Si based alloys [101, 104-112], and modification of the distribution/morphology of Al_3Ti/TiB_2 phases in an Al-Ti-B master alloy [113]. The reported data and mechanisms are summarized in Table 1.2.

Ultrasonic degassing is another well-known effect for metallurgical application in aluminum castings. Eskin reported that the cavitation treatment halved the content of hydrogen from 0.6 to 0.3 cm^3 per 100 g in an Al-6 wt% Mg alloy [114]. Similar results were also found by Abramov [12], Wu et al. [115], Puga et al. [116, 117], NajiMeidani et al. [118] and Xu et al. [119, 120]. The commonly accepted mechanism is a process of three simultaneous stages [11, 12]: (1) the diffusion of dissolved gas to the ultra fine bubbles existing in the liquid; (2) the coalescence of fine bubbles as result of acoustic streaming, radiation pressure, as well as Bjerknes and Bernoulli forces; and (3) floating up of large bubbles with the help of the action of Stokes forces and acoustic flows.

Therefore, the efficiency and effectiveness of ultrasonic degassing strongly depend on ultrasonic processing temperature [117, 120], treated melt volume [117, 119, 120] and ultrasonic power [117]. It is also reported that the combination of other degassing technologies with ultrasonic degassing, such as combination with vacuum treatment or argon degassing, resulted in a better degassing effect in aluminum melt as compared to a single degassing method [114, 119, 121].

Ultrasonic processing can also used for alleviating macrosegregation during DC casting. It was reported that a relative uniform distribution of main alloying elements over the ingot cross section can be achieved by applying ultrasonic processing in 112-mm and 270-mm ingots for AA7055 alloy [11]. It was explained by the change in crystallization caused by cavitation in molten metal. However, the detailed mechanism is still unclear.

Table 1.1 The summarized mechanisms of ultrasonic-aided grain refinement

Reported effect	Suggested mechanisms	Major applicable ranges	References
Refinement of grain structure	Rapidly increase of the size of the bubbles and evaporation of liquid inside the bubbles tend to reduce the bubble temperature, which results in an undercooling of the melt at the bubble surface	Liquid stage/no solid phases requested	[122]
	The increased pressure caused by bubbles collapse leads to an increase of melting point of surrounding liquid, which is equivalent to increased undercooling	Liquid stage/no solid phases requested	[123, 124]
	Cavitation activates insoluble particles (oxides, carbides, etc) existing in the melt and turns them to solidification sites	Liquid stage/ insoluble particles requested	[11, 12]
	Shock waves generated from the collapse of cavities lead to fragmentation of growing dendrites	Solidification range/growing dendrite requested	[12, 95, 102, 125, 126]
	The refined primary intermetallics act during further solidification as nucleation sites for aluminum grains	Solidification range/growing intermetallics requested	[103, 127-129]

Table 1.2 The summarized reported data on structural refinement in Al-Si based alloys and the Al-Ti-B master alloy

Researched objects	Reported effects	Suggested mechanisms	References
Eutectic phases in Al-Si based alloys	Refinement of eutectic phases	Cavitation-assisted fragmentation	[104-106]
	Coarsening of eutectic phases	The introduction of ultrasonic energy into the melt increases somewhat the temperature and effectively decreases the undercooling at the solidification front	[107-111]
Primary phases in Al-Si based alloys	Refinement of primary Si particles	Cavitation-assisted fragmentation	[101, 108, 109, 112]
Al_3Ti/TiB_2 phases in Al-Ti-B master alloy	Uniform distribution of TiAl3 phases and modification of the morphology of TiB_2 agglomeration into loose coral-like, as a result, improved the grain refining performance	Cavitation-assisted fragmentation and acoustic streaming	[113]

This review showed that lots of promising effects are reported on the application of ultrasonic processing in castings. However, the ultrasonic processing is rarely used in industrial productions of aluminum alloys. So what causes this situation? Three factors can be suggested here.

Firstly, the promising effects caused by ultrasonic processing are not fully realized by industries. This is because most of research was at laboratory scale with the use of limited equipment capacity for ultrasonic treatment. Some unsuccessful attempts in industrial

application directly using these laboratory scale setups are not able to attract industry's attention.

The second factor is the lack of a systematic analysis of ultrasonic processing in castings. Although the effect of several parameters of ultrasonic processing and related benefits were reported, the design of experimental setup (magnetostrictive or piezoelectric transducers, design and materials of sonotrode etc.), specific ultrasonic treatment and casting conditions (operational power of generator, selected ultrasonic treatment time, temperature range of UST, ultrasonic treated volume and cooling rate etc.) differ from researcher to researcher, which makes the reported data hardly comparable. In addition, the effect of ultrasonic processing on several important casting properties, such as fluidity of molten melt and contraction behavior during solidification, was rarely studied and reported.

Last but not least, the lack of well understanding of specific mechanisms of the cavitation-aided effects restricts the optimization of ultrasonic processing in industrial application. This is manly due to the complexity of cavitation in liquid metals, and also due to many uncharted and uncontrolled parameters that are involved in casting processing.

Therefore, a systematic analysis of ultrasonic processing in castings and a full understanding of the related mechanisms are necessary to promote further industrial application of ultrasonic processing.

1.4 Thesis objectives and outline

The objective of this thesis is to present a systematic analysis of ultrasonic processing in the casting of aluminum alloys. Experimental studies were preformed in order to improve our understanding of ultrasonic-aided structural refinement in different aluminum alloy systems, ultrasonic processing in DC casting and other casting properties (contraction behavior, fluidity and porosity) under ultrasonic processing. From this understanding a robust process technology is aimed to be developed.

In Chapter 2, the experimental setup used in this research for ultrasonic processing is introduced. This chapter also presents the effect of ultrasonic processing in aluminum alloys containing Zr and Ti. The formation of primary intermetallics under ultrasonic processing is first investigated. Then, in order to study the ultrasonic-aided grain refining effect in the presence of transition metals Zr and Ti, ultrasonic processing is preformed in different temperature ranges (liquid or solidification range), at different concentration of Zr (hyper or hypo-peritectic concentration) and different concentration of alloying elements (Cu, Mg and Zn). Based on these results, the role of solutes and transition metals Zr and Ti on grain refinement is discussed.

In Chapter 3, the effect of ultrasonic processing in several aluminum alloys with eutectic systems is reported. The formation of primary particles and eutectic structures under ultrasonic processing is investigated using binary Al-Mn, Al-Fe, and Al-Si alloys. The grain structure in these alloys under ultrasonic processing is also revealed and discussed. In addition, a commercial Al-Si piston alloy is selected to study the industrial application of ultrasonic processing in commercial aluminum alloys.

In Chapter 4, a systematic analysis of the effects of ultrasonic processing parameters is performed. The power of ultrasonic generator, initial sonotrode temperature, temperature of ultrasonic treatment, holding time after ultrasonic processing and cooling rate during solidification are studied in aluminum alloys containing Zr and Ti. Based on the results, several suggestions are given with respect to the industrial application of ultrasonic processing.

In Chapter 5, results of a preliminary research of ultrasonic processing in DC casting are presented. In order to establish the flow pattern of the melt when passing next to the sonotrode and find favorable conditions for ultrasonic processing in the launder, water modeling using a transparent launder, transparent hot top and ultrasonic equipment is done. Using this result, two DC casting trials using two different setups are preformed under ultrasonic processing. In addition, to analyze the mechanism of ultrasonic processing on macrosegregation in DC casting, an extended research is preformed using different melt feeding schemes in industrial scale DC casting and also through the computer simulation.

In Chapter 6, the effect of ultrasonic processing on thermal contraction during and after solidification is studied. The temperature of the contraction onset, the amount of contraction in the solidification range and thermal contraction coefficient at sub-solidus temperature in ultrasonic treated alloys are measured. The structure-related mechanism on contraction behaviors under ultrasonic processing is discussed.

In Chapter 7, the effect of ultrasonic processing on the fluidity of molten aluminum melt is studied. In addition, a preliminary analysis is preformed to demonstrate the promising degassing effect caused by ultrasonic processing.

In Chapter 8, a summary of the results and the most important conclusions of this thesis are finally presented. Ideas and recommendations for future work are also proposed.

References

[1] http://en.wikipedia.org/wiki/Aluminium_alloy.

[2] L.F.Mondolfo, *Aluminum Alloys: Structure and Properties*. 1976, London: Butter Worths.

[3] V.S.Zolotorevsky, N.A.Belov, and M.V.Glazoff, *Casting Aluminum Alloys* 2007, Oxford: Elsevier Science

[4] R.E.Smallman and R.J.Bishop, *Modern Physical Metallurgy and Materials Engineering*. Sixth Edition ed. 1999, Oxford: Butterworth-Heinemann.

[5] E.O.Hall, *Proc. Phys. Soc. B*, 1951. **64**(9): p. 747-753.

[6] B.S.Murty, S.A.Kori, and M.Chakraborty, *Int. Mater. Rev.*, 2002. **47**: p. 3-29.

[7] M.C.Flemings, *Solidification Processing*. 1974, New York: McGraw-Hill.

[8] T.E.Quested, *Mater. Sci. Technol.*, 2004. **20**: p. 1357-1369.

[9] T.Campanella, C.Charbon, and M.Rappaz, *Metall. Mater. Trans. A*, 2004. **35A**: p. 3201-3210.

[10] C.Vives, *J. Cryst. Growth*, 1998. **158**: p. 118-127.

[11] G.I.Eskin, *Ultrasonic Treatment of Light Alloy Melts*. 1998, Amsterdam: Gordon and Breach Science Publishers.

[12] O.V.Abramov, *Ultrasound in Liquid and Solid Metals*. 1994, Boca Raton,FL: CRC press.

[13] T.E.Quested and A.L.Greer, *Acta Mater.*, 2005. **53**: p. 2683-2692.

[14] I.Maxwell and A.Hellawell, *Acta Metall.*, 1975. **23**: p. 229-237.

[15] J.A.Dantzig and M.Rappaz, *Solidification*. 2009, Boca Raton: CRC Press.

[16] M.A.Easton and D.H.StJohn, *Light Metals 2001*, J.L.Anjier, Editor. 2001, TMS: Warrendale, PA. p. 927-933.

[17] A.L.Greer, P.S.Cooper, M.W.Meredith, W.Schneider, P.Schumacher, J.A.Spittle, and A.Tronche, *Adv. Eng. Mater.*, 2003. **5**: p. 81-91.

[18] T.Chandrashekar, M.K.Muralidhara, K.T.Kashyap, and P.R. Rao, *Int. J. Adv. Technol.*, 2009. **40**: p. 234-241.

[19] T.E.Quested and A.L.Greer, *Acta Mater.*, 2005. **53**: p. 4643-4653.

[20] M.Johnsson and L. Bäckerud, *Z.Metall.*, 1996. **87**(3): p. 216-220.

[21] T.E.Quested, A.T.Dinsdale, and A.L.Greer, *Acta Mater.*, 2005. **53**: p. 1323-1334.

[22] D.H.StJohn, M.A.Easton, P.Cao, and M.Qian, *Int. J. Cast. Met. Res.*, 2007. **20**: p. 131-135.

[23] Easton, M.A. and D.H. StJohn, *Metall. Mater. Trans. A*, 2005. **36A**: p. 1911-1920.

[24] Easton, M.A. and D.H. StJohn, *Mater. Sci. Eng. A*, 2008. **486**: p. 8-13.

[25] P.R.Beeley, *Foundry Technology*. 1972, London: Butterworths.

[26] C.Beckermann, in *ASM Handbook, Volume 15: Casting*, A.I.H. Committee, Editor. 2008, ASM International. p. 348-352.

[27] R.Nadella, D.G.Eskin, Q.Du, and L.Katgerman, *Progr. Mater. Sci.*, 2008. **53**: p. 421-480.

[28] B.C.H.Venneker and L.Katgerman, *J. Light. Met.*, 2002. **2**: p. 149-159.

[29] D.G.Eskin, *Physical Metallurgy of Direct Chill Casting of Aluminum Alloys*. 2008, New York: CRC Press.

[30] D.G.Eskin, Jr.J.Zuidema, V.I.Savran, and L.Katgerman, *Mater. Sci. Eng. A*, 2004. **384A**: p. 232-244.

[31] D.G.Eskin, V.I.Savran, and L.Katgerman, *Metall. Mater. Trans. A*, 2005. **36A**: p. 1965-1976.

[32] R.C.Dorward and D.J.Beerntsen, *Light Metals 1990*, C.M.Bickert, Editor. 1990, TMS: Warrendale,PA. p. 919-924.

[33] V.I.Dobatkin, *Continuous Casting and Casting Properties of Alloys*. 1948, Moscow: Oborongiz.

[34] R.Nadella, D.G.Eskin, and L.Katgerman, *Mater. Sci. Forum*, 2006. **519-521**: p. 1841-1846.

[35] V.A.Livanov, R.M.Gabidullin, and V.S.Shipilov, *Direct-chill Casting of Aluminium Alloys*. 1977, Moscow: Metallurgiya.

[36] S.C.Flood and D.A.Davidson, *Mater. Sci. Technol.*, 1994. **10**: p. 741-751.

[37] D.G.Eskin, Q.Du, and L.Katgerman, *Metall. Mater. Trans. A*, 2008. **39A**: p. 1206-1212.

[38] M.G.Chu and J.E.Jacoby, *Light Metals 1990*, C.M.Bickert, Editor. 1990, TMS: Warrendale,PA. p. 925-930.

[39] B.Gariepy and Y.Caron, *Light Metals 1991*, E.L.Rooy, Editor. 1991, TMS: Warrendale,PA. p. 961-971.

[40] L.Zhang, D.G.Eskin, A.Miroux, T.Subroto, and L.Katgerman, *IOP Conf. Ser.: Mater. Sci. Eng.*, 2012. **33,012019**: p. 1-6.

[41] A.M.Glenn, S.P.Russo, and P.J.K.Paterson, *Metall. Mater. Trans. A*, 2003. **34A**: p. 1513-1523.

[42] G.Lesoult, V.Albert, B.Appolaire, H.Combeau, D.Daloz, A.Joly, C.Stomp, G.U.Grün, and P.Jarry, *Sci. Technol. Adv. Mater.*, 2001. **2**: p. 285-291.

[43] R.Nadella, D.G.Eskin, and L.Katgerman, *Light Metals 2007*, M.Sørlie, Editor. 2007, TMS: Warrendale,PA. p. 727-732.

[44] A.Joly, G.U.Grün, D.Daloz, H.Combeau, and G.Lesoult, *Mater. Sci. Forum*, 2000. **329-330**: p. 111-120.

[45] L.Arnberg, L.Bäckerud, and G.Chai, *Solidification Characteristics of Aluminium Alloys, Vol. 3: Dendrite Coherency*. 1996, Des Plaines,IL: American Foundrymen's Society.

[46] D.G.Eskin and L.Katgerman, *Mater. Sci. Forum*, 2010. **630**: p. 193-199.

[47] D.G.Eskin, A.Jafari, and L.Katgerman, *Mater. Sci. Tech.*, 2011. **27**: p. 890-896.

[48] D.G.Eskin, A.N.Turchin, and L.Katgerman, *Int. J. Cast Metals Res.*, 2009. **22**: p. 99-102.

[49] D.G.Eskin, Q.Du, and L.Katgerman, *Scr. Mater.*, 2006. **55**: p. 715-718.

[50] D.G.Eskin, R.Nadella, and L.Katgerman, *Acta Mater.*, 2008. **56**: p. 1358-1365.

[51] J.Campbell, *Castings*. 1991, Oxford, U.K.: Butterworth-Heinemann.

[52] J.Campbell, *Castings Practice: The 10 Rules of Casting*. 2004, Oxford, U.K.: Butterworth-Heinemann.

[53] D.G.Eskin, Suyitno, and L.Katgerman, *Progr. Mater. Sci.*, 2004. **49**: p. 629-711.

[54] D.G.Eskin, Suyitno, J.F.Mooney, and L.Katgerman, *Metall. Mater. Trans. A*, 2004. **35A**: p. 1325-1335.

[55] W.S.Pellini, *Foundry*, 1952. **80**: p. 125-133,192-199.

[56] S.Lin, C.Aliravci, and M.O.Pekguleryuz, *Metall. Mater. Trans. A*, 2007. **38A**: p. 1058-1068.

[57] T.W.Clyne and G.J.Davies, *Brit. Foundry*, 1975. **68**: p. 238-244.

[58] W.I.Pumphrey and J.V.Lyons, *J. Inst. Met.*, 1947. **74**: p. 439-455.

[59] W.I.Pumphrey and J.V.Lyons, *J. Inst. Met.*, 1948. **74**: p. 439-455.

[60] I.I.Novikov and O.E.Grushko, *Mater. Sci. Technol.*, 1995. **11**: p. 926-932.

[61] P.H.Jennings, A.R.E.Singer, and W.I.Pumphrey, *J. Inst. Met.*, 1947. **74**: p. 227-248.

[62] D.Warrington and D.G.McCartney, *Cast Met.*, 1991. **3**(4): p. 202-208.

[63] G.K.Sigworth, O.Rios, J.Howell, and M.Kaufman, *AFS Trans.*, 2004. **112**: p. 387-408.

[64] K.R.Ravi, R.M.Pillai, K.R.Amaranathan, B.C.Pai, and M.Chakraborty, *J. Alloys Compd.*, 2008. **456**: p. 201-210.

[65] L.Bichler, A.Elsayed, and K.Lee, *Int. J. Metal Cast.*, 2008. **2**(1): p. 43-54.

[66] M.Lalpoor, D.G.Eskin, H.G.Fjær, A.T. Cate, N.Ontijt, and L.Katgerman, *Mater. Sci. Forum*, 2010. **654-656**: p. 1432-1435.

[67] H.Nagaumi, S.Suzuki, T.Okane, and T.Umeda, *Mater. Trans.*, 2006. **47**(11): p. 2821-2827.

[68] M.DiSabatino, L.Arnberg, S.Brusethaug, and D.Apelian, *Int. J. Cast Metals Res.*, 2006. **19**: p. 94-97.

[69] J.R.Davis, ed. *ASM Specialty Handbook: Aluminum and Aluminum Alloys*. 1993, ASM International.

[70] S.Gowri and F.H.Samuel, *Met. Trans. A*, 1994. **25A**: p. 437-448.

[71] G.Lang, *Aluminium*, 1972. **48**: p. 664-672.

[72] A.K.Dahle, P.A.Tondel, C.J.Paradies, and L.Arnberg, *Metall. Mater. Trans. A*, 1996. **27A**: p. 2305-2313.

[73] M.DiSabatino and L.Arnberg, *Int. J. Cast Metals Res.*, 2005. **18**: p. 181-186.

[74] M.Tiryakioglu, D.R.Askeland, and C.W.Ramsay, *AFS Trans.*, 1994. **102**: p. 17-25.

[75] F.R.Mollard, M.C.Flemings, and E.Niiyama, 1987. **95**: p. 647-652

[76] S.Sánchez, E.Velasco, P.D.Zambrano, and J.L.Cavazos, *Mater. Sci. Forum*, 2006. **509**: p. 159-164.

[77] Y.D.Kwon and Z.H.Lee, *Mater. Sci. Eng. A*, 2003. **360**: p. 372-376.

[78] M.DiSabatino, *Fluidity of Aluminum Foundry Alloys*. 2005, Norwegian University of Science and Technology.

[79] K.L.Sahoo and C.S.Sivaramakrishnan, *J. Mat. Proc. Tech.*, 2003. **135**: p. 253-257.

[80] M.DiSabatino and L.Arnberg, *Mater. Sci. Eng. A*, 2005. **413-414**: p. 272-276.

[81] M.C.Flemings, F.R.Mollard, and H.F.Taylor, *AFS Trans.*, 1961. **69**: p. 566-576.

[82] ASM, ed. *Metals Handbook 4th Ed. Properties and Selection: Non-ferrous Alloys and Pure Metals*. Vol. 12. 1979, ASM. 164-165.

[83] N.Eisuke and A.Koichi, *J. Mat. Proc. Tech.*, 1997. **63**: p. 779-783.

[84] M.Divandari, V.Jamali, and S.G.Shabestari, *Int. J. Cast Metals Res.*, 2010. **23**: p. 23-29.

[85] J.G.Kaufman and E.L.Rooy, *Aluminum Alloy Casting: Properties,Processes, and Applications*. 2004, Materials Park, OH: ASM International.

[86] P.N.Anyalebechi, D.E.J.Talbot, and D.A.Granger, *Metall. Mater. Trans. B*, 1988. **19B**: p. 227-232.

[87] P.N.Anyalebechi, *Scripta Metal. Mater.*, 1995. **33**(8): p. 1209-1216.

[88] P.N.Anyalebechi, *Met. Trans. B*, 1990. **21B**: p. 649-654.

[89] P.N.Anyalebechi, *Light Metal 1998*, B.Welch, Editor. 1998, TMS: Warrendale,PA.

[90] A.Engh and T.Pedersen, *Light Metals 1984*, J.P.McGreen, Editor. 1984, TMS: Warrendale,PA. p. 1329-1343.

[91] D.A.Larsen, *JOM*, 1997. **49**(8): p. 26-27,67.

[92] D.Dispinar and J.Campbell, *J. Mat. Proc. Tech.*, 2007. **182**: p. 405-410.

[93] O.Richly, *Aluminium*, 1981. **57**(8): p. 546-548.

[94] A.Choudhury and M.Lorke, *Aluminium*, 1989. **65**(5): p. 462-468.

[95] H.J.Seemann, H.Staats, and K.G.Pretor, *Arch. Eisenhutt.*, 1967. **38**: p. 257-265.

[96] G.I.Eskin, *Ultrason. Sonochem.*, 1994. **1**: p. 59-63.

[97] G.I.Eskin and D.G.Eskin, *Ultrason. Sonochem.*, 2003. **10**: p. 297-301.

[98] T.G.Leighton, *Prog. Biophys. Mol. Bio.*, 2007. **93**: p. 3-83.

[99] H.J.Seemann and H.Staats, *Z. Metallkd.*, 1968. **59**(5): p. 347-356.

[100] N.Enomoto, Y.Iimura, and Z.Nakagawa, *J. Mater. Res.*, 1997. **12**(2): p. 371-376.

[101] V.O.Abramov, O.V.Abramov, B.B.Straumal, and W.Gust, *Mater. Design*, 1997. **18**(4-6): p. 323-326.

[102] J.Campbell, *Int. Met. Rev.*, 1981. **26**(2): p. 71-108.

[103] T.V.Atamanenko, *Cavitation-added Grain Refinement in Aluminum Alloys*. 2010, Delft univeristy of technology: Delft.

[104] H.Puga, S.Costa, J.Barbosa, S.Ribeiro, and M. Prokicc, *J. Mater. Process. Technol.*, 2011. **211**: p. 1729-1735.

[105] S.L.Zhang, Y.T.Zhao, X.N.Cheng, G.Chen, and Q.X.Dai, *J. Alloys Compd.* **470**: p. 168-172.

[106] X.Jian, T.T.Meek, and Q.Han, *Scr. Mater.*, 2006. **54**: p. 893-896.

[107] A.H.Freedman and J.F.Wallace, *Trans. AFS*, 1957. **56**: p. 578-589.

[108] G.I.Eskin and D.G.Eskin, *Z. Metallkde.*, 2004. **95**: p. 682-690.

[109] H.K.Feng, S.R.Yu, Y.L.Li, and L.Y.Gong, *J. Mater. Process. Technol.*, 2008. **208**: p. 330-335.

[110] K.Kocatepe and F.Burdett, *J. Mat. Sci.*, 2000. **35**: p. 3327-3335.

[111] N.Abu-Dheir, M.Khraisheh, K.Saito, and A.Male, *Mater. Sci. Eng. A*, 2005. **393A**(1-2): p. 109-117.

[112] S.R.Yu, H.K.Feng, Y.L.Li, and L.Y.Gong, *J. Alloys Compd.*, 2009. **484**: p. 360-364.

[113] Y.Han, K.Li, J.Wang, D.Shu, and B.Sun, *Mater. Sci. Eng. A*, 2005. **405**: p. 306-312.

[114] G.I.Eskin, *Ultrason. Sonochem.*, 1995. **2**(2): p. 137-141.

[115] S.S.Wu, L.F.Liu, Q.Q.Ma, Y.W.Mao, and P.An, *China Foundry*, 2012. **9**(3): p. 201-206.

[116] H.Puga, J.Barbosa, E.Seabra, S.Ribeiro, and M.Prokic, in *Fourth International Conference on Advances and Trends in Engineering Materials and their Applications*. 2009: Hamburg.

[117] H.Puga, J.Barbosa, E.Seabra, S.Ribeiro, and M.Prokic, *Mater. Lett.*, 2009. **63**(9-10): p. 806-808.

[118] A.R.NajiMeidani and M.Hasan, *J. Mat. Proc. Tech.*, 2004. **147**: p. 311-320.

[119] H.B.Xu, Q.Y.Han, and T.T.Meeka, *Mater. Sci. Eng. A*, 2008. **473**: p. 96-104.

[120] H.B.Xu, X.G.Jian, T.T.Meek, and Q.Y.Han, *Mater. Lett.*, 2004. **58**(29): p. 3669-3673.

[121] H.B.Xu, T.T.Meeka, and Q.Y.Han, *Mater. Lett.*, 2007. **61**: p. 1246–1250.

[122] O.V.Abramov and I.I.Teumin, *The Physical Principles of Ultrasonic Technology*. 1970, Moscow: Nauka: p. 427-514.

[123] J.D.Hunt and K.A.Jackson, *J. Appl. Phys.*, 1966. **37**: p. 254-257.

[124] S.L.Hem, *Ultrasonics*, 1967. **5**(4): p. 202-207.

[125] R.Chow, R.Blindt, R.Chivers, and M.Povey, *Ultrasonics*, 2003. **41**: p. 595-604.

[126] R.T.Southin, *J. Inst. Metals*, 1966. **94**: p. 401-407.

[127] L.Zhang, D.G.Eskin, A.Miroux, and L.Katgerman, *IOP Conf. Ser.: Mater. Sci. Eng*, 2012. **27,012002**: p. 1-6.

[128] L.Zhang, D.G.Eskin, and L.Katgerman, *J. Mater. Sci.*, 2011. **46**: p. 5252-5259.

[129] T.V.Atamanenko, D.G.Eskin, L.Zhang, and L.Katgerman, *Metall. Mater. Trans. A*, 2010. **41A**: p. 2056-2066.

Chapter 2

Effect of ultrasonic processing on as cast structure in aluminum alloys containing Zr and Ti

2.1 Introduction

As mentioned in the previous chapter, the type and size of the particles in the melt are crucial to grain refinement in aluminum alloys. In industrial aluminum casting, grain refiners based on Al-Ti-B system, which contain large Al_3Ti particles and much finer, agglomerated TiB_2 particles, are the most widely used for grain refinement [1, 2].

Al_3Ti is well known to be a good nucleation site for α-Al grains because multiple orientation relationships were found between Al_3Ti and α-Al [3]. In addition, solute Ti in the liquid phase acts as a powerful growth restriction element for growing α-Al grains by contributing to the constitutional undercooling effect [4]. However, Al_3Ti particles usually are coarse under typical casting conditions, no matter if they come from undissolved aluminides in Al-Ti-B master alloys, or are naturally formed at hyperperitectic concentration during solidification. Thus, the grain refining effect caused by nucleating on Al_3Ti particles is believed to be not as good as the effect that comes from growth restriction.

Although borides should be poor nucleant particles because of large lattice disregistry with α-Al phase, in most cases, TiB_2 can act as nucleation sites for α-Al grains through the formation of a thin Al_3Ti interfacial layer around [1, 5, 6]. However, it is not suitable for all Al alloys. For instance, in 7xxx series alloys, Zr usually is present as a recrystallization inhibitor [7, 8]. Zr is reported to poison the efficiency of grain refining effect of Al-Ti-B mater alloys [9]. The most probable reason for the decreased potency of Al-Ti-B refiners is the mechanism when Zr inhibits the formation of Al_3Ti layer on the boride [10]. Although increasing the amount of Al-Ti-B master alloy is reported to be able to compensate for this negative effect [2, 11], it is definitely not the best solution in industry. Similarly Si poisons grain refining by TiB_2 particles via substitution of Al_3Ti with Ti_2Si phase [12].

As an alternative, ultrasonic processing is known to induce grain refining in aluminum alloys, especially when the transition metals Zr and Ti are present in the melt [13-17]. As reported by Eskin [13], when the transition metals Zr and Ti were present in the melt, the intermetallics Al_3Zr and Al_3Ti were refined by ultrasonic processing, as well as the grain structure. In the period of primary solidification of intermetallics, ultrasonic cavitation assists the refinement of crystallizing intermetallic compounds. Similar results were also reported by Atamanenko et al. [15, 18]. Al grain refinement occurred when the ultrasonic treatment (UST) was performed in the temperature range of primary solidification of $Al_3(Zr, Ti)$. The ratio between the refinement of primary phases and change of their lattice parameters through dissolution of Ti in Al_3Zr was suggested to be responsible for the good grain refining effect.

The research presented in this chapter was triggered by Atamanenko's results [19]. The objective is to continue to systematically analyze the effect of Zr and Ti on the grain refining effect under ultrasonic processing. Two main questions are in the focus of this chapter: How the intermetallics form under UST and why dramatic grain refinement happens when Zr and Ti are present? To solve these questions, the formation of primary intermetallics under ultrasonic processing in an Al-Ti alloy and an Al-Zr-Ti alloy were investigated. The effect of ultrasonic processing in the alloys containing Zr and Ti on grain refinement was studied by applying UST in different temperature ranges. The effect of the concentration of transition metals and solute on ultrasonic-aided grain refinement was also

presented in this chapter. Based on these results, the foundation for upscaling the ultrasonic technology to industrial process can be established.

2.2 Experimental procedure

The experimental setup for ultrasonic processing used in this study is illustrated in Fig. 2.1. It mainly comprised a 5-kW ultrasonic generator (part A, Fig. 2.1), a 5-kW magnetostrictive transducer with water-cooling system (part B, Fig. 2.1) and a metallic waveguide system with a niobium tip (horn, sonotrode) (part C, Fig. 2.1). The whole setup was placed on a trolley (part E, Fig. 2.1) in order to move the ultrasonic horn (sonotrode) in both vertical and horizontal directions during experiment.
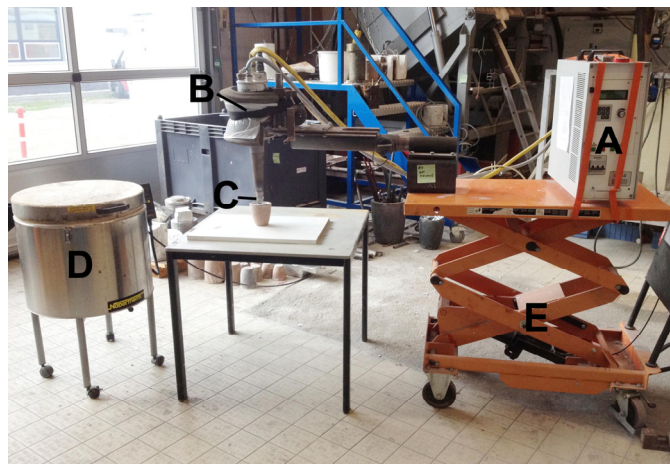

Figure 2.1 Photo of the experimental setup for ultrasonic processing used in this study. A, ultrasonic generator; B, magnetostrictive transducer; C, waveguide system with a niobium tip; D, furnace and E, trolley.

Different sonotrode designs can be used for ultrasonic processing. The two most commonly used designs are cylindrical and conical. The details of these designs can be found in [19]. In this research, only conical Nb sonotrode was chosen in order to obtain a larger amplitude of vibration. The amplitude of vibrations was measured on the sonotrode by a vibrometer. The correlation between the input power and amplitude of vibrations for the conical Nb sonotrode used in this study is shown in Fig. 2.2.
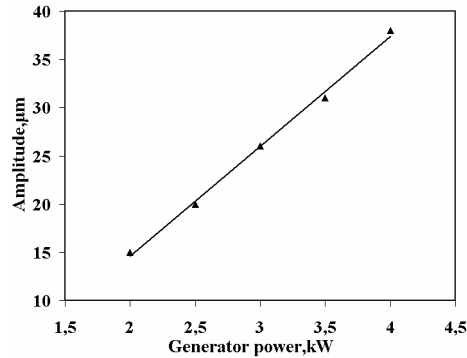
Figure 2.2 The relationship between the amplitude of vibrations and ultrasonic generator power in experimental Nb ultrasonic conical horn.

The alloys used in all experiments in this thesis were prepared using 99.97 wt% pure Al, Al-5 wt% Ti, Al-6 wt% Zr, Al-50 wt% Cu, Al-25 wt% Mg, Al-10 wt% Fe, Al-60 wt% Mn alloys and pure Zn. The commercial AA7075 and AA2024 alloys and Al-3 wt% Ti-1 wt% B master alloy were provided by industry (Aldel, Delfzijl, The Netherlands).

During experiment, the alloy (between 0.3 and 2 kg melt) was firstly molten in an electric furnace, and then treated by ultrasonic processing directly in the crucible. Fig. 2.3 shows the schematic view of ultrasonic processing in the crucible. The tip of the sonotrode was preheated by dipping it in a large volume of molten Al prior to the experiment. After being taken out from the furnace, the melt was treated in the crucible by ultrasound for about 10 to 20 s. The temperature during UST was controlled by a K thermocouple placed in the crucible or by the measurements of the starting melt temperature and the pouring melt temperature. After UST, the melt was poured into the mold that either was made of graphite or copper, depending on the required cooling rate in the experiments. Without ultrasonic treatment, the melt was poured into the mold directly at the given temperature after taken out from the furnace.
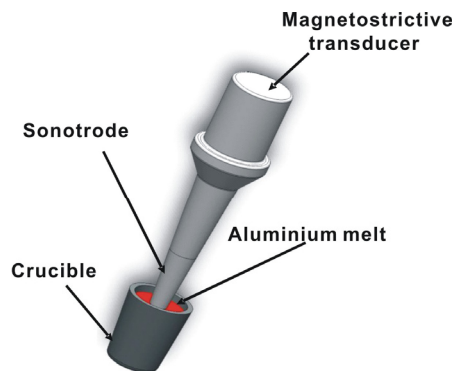

Figure 2.3 Schematic view of ultrasonic processing in the crucible.

In all experiments, the mold was preheated before casting. The size of the samples solidified in copper mold was Ø40 mm × 30 mm. The diameter of the samples solidified in graphite mold was about 50 mm, and the height was 45 mm. The cooling rates during solidification in graphite mold and copper mold were 0.8 K/s, and 2.0 K/s respectively. The temperature was measured by a 0.1-mm thin, open-tip K-thermocouple standing vertically in the center of the mold.

The microstructure and composition analysis were made on cross section taken from the middle of the samples. The chemical composition of all tested Al alloys was measured using a spark spectrum analyzer (Spectro, Kleve, Germany) or X-ray fluorescent analysis. The grain structure of all samples was examined in an optical microscope after grinding, polishing, and electro-oxidizing at 20 VDC in a 3% HBF4 water solution. The size of grains was measured using the linear intercept method. Several straight lines (3-6 lines) were drawn and the number of interceptions of each line with grain boundaries was counted. At least 100 intercepts were counted during each measurement. The average grain size was estimated by the combination of counted intercepts, total test line length and magnification. The error bars presented in this chapter were determined by using standard deviation of the measured grains size in each straight line measurement. During the measurement of the size of intermetallics, at least 20 particles were selected. The average length of these particles was used to represent the size of the intermetallics.

Morphology of the primary intermetallic particles was examined either in an optical microscope or in a scanning electron microscope (SEM) JSM 6500F. The chemical composition of the particles was measured by energy dispersive X-ray spectrum analysis (EDS).

2.3 Formation of primary intermetallics under UST

2.3.1 Effect of UST on primary intermetallics in Al-Ti and Al-Zr-Ti alloys

In order to verify the refinement effect of ultrasound on intermetallics, an Al-0.4 wt% Ti alloy and an Al-0.4 wt% Zr-0.12 wt% Ti alloy were selected. The Al-Ti equilibrium phase diagram and the Al-Zr equilibrium phase diagram are shown in Fig. 2.4 and Fig. 2.5. There is no available ternary Al-Ti-Zr phase diagram and it is known that there are no ternary phases formed in this system, thus, the Al-Zr equilibrium phase diagram instead of the ternary Al-Ti-Zr phase diagram was used.

The temperature range of UST and the concentration of the alloy used in this research were shown as dashed line with arrow in these phase diagrams. A large amount of transition metals in these alloys facilitated the formation of intermetallic compounds during solidification, and make these primary particles more visible.
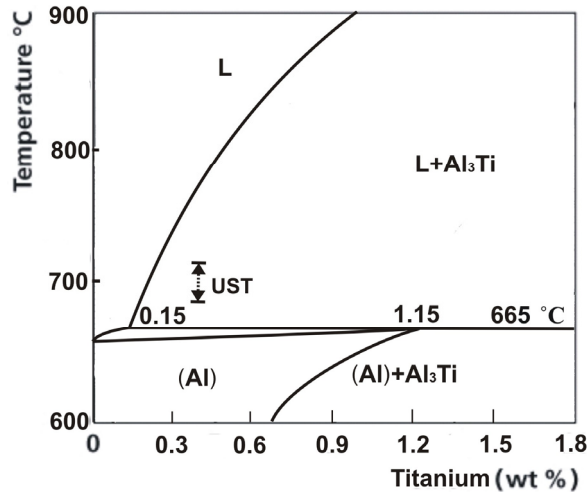
Figure 2.4 Simplified equilibrium Al-rich Al-Ti binary phase diagram, adapted from [20].
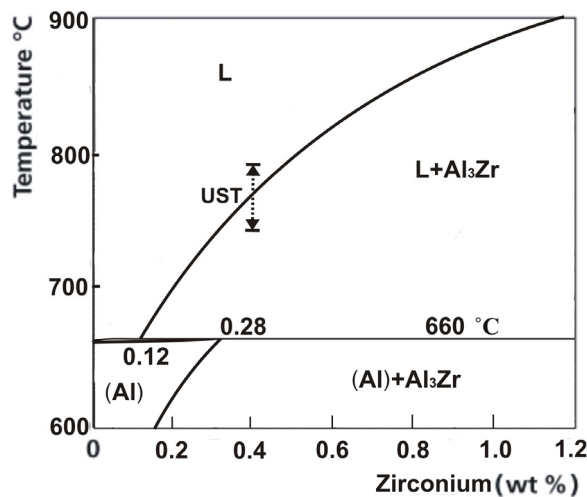

Figure 2.5 Simplified equilibrium Al-rich Al-Zr binary phase diagram, adapted from [21, 22].

In Al-0.4 wt% Ti alloy, the melt (appr. 0.3 kg) in the crucible was subjected to UST (4 kW) in the solidification range of Al_3Ti, from 720 ˚C to 680 ˚C (0.66% solid phase), then was poured in a copper mold. Sample without UST were produced by casting at 720 ˚C.

Figures 2.6 (a) and (b) represent the as-cast microstructures of the Al-0.4 wt% Ti alloy without UST. The size of Al_3Ti particles was in the range of 20 to 80 μm. When UST was applied, two size ranges of Al_3Ti particles were found, as shown in Fig. 2.6 (c) and (d).

28

Most particles became dramatically smaller in size, ranging from 3 to 8 µm. The larger particles with the size ranging from 50 to 80 µm were much less in numbers and are supposed to form during solidification after the end of UST (below 680°C). The Al average grain size reduced from 90 to 65 µm when UST was applied to the Al-0.4 wt% Ti alloy, as illustrated in Fig. 2.7.
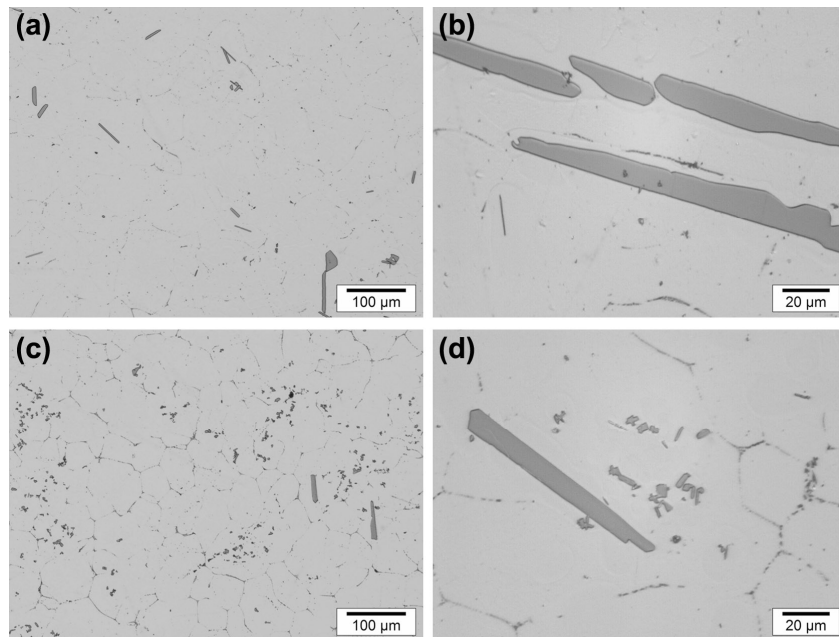
Figure 2.6 Morphology of primary intermetallics in the Al-0.4 wt% Ti alloy: (a) and (b) without UST, at different magnification; (c) and (d) with UST, treated from 720 ˚C to 680 ˚C, at different magnification.

Figure 2.7 Effect of UST on grain structure in the Al-0.4 wt% Ti alloy: (a) without UST and (b) with UST, treated from 720 ˚C to 680 ˚C.

In Al-0.4 wt% Zr-0.12 wt% Ti alloy, the melt (appr. 0.5 kg) was treated by UST (4 kW) in the crucible by ultrasound for about 10 s from the liquidus of Al_3Zr (790 ˚C) to

approximately 750 ˚C (0.4-0.45% solid phase). After UST, the melt was poured into a graphite mold in order to obtain a lower cooling rate of 0.5-0.8 K/s. Without ultrasonic treatment, the melt was poured into a graphite mold directly at temperature 790 ˚C.

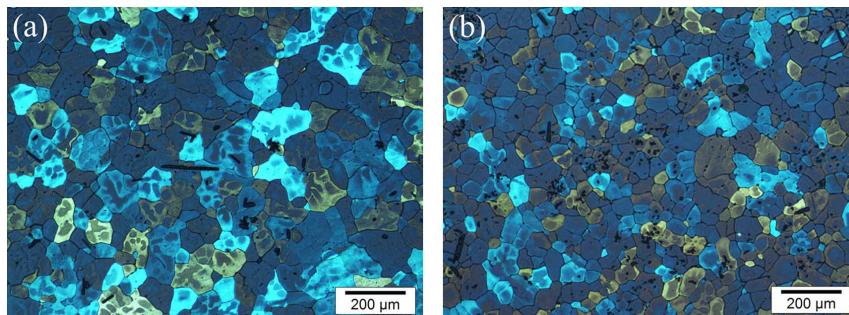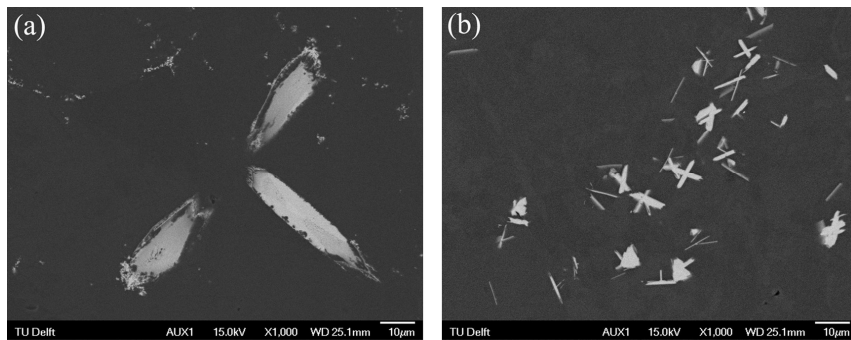Figure 2.8 Morphology of primary intermetallics in the Al-0.4 wt% Zr-0.12 wt% Ti alloy: (a) without UST and (b) with UST, treated from 790 ˚C to 750 ˚C.

Figure 2.8 gives typical examples of primary intermetallics in the Al-0.4 wt% Zr-0.12 wt% Ti alloy cast with and without UST. The results are similar to that in the Al-0.4 wt% Ti alloy. The particles size was reduced from 50-100 μm without UST to 5-10 μm when UST was applied. The grain size increased to some extent when UST was applied in this alloy under the given casting condition. The detail information and suggested mechanism will be discussed later in Chapter 4.

The fragmentation effect caused by the cavitation bubbles collapse is suggested to be the main mechanism of refinement of intermetallics. It is also reported and suggested by many researchers [13, 14, 18]. When the cavitation bubbles collapse, extremely powerful shock waves occur, whose action near the solid interface should be considered as a powerful cause of the destruction and dispersion of growing crystals.

2.3.2 A possible nucleation behavior of primary intermetallics under UST

Fragmentation is frequently considered as the main mechanism of crystal refinement caused by UST. However, it is well known that besides cavitation-assisted fragmentation, UST also gives other benefits to the melt. Transformation of non-wettable oxides present in the melt to nucleation sites is one of the widely discussed effects induced by UST [23, 24]. Aluminum oxides always exist in the melt during casting and are relatively stable at the high temperature range at which primary Al_3Zr form. Do aluminum oxides affect the formation of Al_3Zr primary intermetallics by heterogeneous nucleation to some extent? This is the main question we would like to discuss in this section.

Lattice mismatch is one of the important factors that can be used to predict the nucleation potency of nucleation sites. In order to analyze the nucleation behavior, the edge to edge matching model [25, 26] is used for a preliminary analysis of lattice mismatch between aluminum oxides and Al_3Zr phase.
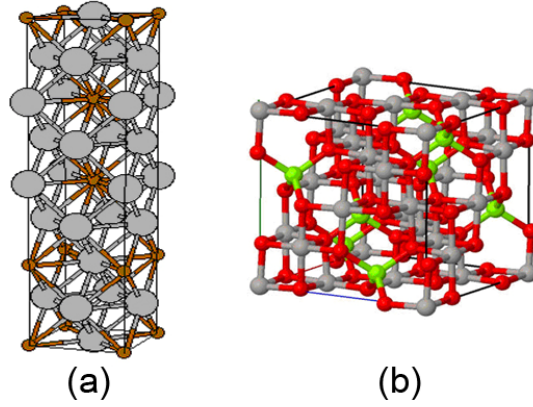
Figure 2.9 Crystal lattice structures of (a) Al_3Zr [27] and (b) γAl_2O_3 with a cubic spinel-type structure [28].

At normal casting temperature, Al_3Zr has a body-center tetragonal structure (DO_{23}) with the lattice parameters a=0.4009 nm, c=1.728 nm [29], as illustrated in Fig. 2.9 (a) [27]. Taking atomic positions and diffraction intensity data (MDI Jade 5.0) into consideration, the most close packed atomic row families run along $<401>_{Al_3Zr}$ and $<110>_{Al_3Zr}$ directions lying in close packed plane families $\{114\}_{Al_3Zr}$ and $\{200\}_{Al_3Zr}$. Aluminum oxide is considered as γAl_2O_3 because it can be stable at normal casting temperature, about 750 ˚C. γAl_2O_3 is generally believed to be a cubic spinel-type structure ($MgAl_2O_4$) [28] with the lattice parameter a=0.7911 in accordance with the Fd-3m space group [30], as shown in Fig. 2.9 (b). The two close packed planes of γAl_2O_3 are $\{400\}_{\gamma Al_2O_3}$ and $\{311\}_{\gamma Al_2O_3}$. The most possible close packed atomic row in these planes is $<110>_{\gamma Al_2O_3}$. Hence the interatomic spacing misfit f_r and interplanar spacing misfit f_d can be calculated. The interatomic spacing misfit f_r represents the interatomic spacing misfit along a pair of close-packed rows coming from the adjacent phases, and is defined by

$$f_r = \frac{|r_m - r_p|}{r_p},$$ (2.1)

where r_m and r_p are interatomic spacings along close packed directions of the nucleated solid and the substrate, respectively. The interplanar spacing misfit f_d is the interplanar spacing misfit between a pair of close packed planes containing the preceding close packed rows and defined by

$$f_d = \frac{|d_m - d_p|}{d_p},$$ (2.2)

where d_m and d_p is interplanar spaces of close packed planes in the nucleated solid and the substrate, respectively.

Thus, the interatomic spacing misfit along the row pair $<401>_{Al_3Zr}/<110>_{\gamma Al_2O_3}$ and $<110>_{Al_3Zr}/<110>_{\gamma Al_2O_3}$ can be calculated as 5.5% and 1.3%. Both are smaller than the suggested limit of 10% for potent matching [25]. The f_d between $\{200\}_{Al_3Zr}/\{400\}_{\gamma Al_2O_3}$ and $\{114\}_{Al_3Zr}/\{311\}_{\gamma Al_2O_3}$ are 1.4% and 0.6% respectively. The data used in the calculations are shown in Table 2.1.

Table 2.1. Crystallographic data of Al_3Zr and γ-Al_2O_3 in an aluminum melt

Phase	Close packed row <hkl>	r_{hkl}, nm	Close packed plane {hkl}	d_{hkl}, nm
Al_3Zr	<401>	0.2950	{114}	0.2370
	<110>	0.2835	{200}	0.2005
γAl_2O_3	<110>	0.2797	{400}	0.1978
			{311}	0.2385

From the calculation, a very small mismatch can be found between aluminum oxide and Al₃Zr phase, which means that oxides might have a good potency to be the substrate for the Al₃Zr phase during nucleation. So as to check this possibility, extra aluminum oxide films from the melt surface were mixed into the melt before UST. Experiments were performed by mixing aluminum oxides films at 820 ˚C into the Al-0.4 wt % Zr-0.12 wt% Ti alloy melt. After mixing, the melt was treated by ultrasound at 4.0 kW generator power from the liquidus of Al₃Zr (790 ˚C) to approximately 750 ˚C, then cast into the graphite mold in order to obtain primary intermetallics at a relatively low cooling rate. Without ultrasonic treatment the pouring melt temperature was 790 ˚C after mixing aluminum oxides films.
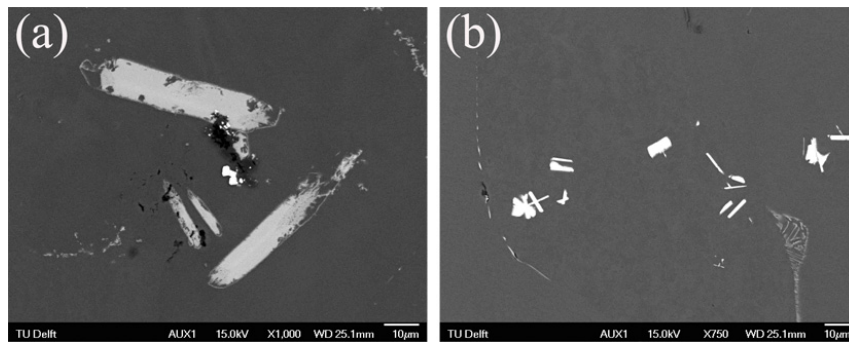

Figure 2.10 Morphology of primary intermetallics in the Al-0.4 wt% Zr-0.12 wt% Ti alloy with mixing oxides: (a) without UST and (b) with UST, treated from 790 ˚C to 750 ˚C.

Figure 2.10 gives an overview of primary intermetallics in the Al-0.4 wt% Zr-0.12 wt% Ti alloy cast with and without UST in the condition of extra aluminum oxide films mixed in.

32

The particles size was reduced from 30-50 μm without UST to 5-10 μm when UST was applied.
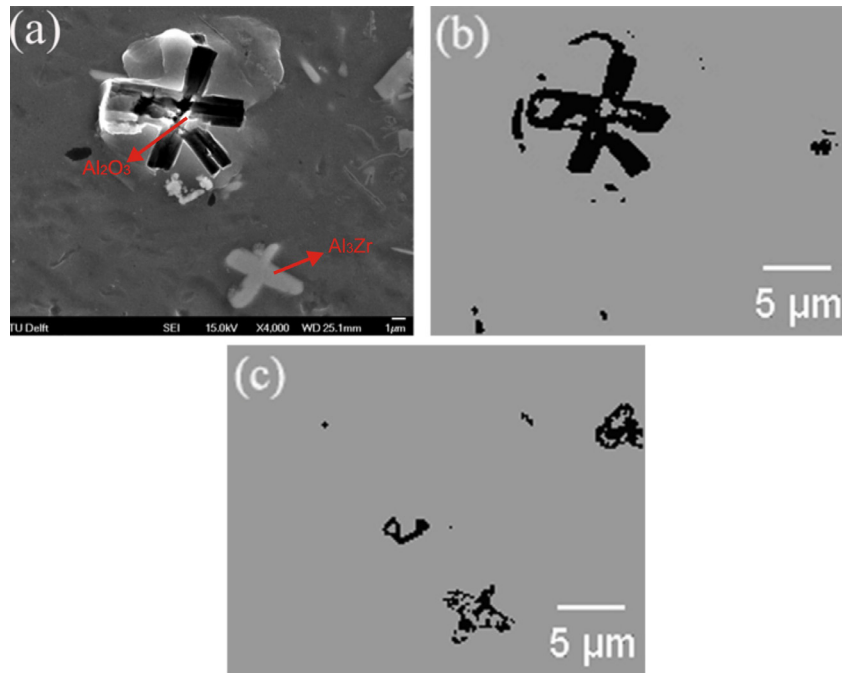

Figure 2.11 Intermetallics and oxides found in an aluminum alloy with 0.4 wt% Zr and 0.12 wt% Ti cast with UST: (a) SEM image; (b) mapping of O element and (c) mapping of Zr element.

Figure 2.11 (a) presents the SEM image of primary intermetallics in the Al-0.4 wt% Zr-0.12 wt% Ti alloy subjected to UST after mixing an extra aluminum oxide film. According to EDS, the upper cross-shaped black phase contains 21 wt % oxygen and 79 wt % Al, and represents therefore the mixed Al_2O_3, as shown in Fig. 2.11 (b). The lower cross-shaped grey particle is Al_3Zr, with approximately 4% dissolved Ti inside (Fig. 2.11 (c)). Most of intermetallics are 5-10 μm when UST was applied. In the light of similar shape of aluminum oxide and Al_3Zr particle observed in Fig. 2.11, it is suggested that an Al_3Zr particle might have nucleated onto the oxide substrate and then was separated from it either during the sample preparation or during melt treatment because of vibration and acoustic streaming. This kind of particles could retain fine structure in the melt (around 5 μm) during solidification. Although the evidence is not conclusive, it gives some support for the hypothesis that alumina inclusions may act as substrates for intermetallic nucleation under cavitation conditions which may be one of the mechanisms of refinement of these primary particles.

However, without UST, the mixing-in of aluminum oxide films did not lead to refinement of primary particles and no association between oxide particles and primary intermetallics could be found.

There are two possible factors acting here. On one hand, oxides are usually not well wettable by the melt, because of the gaseous phase absorbed at their surface. Due to the pressure pulse generated from the collapse of cavitation bubbles, these oxides can be wetted by the melt and transformed to additional nucleation sites. On the other hand, the UST promotes dispersion of oxides from their agglomerates and films, making their distribution finer and more uniform in the melt, therefore, increasing the possibility of nucleation for Al_3Zr phase on oxides.

It is worth noting that although improving wetting ability of oxides by UST may promote the formation of fine primary intermetallics, few primary particles were found around oxides and the amount of oxide inclusions is much less than the number of fine Al_3Zr particles. It is suggested that both the cavitation-induced fragmentation and the nucleation of primary intermetallics should be considered for explaining the formation of fine primary intermetallics under UST.

2.4 Role of solutes and transition metals in grain refinement under UST

2.4.1 Formation of intermetallics and related grain refinement in an Al-Zr-Ti alloy

In the previous section, the refinement of intermetallics particles caused by ultrasonic processing was introduced. It is clear that ultrasonic processing leads to the formation of fine intermetallics during solidification and the increasing of number density of these particles. Do these particles influence the subsequent solidification processing of α-Al grains? This is the topic we would like to discuss in this section.

An Al-0.1 wt% Zr-0.06 wt% Ti alloy at hypo-peritectic concentration and an Al-0.4 wt% Zr-0.06 wt% Ti alloy at hyper-peritectic concentration were selected in this research according to the Al-Zr equilibrium phase diagram (Fig. 2.5).

The reason for selecting Al_3Zr based intermetallics instead of Al_3Ti particles in this study is that the transition element Zr provides less growth restriction effect than Ti. By adding different amount of Zr, the changing of grain structure will be more affected by Al_3Zr intermetallics than by extra growth restriction effect as in the case of adding Ti. Therefore, we can study the effect of particle number and size.

In the Al-0.1 wt% Zr-0.06 wt% Ti alloy, the melt (appr. 0.3 kg) was treated by ultrasound (4 kW) in the crucible from liquid state (760 ˚C) to the solidification range (650 ˚C). After this treatment, the melt was cast into a copper mold. Without UST, the melt was cast directly at 760 ˚C.
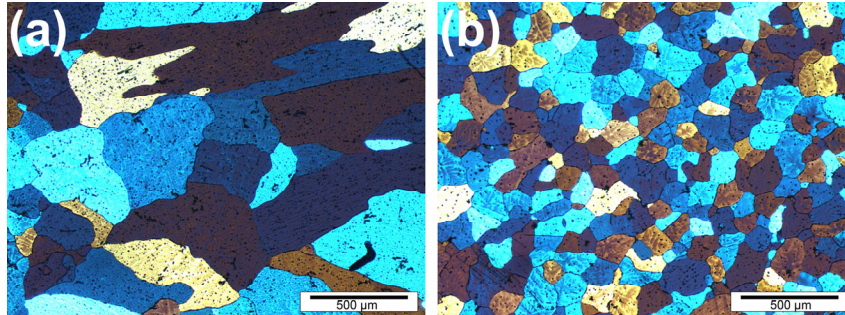
Figure 2.12 Grain structure in the Al-0.1 wt% Zr-0.06 wt% Ti alloy: (a) without UST and (b) with UST, from liquid state (760 ˚C) to the solidification range (650 ˚C).

Figure 2.12 gives the grain structure of the Al-0.1 wt% Zr-0.06 wt% Ti alloy without and with UST. In the non-treated alloy, the grains are coarse and a column structure appears close to the surface of the sample. After being treated by ultrasound, the grain size decreases by about 3 times, as illustrated in Fig. 2.12 and Fig. 2.13. There are no intermetallics found in these samples, as the alloy is at hypo-peritectic concentration. It is suggested that either activation of non-wettable oxides into nucleation sites or fragmentation of growing α-Al crystals caused by UST at around liquidus is responsible to this percentage of grain refinement.
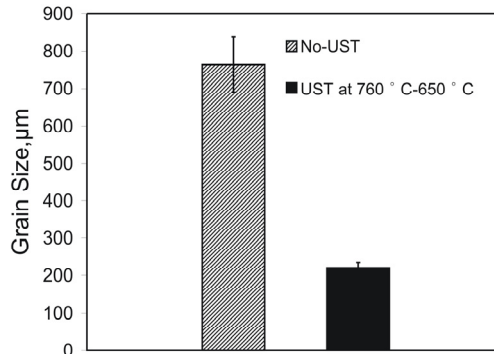

Figure 2.13 Grain size in the Al-0.1 wt% Zr-0.06 wt% Ti alloy.

For the Al-0.4 wt% Zr-0.06 wt% Ti alloy, two temperature ranges of UST were selected. One is only in the liquid state, from 850 ˚C to 810 ˚C. Another is from liquid state (850 ˚C) to the temperature range of primary Al$_3$Zr solidification (760 ˚C). Without UST, the melt was cast directly at 850 ˚C.

35
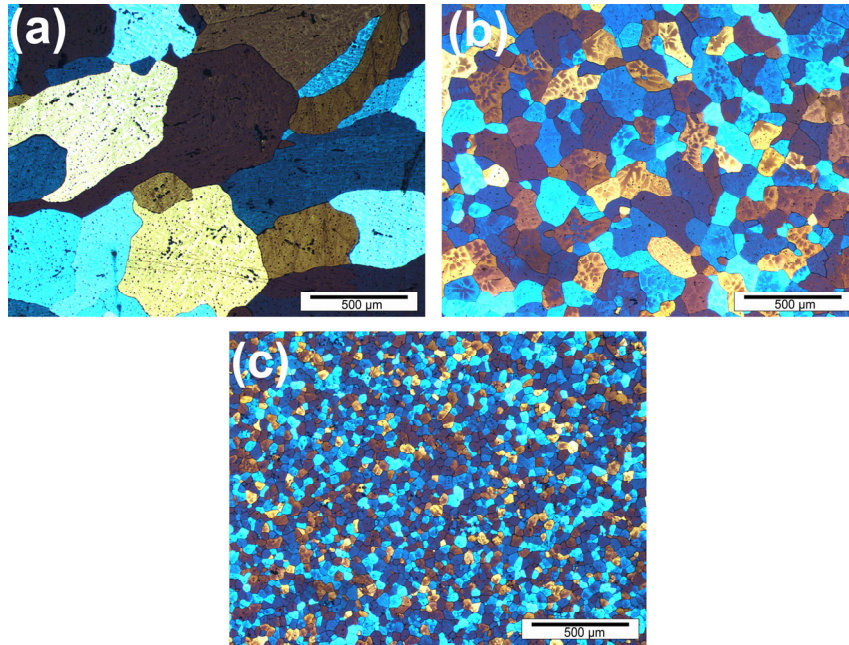
Figure 2.14 Grain structure in the Al-0.4 wt% Zr-0.06 wt% Ti alloy: (a) without UST; (b) with UST, in the liquid state, from 850 ˚C to 810 ˚C and (c) with UST, from liquid state (850 ˚C) to the temperature range of primary solidification (760 ˚C).

Figures 2.14 and 2.15 show the grain structure and the measured average grain size in the Al-0.4 wt% Zr-0.06 wt% Ti alloy without and with UST. When UST was applied in the liquid state, the grain size decreases from 540 μm to 210 μm. Although this alloy is at hyper-peritectic concentration, no intermetallics were found in non-treated alloy and the alloy with UST in the liquid state. This is in opposition to the very large intermetallics observed after slow cooling rate (0.8 K/s) as shown in section 2.3.1. The relative high cooling rate used in this experiment (2 K/s) is considered as the main reason. In this case, Zr will form a supersaturated solid solution with Al due to the suppression of peritectic reaction at the high cooling rate [22]. The mechanism of this grain refinement is considered as same as the mechanism in the Al-0.1 wt% Zr-0.06 wt% Ti alloy. The activation of non-wettable oxides into nucleation sites was considered as the main reason to this percentage of grain refinement.
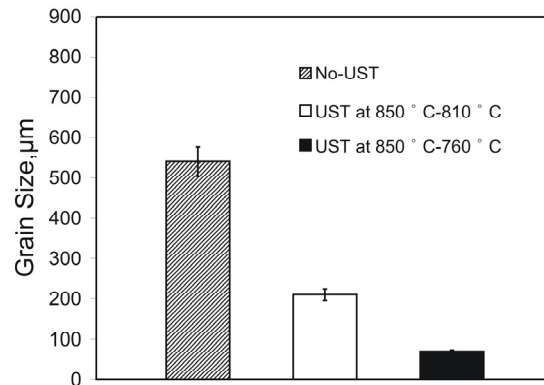
Figure 2.15 Grain size in the Al-0.4 wt% Zr-0.06 wt% Ti alloy.

However, as shown in Fig. 2.14 (c) and Fig. 2.15, a more significant grain refining effect can be achieved when UST is applied in the solidification range of primary intermetallics. The grain size reduces approximately 7-8 times as compared to non-treated alloy. In this case, ultrasonic processing was only applied in the temperature range of primary solidification, and was terminated at 760 ˚C, which is far away from the temperature of α-Al solidification. Why did this dramatic grain refinement happen under this condition?

Looking deeper into the structure, we can find lots of separate fine plate-like particles, most of which usually appear in the center of refined grains, as illustrated in Fig. 2.16. According to EDS composition analysis, these particles are primary intermetallics Al_3Zr with some dissolved Ti. UST facilitates the formation of fine intermetallics, and also it may change the lattice parameter of these intermetallics, which increases the nucleation potency of these particles. During the further solidification processing, these fine particles might act as nucleation sites and promote the grain refining effect by heterogeneous nucleation under proper casting condition, as shown in Fig. 2.14 (c).

Figure 2.16 Grain structure and intermetallics found in the Al-0.4 wt% Zr-0.06 wt% Ti alloy with UST from liquid state (850 ˚C) to the temperature range of primary solidification (760 ˚C): (a) and (b) different magnifications.

37

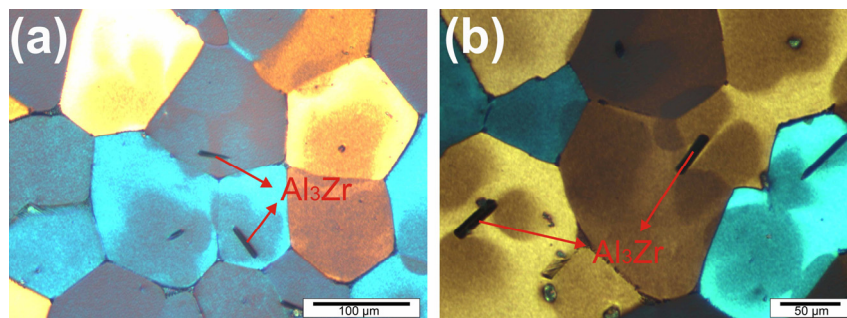2.4.2 Influence of Zr and solute on ultrasonic-aided grain refinement

Through experiments introduced in previous sections, we can suggest that the refined intermetallics are the main reason for the significant ultrasonic-aided grain refinement in Al alloys containing Zr and Ti. But now the question is 'Why and how do these intermetallics affect the grain structure in Al alloy under UST'? According to our experimental observations, UST may have two effects during the solidification processing. It can increase the maximum number of substrates (nuclei) and/or it can increase the nucleation potency of the intermetallics. The effect of ultrasonic processing on the formation of intermetallics in the present of Ti has been studied by Atamanenko et al. and its was found that with the help of UST, Ti was dissolved in Al_3Zr particles, which might change the lattice parameters of this phase and ensure that the nucleating undercooling during solidification is adequate to the size of intermetallics [15, 18, 19]. The objective of this section is to continue to analyze the formation of intermetallics and related grain structure under ultrasonic processing. Through changing the concentration of Zr and solute elements in Al alloy under ultrasonic processing, the link between the intermetallics and grain stricture under UST will be revealed more clearly.

Table 2.2. The casting conditions and alloy compositions in this research

Alloy	Composition, wt%			Additions, wt%	Casting temperature, °C	Cooling rate, K/s
	Cu	Mg	Zn			
Low solute content alloy	1.6	1.3	4.3	0.13Zr, 0.06Ti 0.2Zr, 0.06Ti		
Medium solute content alloy	2.3	1.5	6.1	0.13Zr, 0.06Ti 0.2Zr, 0.06Ti	700	2
High solute content alloy	3.5	1.8	8.3	0.13Zr, 0.06Ti 0.2Zr, 0.06Ti		

In order to study the specific role of Zr under UST, 0.2 wt% Zr and 0.13 wt% Zr with constant amount of Ti were added into three 7xxx-series Al alloys having different accumulated growth restriction factor Q values. The details of casting conditions and alloy compositions are summarized in Table 2.2. The melt (appr. 0.3 kg) was treated in the crucible at 700 ˚C by UST (4 kW) for about 10 s. This temperature was above the liquidus of Al solid solution, and during UST, the melt temperature can reach the solidification range of primary Al_3Zr phase. After UST, the melt was poured into a preheated copper mold.

Figure 2.17 shows the effect of solute content on the grain structures of 7xxx-series Al alloys with 0.2 wt% Zr and 0.06 wt% Ti processed by UST. It clearly demonstrates that with 0.2 wt% Zr, UST results in a grain refining effect for all tested alloys with different *Q*

values. The quantitative information is given in Fig. 2.18. With the help of UST, the grain size decreased about 30-60% as compared to non-treated alloys. With increasing the solute content, the grain size decreased as well.

Figure 2.17 Grain structure in 7xxx-series alloys with 0.2 wt % Zr and 0.06 wt% Ti: (a), (d) low solute content alloy, without (a) and with (d) UST; (b), (e) medium solute content alloy, without (b) and with (e) UST; (c), (f) high solute content alloy, without (c) and with (f) UST.

Figure 2.18 Effect of solute content on grain size of 7xxx-series Al alloys with 0.2 wt% Zr and 0.06 wt% Ti processed by UST.

In order to analyze how UST affects the number of nucleation sites and nucleant potency of the particles, we re-plotted the grain size from Fig. 2.18 with respect to Q values, as shown in Fig. 2.19. The intercept at origin a defined in Eq. 1.2 decreases when UST is used, which means that the maximum number of particles that are active nucleants increases due to UST. This is in good agreement with the results shown in previous sections. Meanwhile, the

39

gradient *b* decreased slightly under UST as well, which shows the nucleant potency of the intermetallics is also improved by UST.
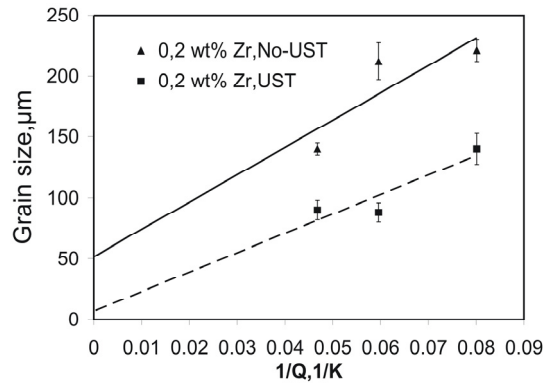
Figure 2.19 Relationship between grain size and $1/Q$ in 7xxx-series Al alloys with 0.2 wt% Zr and 0.06 wt% Ti.

In the alloys with 0.13 wt% Zr and 0.06 wt% Ti, the grain size only decreased in the alloys with higher *Q* values and when UST was applied, as illustrated in Figs. 2.20-2.22. The ultrasonic grain refining effect in these alloys is not as good as with higher Zr concentration.
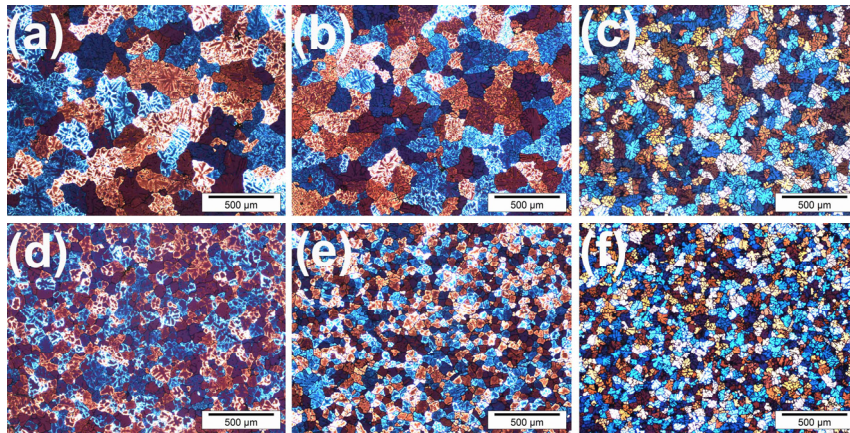

Figure 2.20 Grain structure in 7xxx-series alloys with 0.13 wt % Zr and 0.06 wt% Ti: (a), (d) low solute content alloy, without (a) and with (d) UST; (b), (e) medium solute content alloy, without (b) and with (e) UST; (c), (f) high solute content alloy, without (c) and with (f) UST.
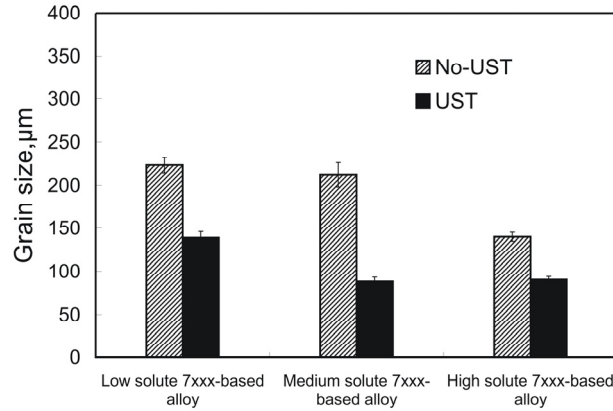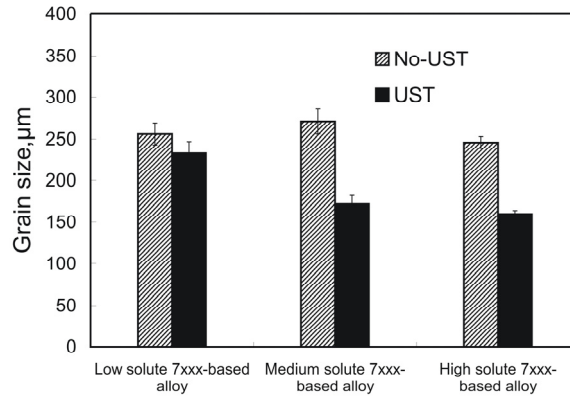
Figure 2.21 Effect of solute content on grain size of 7xxx-series Al alloys with 0.13 wt% Zr and 0.06 wt% Ti processed by UST.
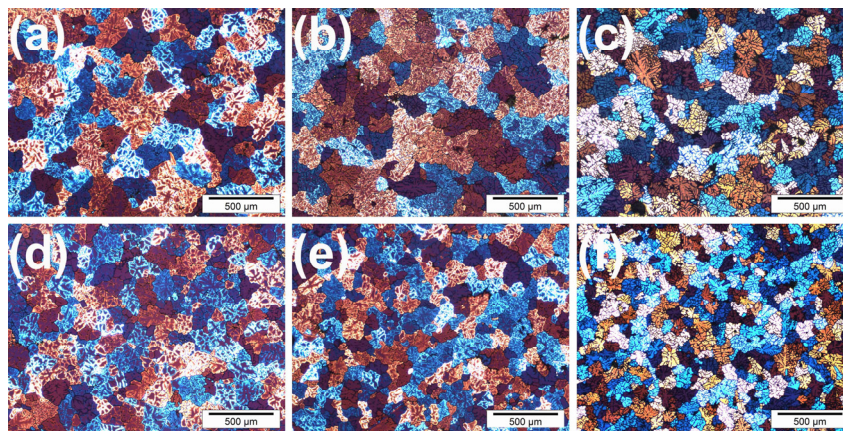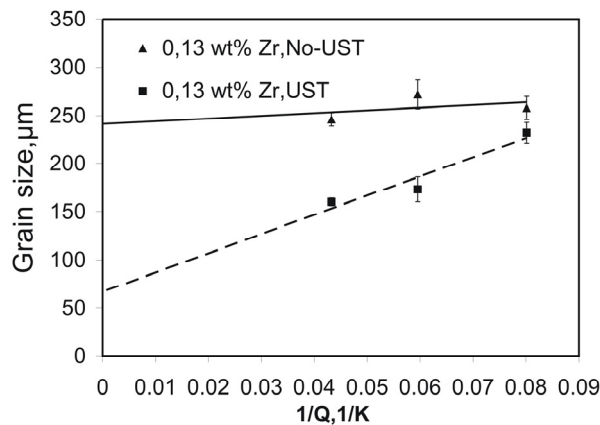

Figure 2.22 Relationship between grain size and 1/Q in 7xxx-series Al alloys with 0.13 wt% Zr and 0.06 wt% Ti.

By plotting the grain size with respect to the Q value (Fig. 2.22), we can see that the grain size remains almost constant in non-treated alloys. UST, however, results in the increased amount of nucleating particles, as demonstrated in Fig. 2.22 by the decrease of the intercept at origin a. It might be confusing in view of the interpretation of Eq.1.2 that the alloys with 0.13 wt% Zr and cast without UST seem to have more potent nucleating particles, as the slope b (nucleating undercooling) is smaller than for the other cases. It is quite possible that in these alloys that are very close to the peritectic point in the Al-Zr system, the formation of primary equilibrium Al_3Zr phase is not occurring under given casting conditions (relative high cooling rate 2 K/s) and either few metastable $L1_2$ Al_3Zr particles are formed (which have very good crystallographic match with Al) or Zr is consumed by a supersaturated solid solution. In the latter case, the gradient b represents the nucleant potency of the particles which are naturally present in the melt. These particles might have good nucleating potency

41

but are scarce. UST has been reported to facilitate the formation of equilibrium Al_3Zr intermetallics and the dissolution of Ti in them [15-17, 19, 31]. It has been also shown that Ti being dissolved in Al_3Zr should actually increase the nucleating undercooling [18]. As a result the undercooling matches the size of numerous refined particles and the efficient grain refinement occurs under UST.

It is worth to note that the *Q* values for the discussed alloys were only calculated by GRF of Cu, Mg and Zn, not including Ti and Zr. On one hand, all Zr and Ti are assumed to be bound in $Al_3(Zr, Ti)$ intermetallics during calculation. On the other hand, Ti is constant in all alloys discussed above, hence, the effect of Ti was considered to be equal. Based on this, the role of Zr concentration and UST can be clearly shown in Fig. 2.23. As one can see, under UST, the maximum number of potent intermetallics increases with increasing Zr concentration, which produces a better grain refining effect, while the nucleant potency of the particles remain the same. The role of Zr under UST is suggested mainly in increasing the number of nucleating particles.
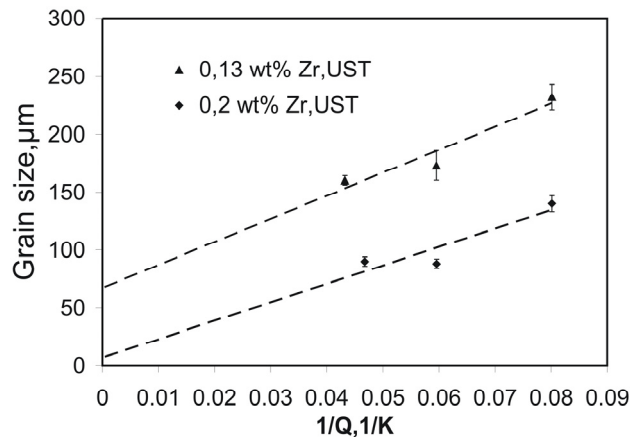
Figure 2.23 Effect of Zr concentration and UST on the grain size at a constant Ti concentration.

2.5 Conclusions

Ultrasonic treatment of molten aluminum alloys can refine the intermetallics dramatically when it is applied in the temperature range of their primary solidification, e.g. in aluminum alloys containing Zr and Ti. It is suggested that both the cavitation-induced fragmentation and the nucleation of primary intermetallics should be considered for explaining the formation of fine primary intermetallics under UST. These refined particles may be involved in further solidification process as nucleation sites and promote the grain refining effect by heterogeneous nucleation.

Typical effects of transition metals Zr and Ti under UST was studied, as well as the effect of solute in the melt. Through these results, we can conclude that three factors act in achieving the optimum grain refining effect in Al alloys with Zr and Ti under UST. Firstly, the amount of Zr should be sufficient to produce primary intermetallics and the UST should

be applied in the temperature range of their formation to assure their refinement. Secondly, Ti should be added and be dissolved in Al_3Zr so that the nucleating undercooling during solidification will be adequate to the size of intermetallics. And thirdly, other solute elements should contribute to this grain refinement by restricting the growth of aluminum grains.

References

[1] A.L.Greer, P.S.Cooper, M.W.Meredith, W.Schneider, P.Schumacher, J.A.Spittle, and A.Tronche, *Adv. Eng. Mater.*, 2003. **5**: p. 81-91.

[2] G.P.Jones and J.Pearson, *Metall. Trans. B*, 1976. **7B**: p. 223-234.

[3] I.G.Davies, J.M.Dennis, and A.Hellawell, *Metall. Trans.*, 1970. **1**: p. 275-280.

[4] T.E.Quested and A.L.Greer, *Acta Mater.*, 2005. **53**: p. 4643-4653.

[5] P.Schumacher, A.L.Greer, J.Worth, P.V.Evans, M.A.Kearns, P.Fisher, and A.H.Green, *Mater. Sci. Technol.*, 1998. **14**: p. 394-404.

[6] M.Easton and D.Stjohn, *Metall. Mater. Trans. A*, 1999. **30A**: p. 1613-1623.

[7] E.Nes, *Acta Metall.*, 1972. **20**: p. 499-506.

[8] N.Ryum, *Acta Mater.*, 1969. **17**: p. 269-278.

[9] S.M.Ahmady, D.G.McCartney, and S.R.Thistlethwaite, *Light Metel 1990*, C.M.Bickert, Editor. 1990, TMS: Warrendale, PA. p. 837-843.

[10] A.M.Bunn, P.Schumacher, M.A.Kearns, C.B.Boothroyd, and A.L.Greer, *Mater. Sci. Technol.*, 1999. **15**: p. 1115-1123.

[11] A.A.Rao, B.S.Murty, and M.Chakraborty, *Mater. Sci. Technol.*, 1997. **13**: p. 769-777.

[12] G.K.Sigworth and M.M.Guzowski, *AFS Trans.*, 1985. **93**: p. 907-912.

[13] G.I.Eskin, *Ultrasonic Treatment of Light Alloy Melts*. 1998, Amsterdam: Gordon and Breach Science Publishers.

[14] O.V.Abramov, *Ultrasound in Liquid and Solid Metals*. 1994, Boca Raton,FL: CRC press.

[15] T.V.Atamanenko, D.G.Eskin, L.Zhang, and L.Katgerman, *Metall. Mater. Trans. A*, 2010. **41A**: p. 2056-2066.

[16] L.Zhang, D.G.Eskin, A.Miroux, and L.Katgerman, *IOP Conf. Ser.: Mater. Sci. Eng*, 2012. **27,012002**: p. 1-6.

[17] L.Zhang, D.G.Eskin, and L.Katgerman, *J. Mater. Sci.*, 2011. **46**: p. 5252-5259.

[18] T.V.Atamanenko, D.G.Eskin, M.Sluitera, and L.Katgerman, *J. Alloys. Comp.*, 2011. **509**: p. 57-60.

[19] T.V.Atamanenko, *Cavitation-Aided Grain Refinement in Aluminum Alloys*. 2010, Delft Univeristy of Technology: Delft.

[20] G.K.Sigworth, *Met. Trans. A*, 1984. **15A**: p. 277-282.

[21] K.E.Kinpling, D.C.Dunand, and D.N.Seidman, *Metall. Mater. Trans. A*, 2007. **38**: p. 2552-2563.

[22] N.A.Belov, A.N.Alabin, D.G.Eskin, and V.V.Istomin-Kastrovskii, *J. Mater. Sci.*, 2006. **41**: p. 5890-5899.

[23] G.I.Eskin, *Ultrason. Sonochem.* , 1994. **1**: p. 59-63.

[24] G.I.Eskin and D.G.Eskin, *Ultrason. Sonochem.*, 2003. **10**: p. 297-301.

[25] D.Qiu, J.A.Taylor, and M.X.Zhang, *Metall. Mater. Trans. A*, 2010. **41A**: p. 3412-3419.

[26] M.X.Zhang, P.M.Kelly, M.A.Easton, and J.A.Taylor, *Acta Mater.*, 2005. **53**: p. 1427-1438.

[27] http://cst-www.nrl.navy.mil/lattice/struk/d0_23.html provided by the Center for Computational Materials Science of the United States Naval Research Laboratory.

[28] http://www.chemtube3d.com/solidstate/_spinel(final).htm provided by University of Liverpool.

[29] S.Srinivasan, P.B.Desch, and R.B.Schwarz, *Scripta Metall.*, 1991. **20**: p. 2513-2516.

[30] G.Gutierrez, A.Taga, and B.Johansson, *Phys. Rev. B*, 2001 **65,012101**: p. 1-4.

[31] L.Zhang, D.G.Eskin, A.Miroux, and L.Katgerman. in *13th International Conference on Aluminum Alloys*. 2012: TMS, p. 1389-1394.

Chapter 3

Effect of ultrasonic processing on as cast structure in aluminum alloys of eutectic systems

3.1 Introduction

In the previous chapter, cavitation-assisted fragmentation of growing crystals has shown to be a promising effect on refinement of structure in aluminum alloys. Transition metals Zr and Ti, due to their participation to peritectic reaction in aluminum system, form primary particles at relative high temperature and prior to the formation of α-Al grains. However, the most commonly used alloying elements in aluminum alloys have eutectic reaction with Al. Eutectic phases usually form simultaneously at a relatively low temperature. The application of ultrasonic processing close to this temperature range might have direct impact on the morphology of eutectic phases. In addition, the formation of primary particles at hyper-eutectic concentration under UST is also worthy of systematic study, since the size and distribution of these particles strongly affect the final properties of aluminum products.

Considering Al-Si alloys for instance, there is a large number of publications on refined microstructures (grain structure, eutectic Si phase and primary Si particles) caused by UST, which show a promising application prospect for UST in Al-Si alloys. The refinement of both grain structure and primary Si particles has been reported by many researchers [1-4]. However, there have been several conflicting reports on refinement of eutectic Si phase in both hypo- and hyper-eutectic Al-Si alloys. Significant refinement of eutectic Si phases caused by ultrasonic treatment has been observed in Refs [5-7], while Refs [1, 2, 8-11] reported the coarsening of eutectic silicon phase when UST was applied to various Al-Si alloy systems.

The effect of ultrasound on the formation of primary particles in other eutectic systems has also been reported by some researchers. For instance, G. Eskin found that in an Al-3%Mn alloy, ultrasonic processing reduced the average size of primary Al_6Mn particles 45-50 times in slow solidification and 5-9 times in accelerated solidification [12]. Similar results can be found in Ref [13] .

However, although it seems obvious that UST affects the microstructures of aluminum alloys of eutectic systems during solidification processing, the ultrasonic treatment time, temperature range and chosen alloy systems differ from researcher to researcher, which makes it difficult to compare the reported results. In addition, the reported data by each research usually focus only on grain structure, or eutectic phases, or primary particles. The probable relationship among these features are rarely mentioned or reported.

The objective of this chapter is to analyze the effect of ultrasonic processing in several aluminum alloys with eutectic reactions. The formation of primary particles and eutectic structures under UST is studied using binary Al-Mn, Al-Fe, and Al-Si alloys. In addition, casting under UST of a commercial Al-Si piston alloy was also analyzed. Several ultrasonic treatment temperature ranges were chosen for these alloys. Unlike the peritectic reaction we introduced in Chapter 2, the nucleation and growth of primary particles and eutectic phases are relatively independent of each other. Could ultrasonic processing bring the same refinement effect on primary particles in aluminum alloys of eutectic system? Do these refined particles still have dramatic influence on the formation of α-Al grains? And does UST refine or coarsen the eutectic phases? The results presented in this chapter aim at further understanding the mechanism of ultrasonic-added structure refinement. The first part of the chapter shows the effect of UST temperature range on the grain size and

intermetallics of near eutectic Al-Mn and Al-Fe alloys. The effect of Ti addition to these alloys is also presented. The effect of UST on eutectic alloys with composition deviating for the eutectic composition is studied in the second part of this chapter using the Al-Si system. The effect of UST temperature range on the microstructure is also examined. Finally, in the last part of the chapter the application of UST to commercial Al-Si piston alloy is discussed.

3.2 Formation of microstructure in binary Al-Fe and Al-Mn alloys

As the common elements in aluminum alloys, Fe and Mn were selected in this research. The Al-Mn system shows an eutectic solidification of Al-Al_6Mn for 1.9 wt% Mn at 657 ˚C while the Al-Fe system shows an eutectic solidification of Al-Al_3Fe for appr. 1.8 wt% Fe at 655 ˚C. A near eutectic Al-1.9 wt% Mn alloy and a near eutectic Al-2.1 wt% Fe alloy were cast while applying UST (4 kW) in the crucible (appr. 0.3 kg melt) for about 10 s, from 700 ˚C, which about 40˚C above the liquidus, to 660 ˚C, close to the eutectic point. After UST, the melt was cast into a copper mold which provides a cooling rate 2 K/s. Without UST, the melt was directly cast into a copper mold at 670 ˚C. The detailed experimental procedure was introduced already in section 2.2. Titanium in an amount of 0.06 wt% was added in some experiments in order to create a larger constitutional undercooling and make the composition of the experimental alloys closer to commercial alloys that usually contain certain amount of Ti. Table 3.1 summarizes the details of casting conditions and alloy compositions.

Table 3.1. The casting conditions and alloy compositions

Alloy	Starting temperature for UST, ˚C	Temperature range of UST	Method of UST
Al-1.9 wt% Mn		No-UST, cast at 670 ˚C	
		UST, at 700-660 ˚C	
Al-1.9 wt % Mn-0.06 wt% Ti	700	No-UST, cast at 670 ˚C	In the crucible
		700-660 ˚C	
Al-2.1 wt% Fe		No-UST, cast at 670 ˚C	
		UST, at 700-660 ˚C	
Al-2.1 wt% Fe-0.06 wt% Ti		No-UST, cast at 670 ˚C	
		UST, at 700-660 ˚C	

In the Al-1.9 wt% Mn alloy, the microstructures in the case of without and with UST are illustrated in Fig. 3.1. In non-treated alloy, no primary particles were found. The grain size of non-treated sample is around 200 μm. When UST was applied, lots of primary particles can be found in the grains at this near eutectic concentration, as shown in Fig. 3.1 (b) and

(c). This is in agreement with previous results in Chapter 2 that UST facilitate the formation of fine primary particles. However, the grain size in the treated alloy dramatically increased from 200 μm to 1100 μm. The presence of Ti decreased the grain size in both non-treated alloy and treated alloy, as shown in Fig. 3.2, but the trend of coarsening the grain structure caused by UST in this alloy still can be clearly observed. Figure 3.3 gives the quantitative information of the grain size in these alloys.
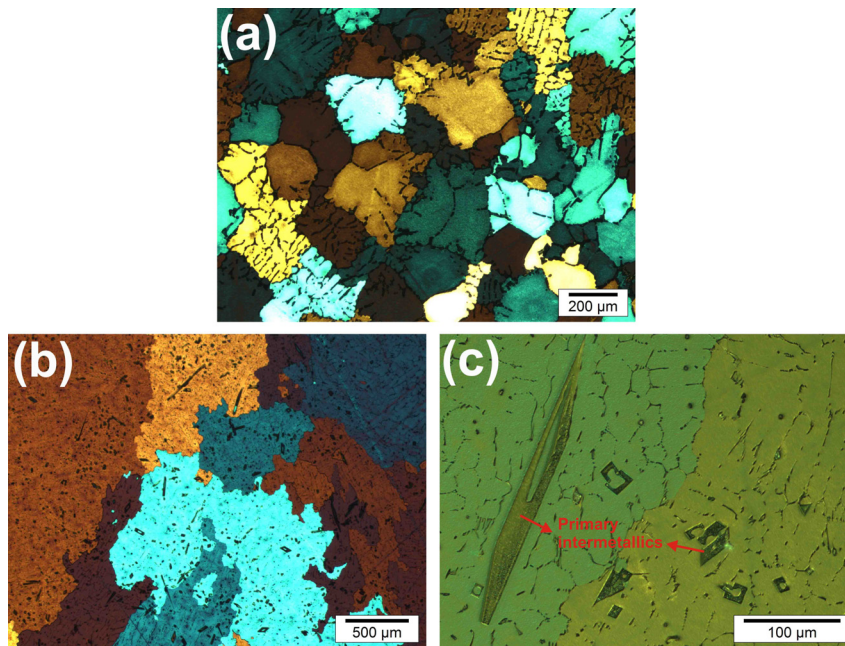
Figure 3.1 Grain structure and intermetallics in the Al-1.9 wt% Mn alloy: (a) without UST; (b) and (c) with UST, from 700˚C to 660 ˚C, with different magnifications.
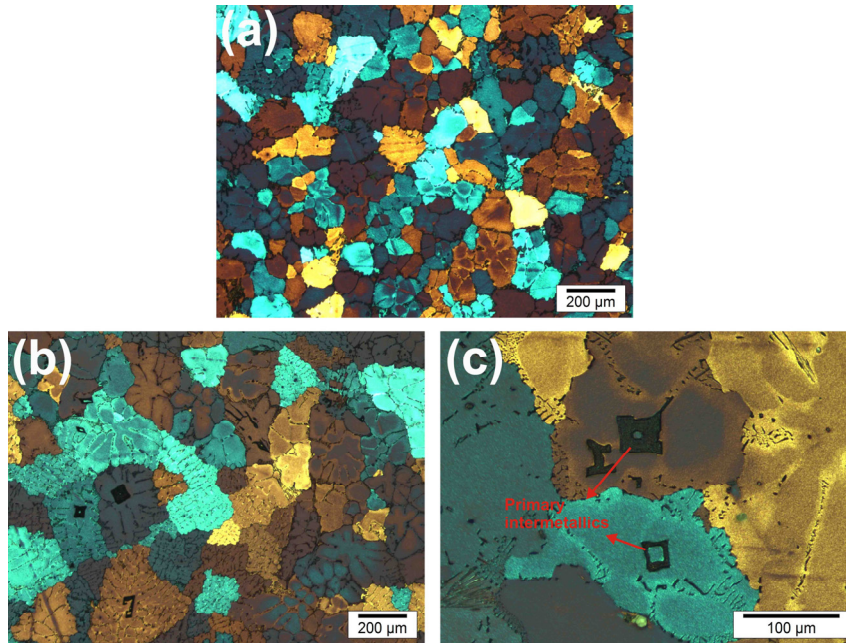
Figure 3.2 Grain structure and intermetallics in the Al-1.9 wt% Mn-0.06 wt% Ti alloy: (a) without UST; (b) and (c) with UST, from 700˚C to 660 ˚C, with different magnifications.
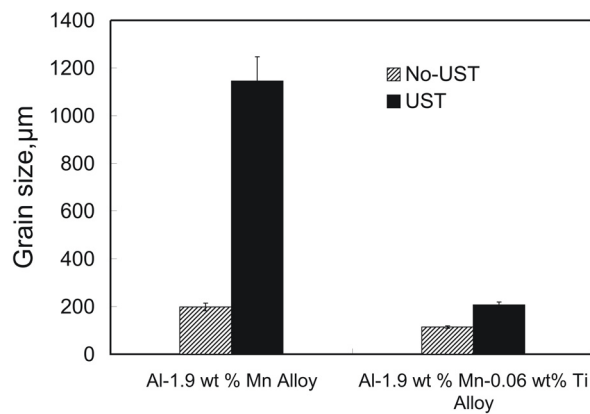
Figure 3.3 Grain Size in the Al-1.9 wt% Mn and in the Al-1.9 wt% Mn -0.06 wt% Ti alloy without and with UST.

It is worth noting that although the number density of the particle decreased to some extent, most of primary particles were observed in the center of grains when 0.06 wt% Ti was added in the ultrasonic treated Al-1.9 wt% Mn alloy, as illustrated in Fig. 3.2 (b) and (c). These particles are believed to act as nucleation sites for α-Al grains, as we suggested in the

previous chapter. Titanium may dissolve into these primary particles or create extra constitutional undercooling to activate these particles, while ultrasound assures that they are relatively fine. This combination makes the nucleation of Al grains easier on these primary particles. Thus, the coarsening effect caused by UST might be alleviated to some extent by Ti, although it cannot be avoided.

Similar results can be found in the Al-2.1 wt% Fe alloy. In non-treated Al-2.1 wt% Fe alloy, large needle-like primary particles and eutectic Fe phases were observed clearly, as shown in Fig. 3.4 (a) and (b). In Fig. 3.4 (c) and (d), we can see that UST resulted in the refinement of the needle-like primary particles and the increase of number density of these particles, as well as the coarsening of eutectic structure and grain structure. Ti had the same effect in this alloy as the effect we suggested before in the Al-1.9 wt% Mn-0.06 wt% alloy (Fig. 3.5 and Fig. 3.6).
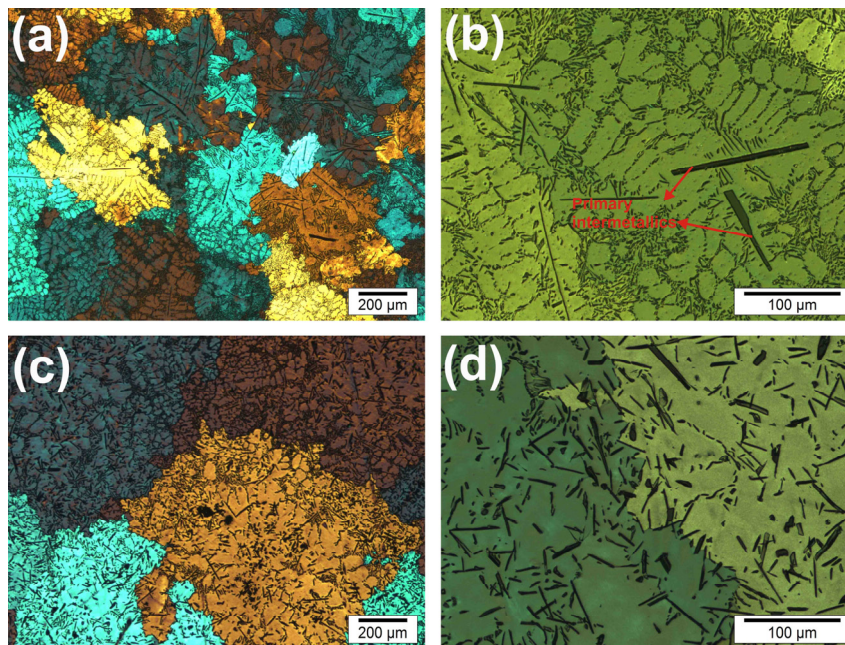
Figure 3.4 Grain structure and intermetallics in the Al-2.1 wt% Fe alloy: (a) and (b) without UST, with different magnifications; (c) and (d) with UST, from 700˚C to 660 ˚C, with different magnifications.
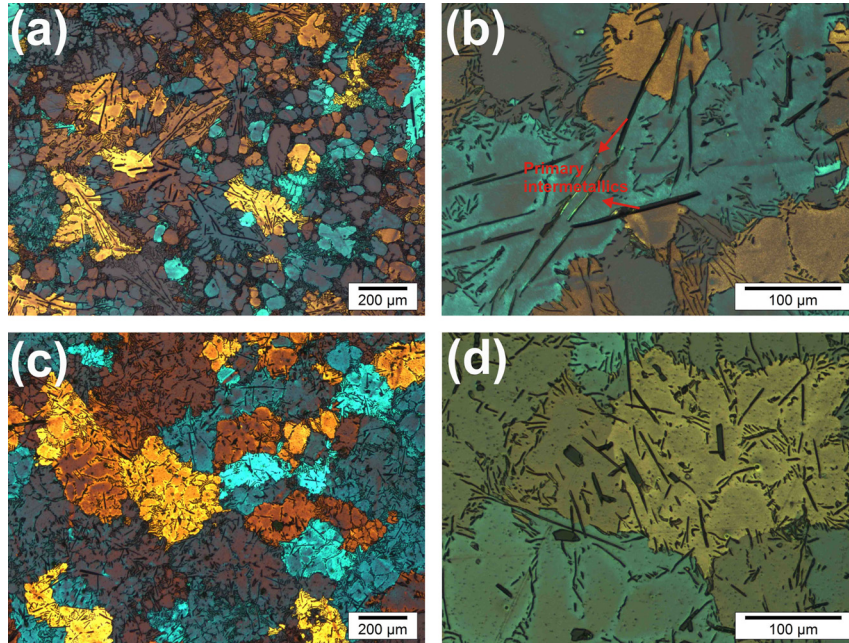
Figure 3.5 Grain structure and intermetallics in the Al-2.1 wt% Fe-0.06 wt% Ti alloy: (a) and (b) without UST, with different magnifications; (c) and (d) with UST, from 700˚C to 660 ˚C, with different magnifications.
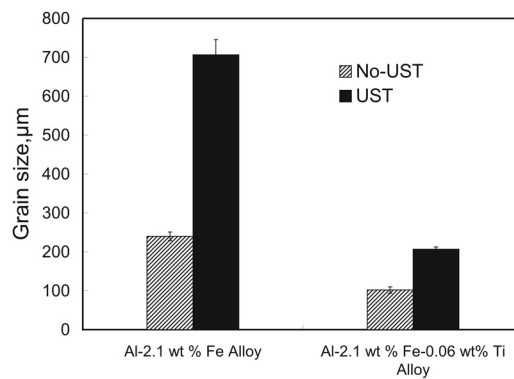
Figure 3.6 Grain Size in the Al-2.1 wt% Fe and in the Al-2.1 wt% Fe -0.06 wt% Ti alloy without and with UST.

The refinement of primary particles has been reported by many researchers and can be understood easily. But what is the mechanism responsible for the coarsening of grain structure when UST is applied to these alloys having eutectic reaction? To solve this query, it is necessary to look at the temperature range of the UST used in these experiments and eutectic reaction itself. During these experiments, ultrasound was applied from liquid state

to the range of primary solidification, and its effects may also be felt during the eutectic reaction.

Therefore, two probable factors are suggested here. On one hand, under the normal casting condition without UST, the solidification occurs under the certain undercooling and the eutectic point shifts to the right. In this case, for the alloys with near-eutectic concentration, more primary (Al) phase will be formed under certain undercooling. This might be the reason why relatively fine grains and no primary intermetallics were found in Al-Mn system and only few primary particles were observed in a more concentrated Al-Fe alloy. However, when UST was applied, it promotes the nucleation of the primary phases, which results in an effectively lower undercooling and the shift of the eutectic point to the left. As a consequence, the grain size increased. This effect might also promote the formation of finer primary intermetallics under ultrasonic processing beside of the fragmentation effect.

On the other hand, the application of UST very close to the eutectic point might directly impact the eutectic reaction and obstruct the interdependent relation of nucleation and growth between eutectic phases. In this case, during eutectic reaction two eutectic phases tend to grow separately and form a kind of "divorced" eutectic structure. This phenomenon can be observed in Fig. 3.4 (d). As we can see, the fine eutectic Fe phases are clearly observable in non-treated alloy. When UST was applied, as shown in Fig. 3.4 (d), the eutectic structure of Fe phases is not as visible as in the non-treated alloy. The morphology of these phases is more close to needle-like primary Fe particles. Although the evidence is not conclusive, it gives some support for the factors of coarsening grain structure we suggested above.

3.3 Formation of microstructure in binary Al-Si alloy

 The previous section introduced the formation of microstructure in near-eutectic Al-Mn and Al-Fe alloys under UST. In this section, binary Al-Si alloys were selected for further analyzing the effect of UST in aluminum alloys of eutectic systems, since the cast Al-Si alloys are widely used in many industrial areas due to their excellent castability, welding ability, corrosion resistance and wear resistance [14-16].

Table 3.2. The casting conditions and alloy compositions in this research

Alloy	Liquidus temperature, ˚C	Temperature range of UST	Mold and cooling rate, K/s
Al-5 wt % Si	630	No-UST, cast at 690 ˚C	Copper mold, 2
		UST, 690-660 ˚C (liquid state)	Copper mold, 2
		UST, 690-610 ˚C (solidification range)	Copper mold, 2
		UST from 690 ˚C until the alloy is mushy	Graphite mold, 0.8
Al-11 wt % Si	589	No-UST, cast at 630 ˚C	Copper mold, 2
		UST, 630-600 ˚C (liquid state)	Copper mold, 2
		UST from 630 ˚C until the alloy is mushy	Graphite mold, 0.8
Al-17 wt % Si	647	No-UST, cast at 720 ˚C	Copper mold, 2
		UST, 720-690 ˚C (liquid state)	Copper mold, 2
		UST, 720-620 ˚C (solidification range)	Copper mold, 2
		UST from 720 ˚C until the alloy is mushy	Graphite mold, 0.8

In this study, hypo-eutectic Al-Si alloy (Al-5 wt% Si), near-eutectic Al-Si alloy (Al-11 wt% Si) and hyper-eutectic Al-Si alloy (Al-17 wt% Si) were cast while applying UST (4kW) in the crucible (appr. 0.35 kg melt) at different temperature ranges. In binary Al-Si alloys, the starting temperature of UST is 40-70 ˚C above the alloy liquidus. During the ultrasonic treatment, the crucible was exposed to air, and the melt temperature decreased continuously as monitored by a K-thermocouple. The UST was performed in the liquid phase for 10 s, or in the temperature range from the starting melt temperature to a temperature within the solidification range, or during the solidification until the alloy was getting mushy (about 0.9 solid fraction). After ultrasonic processing, the melt was poured either into a metallic mold or directly solidified in the graphite crucible. Without ultrasonic treatment the pouring melt temperature was 40-70 ˚C above the liquidus. The casting conditions and their characteristics are summarized in Table 3.2.

3.3.1 Effect of UST on microstructure in hypo-eutectic Al-Si alloy

The liquidus temperature of the Al-5 wt% Si alloy is about 630 ˚C, as determined by thermodynamic simulations.

Figure 3.7 presents the as-cast microstructure of this alloy with and without ultrasonic treatment. Acicular eutectic silicon was observed in non-treated alloy, as shown in Fig. 3.7 (a). When UST was applied in liquid state from 690 ˚C to 660 ˚C (Fig. 3.7 (b)) and in the solidification range of primary aluminum from 690 ˚C to 610 ˚C (Fig. 3.7 (c)) no obvious change in the morphology of eutectic silicon can be found. However, when the melt was treated until later solidification stages, eutectic silicon phase becomes coarser as illustrated in Fig. 3.7 (d).

Figure 3.7 As-cast microstructure of an Al-5 wt% Si alloy: (a) No-UST; (b) UST in the temperature range 690 to 660˚ C; (c) UST in the temperature range 690 to 610 ˚C; (d) UST until the alloy becomes mushy (about 0.9 solid fraction).

Generally, the eutectic silicon forms at 577 ˚C at normal casting condition. Therefore, it is understandable that no obvious effect of UST on morphology of eutectic silicon can be found when it is applied at a temperature well above the eutectic temperature in an Al-Si alloy. Although lots of researches have been done when UST was applied near eutectic temperature or during the whole solidification processing, the reported results are contradictory. Jian et al. [5] used ultrasonic treatment on an A356 alloy and found that, when UST was applied, the average length and width of eutectic silicon decreased from 26 µm to 2 µm and 2.7 µm to 0.6 µm, respectively. And also the eutectic phase spacing was much smaller in the treated alloy. Puga et al. [6] also found the size, thickness and spacing

between eutectic silicon lamellae decreased when UST was used in an AlSi9Cu3 alloy. Similar results can be found elsewhere [7]. However, the opposite results were reported by Freedman and Wallace [8], Burbure et al. [9], Kocatepe and Burdett [10], Abu-Dheir et al. [11], Eskin [1], and Feng et al. [2]. They found the coarsening of eutectic phase when UST was applied in different Al-based alloys. It is suggested that the introduction of ultrasonic energy into the melt increases somewhat the temperature and effectively decreases the undercooling at the solidification front [2].

The results of this study on the formation of eutectic silicon phase are in agreement with the latter, i.e. coarsening results. In the present case, the temperature of the molten alloy decreased during UST. At a lower temperature close to the eutectic reaction, the mushy melt (the melt with high percentage of solid fraction) obstructed the further propagation of cavitation and acoustic flow in the melt, preventing the fragmentation. However, the continuous introduction of ultrasonic energy into the mush resulted in the heat input that slowed the cooling rate and changed the growth conditions of the eutectic, reducing the growth rate without causing the fragmentation of the crystals. Therefore, the eutectic structure coarsened when UST was applied at this temperature range. This is in line with the experimental results which show that ultrasonic treatment additionally superheats the melt [1, 3]. The relatively lower cooling rate in this experiment further increased the size of eutectic phases.

Beside the extra heat input caused by continuous introduction of ultrasound, the coarsening of eutectic Si phase might be also affected by oscillations introduced during eutectic reaction, as we suggested in previous chapter. When UST is applied at eutectic point, eutectic Al phases and eutectic Si phases tend to grow separately, which contribute to some percentage of the coarsening of eutectic Si phases.

As for grain structure, UST clearly led to the refinement of α-Al grains, as summarized in Fig. 3.8 and Fig. 3.9. In the non-treated Al-5 wt% Si alloy, fully grown primary Al dendrites can be observed. The average grain size was 1600 μm (Fig. 3.8 (a)). Some dendrites even grown to more than 4 mm. The UST at the liquid state (from 690 to 660 ˚C) reduced grain size to some extent. This can be explained by transforming non-wetting oxide particles, which are always present in Al melt, into nucleation sites [12, 17]. When UST was applied in the solidification range of primary aluminum, the morphology of primary grains changed to globular and equiaxial. The average grain size was about 100 μm (Fig. 3.8 (c)). This result is consistent with the previous results in Chapter 2 and reported results [12, 18-20]. The cavitation-assisted fragmentation of primary Al phases is considered as the main contributor to the refinement of grain size in the hypo-eutectic Al-Si alloy in this study.

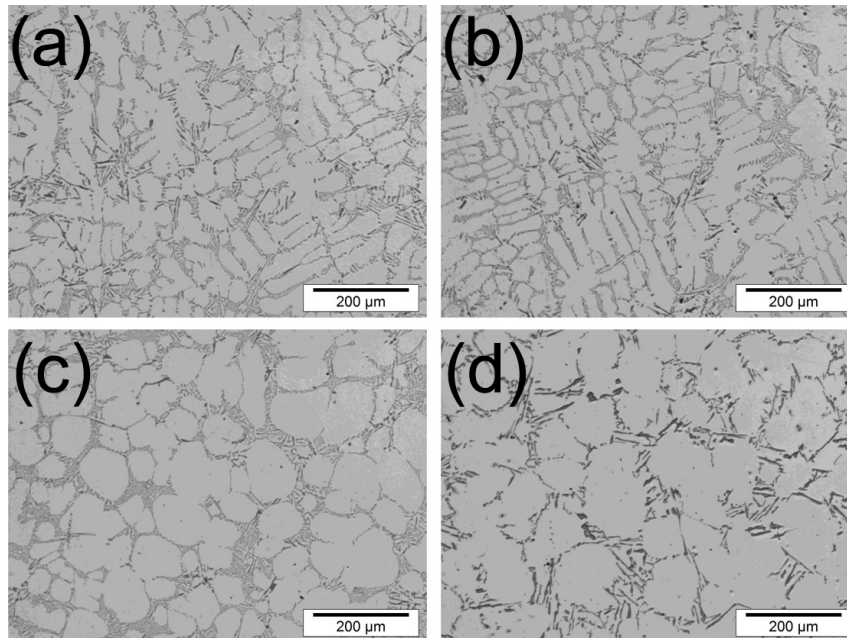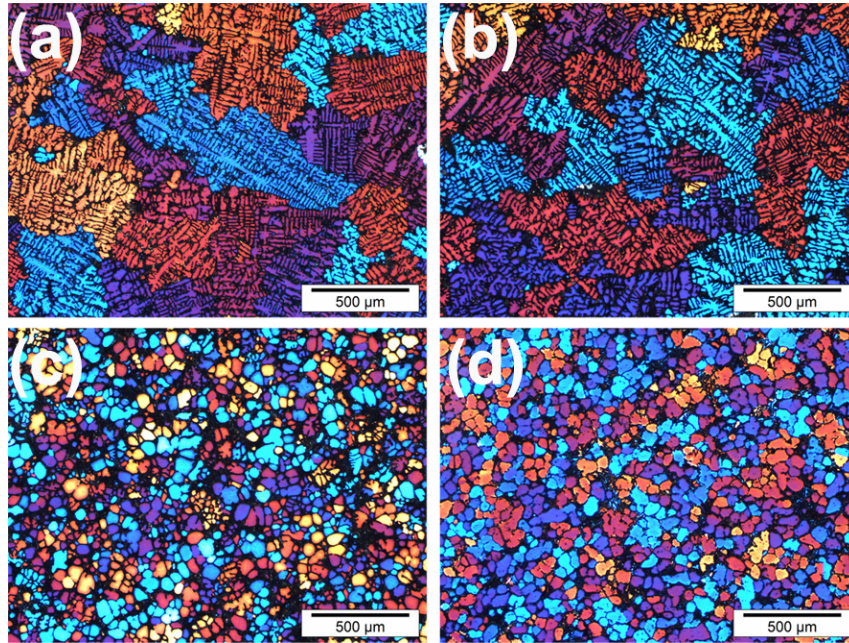Figure 3.8 Grain structure of an Al-5 wt% Si alloy. (a) No-UST; (b) UST in the temperature range 690 to 660˚ C; (c) UST in the temperature range 690 to 610 ˚C and (d) UST until the alloy becomes mushy (about 0.9 solid fraction).
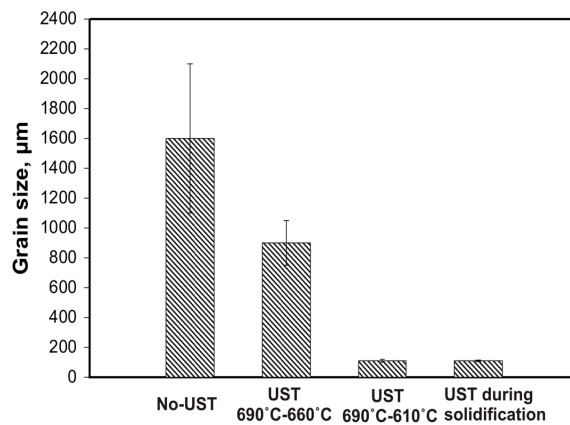

Figure 3.9 Effect of ultrasonic treated temperature range on grain size in Al-5 wt% Si alloy.

3.3.2 Effect of UST on microstructure in near-eutectic Al-Si alloy

In the Al-11%Si alloy, two treatment temperature ranges were used. As shown in Fig. 3.10, primary Si particles can be observed due to non-equilibrium solidification. When the melt was treated for about 10 s, from 630 to 600 ˚C, the size and morphology of Si particles and eutectic Si phases were similar to those in the non-treated alloy. This means that the treatment temperature in this case did not reach the non-equilibrium solidification range of primary Si particles. The average Si particle size was about 25 μm in both cases. When UST was applied down to lower temperatures, the eutectic Si phase coarsened obviously and became more discontinuous. The probable reason was suggested above.

It should be noted that although the average size of primary Si particle did not change a lot as compared with non-treated alloy and 10-s treated alloy (from 630˚C to 600˚C), the outline of Si particles started to changed from straight to irregular (marked in red circle of Fig. 3.10 (c) and (d)), and also some primary Si particles were found to be adhered to eutectic Si phases, as shown in Fig. 3.10 (c) and (d). Although not all particles changed in the current experiment, the trend was clear. Similar results were reported previously that the morphology of Si particles changed from faceted to spherical when UST was applied and it was suggested that the fragmentation of large primary particles followed by aggregation of the fragmented Si is responsible for the spheroidization of the primary Si particles [3]. The adhesion between primary Si particles and eutectic Si phases may be due to nucleation of eutectic Si onto primary silicon. The coarsening of eutectic when the alloy is treated in the mushy zone has been discussed before.
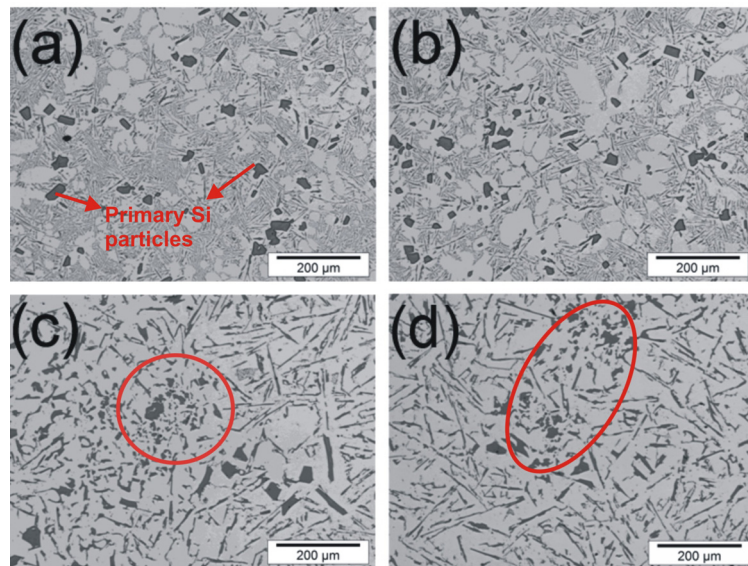

Figure 3.10 As-cast microstructure of an Al-11 wt% Si alloy. (a) No-UST; (b) UST in the temperature range 630 to 600 ˚ C; (c) and (d) UST until the alloy becomes mushy (about 0.9 solid fraction).

Due to a relatively narrow range of solidification of primary aluminum in this alloy as compared to the Al-5 wt% Si alloy, the UST did not result in grain refinement as significant as in the Al-5 wt% Si alloy, as shown in Fig. 3.11. The grain size decreased from 650 μm to 500 μm and further to 250 μm when UST was applied for 10 s in the liquid state and during solidification, respectively. The coarsening effect of grain structure which was discussed in section 3.2, did not appear in this near eutectic alloy. It might be because the fragmentation of primary Al phases was strong enough to overcome the detrimental effect when UST was applied close to eutectic temperature.
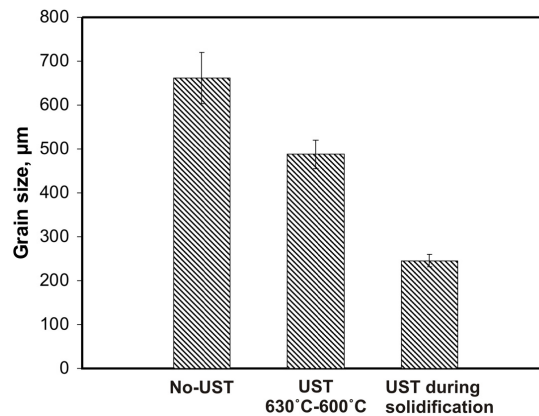
Figure 3.11 Effect of ultrasonic treated temperature range on grain size in Al-11 wt% Si alloy.

3.3.3 Effect of UST on microstructure in hyper-eutectic Al-Si alloy

Good results have been reported for refining of primary Si in hypereutectic Al-Si alloys [1-5, 21]. However, the effect of temperature range on the formation of primary Si phase during UST remains unclear. In our study, an Al–17 wt% Si alloy was treated in three different temperature ranges in order understand the mechanism of Si refinement.

Figure 3.12 shows the microstructures of the Al-17 wt% Si alloy without and after UST. When UST was applied for 10 s in the liquid state, from 720 to 690 ˚C, a dramatic refinement of primary Si particles can be achieved. The average particle size decreased from 45 μm to 18 μm, as illustrated in Fig. 3.12 (b). However, continuation of the ultrasonic treatment to lower temperatures, during the primary Si solidification and further during eutectic reaction, resulted in local coarsening, as illustrated in Fig. 3.12 (c) and (d). The average size of primary Si particles is summarized in Fig. 3.13.

58
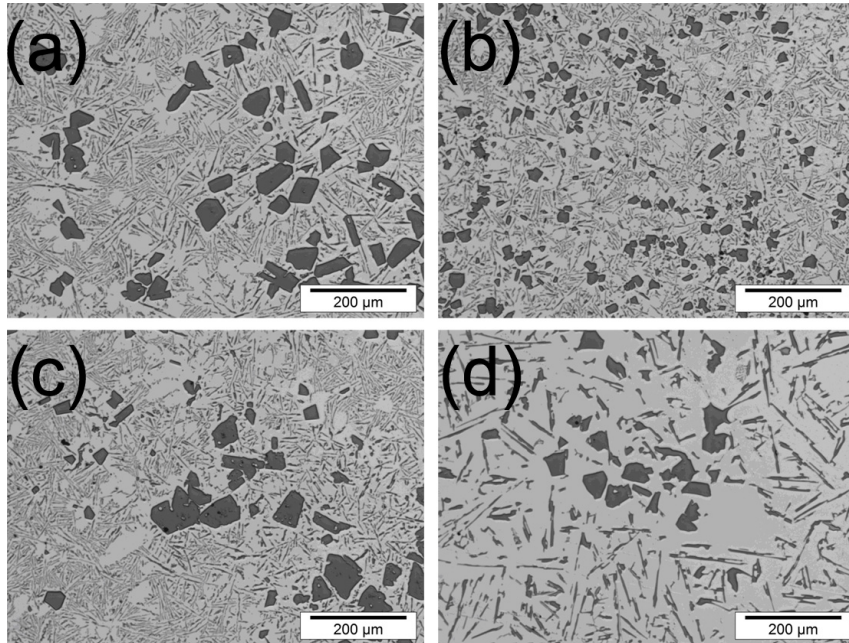
Figure 3.12 As-cast microstructure of an Al-17 wt% Si alloy. (a) No-UST; (b) UST in the temperature range 720 to 690 ˚C; (c) UST in the temperature range 720 to 620 ˚C and (d) UST until the alloy becomes mushy (about 0.9 solid fraction).
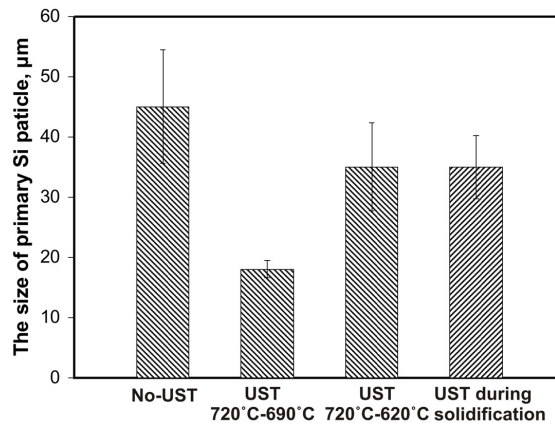
Figure 3.13 Effect of ultrasonic treatment temperature range on the size of primary Si particles in the Al-17 wt% Si alloy.

There are two factors that may influence the refinement of primary Si particles. On one hand, UST multiplies the nucleation sites for the formation of primary Si phases, either

through transforming non-wettable particles present in the melt into nucleation sites, or through increased undercooling related to cavitation expansion and collapse [12]. On the other hand, the cavitation-assisted fragmentation may further reduce the size of primary Si phase [22]. As the primary Si refinement was achieved in our case when UST was performed above the liquidus of the Si primary formation, the former mechanism is more likely to act.

As has been discussed above, when the melt with high percentage of solid fraction is treated by ultrasound, the propagation of ultrasonic effect (i.e. cavitation) is limited except for the heat input and transfer. This heat input increases the alloy temperature or reduces the cooling rate during solidification. As a result, the primary Si particles coarsen and some previously refined Si particles may coalesce and agglomerate as can be observed in Fig. 3.12 (c) and (d).

The main difference between treatment temperature ranges from 720 to 620 ˚C and to the mushy zone is that in the latter case the UST caused the coarsening of eutectic Si phase as well. Meanwhile, the adhesion between primary Si particles and eutectic Si phases can be observed as well when UST was apply at the eutectic temperature in this alloy, as illustrated in Fig. 3.14. It is suggested that both the temperature-related mechanism and the obstruction mechanism of eutectic reaction play a role in coarsening of eutectic Si phases.
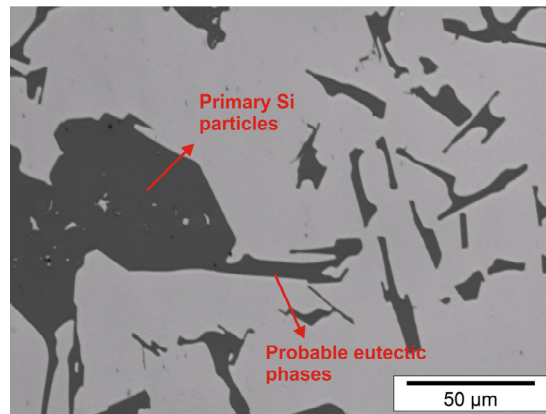
Figure 3.14 An example of probable adhesion effect between primary Si particles and eutectic Si phases.

3.4 Ultrasonic application in a commercial piston Al-Si alloy

Through the analysis in binary Al-Si alloys presented in the previous section, we found that the most promising effect caused by ultrasonic processing is refinement of primary Si particles when UST was applied at a relatively high temperature. In order to further study the ultrasonic processing in Al-Si based alloys and its application prospect, a commercial Al-Si piston alloy was selected. The refinement of primary Si particles is especially important for ductility and toughness of pistons that work under conditions of thermal fatigue.

The commercial Al-Si piston alloy was supplied by industry (Kolbenschmidt, Germany). The composition is shown in Table 3.3.

Table 3.3. Chemical composition of the Al-Si piston alloy (in wt%).

Alloy	Si	Fe	Cu	Mn	Mg	Ni	Zr	Ti
Al-Si piston alloy	10	0.5	3.4	0.2	1.1	2.1	0.13	0.16

Experiments were performed under ultrasonic processing (4 kW) in the crucible (appr. 0.4 kg melt). A range of casting temperatures was chosen to resemble the real casting practice. The main eutectic reaction occurred between 548 and 551 ˚C, as demonstrated from recorded cooling curves during solidification in the mold. The melt was treated for about 10 s in order to avoid any coarsening effect which has been shown previously in binary Al-Si alloys. The starting temperatures of UST were 650 ˚C, 670 ˚C, 700 ˚C and 720 ˚C, respectively. The reduction in melt temperature during UST for each experiment was 30 ˚C. Without ultrasonic treatment, the pouring melt temperatures were 650 ˚C, 670 ˚C, 700 ˚C and 720 ˚C, respectively. A preheated copper mold was used in this experiment.

The results are illustrated by the plot in Fig. 3.15 and the microstructures in Fig. 3.16. The size of primary Si particles decreased with increasing casting temperature. Ultrasonic treatment resulted in a consistent refinement of primary Si particles, but did not lead to any coarsening effect on eutectic Si. The results also show that the more UST temperature is close to the liquidus, the greater the refinement effect is. This is in good agreement with cavitation-assisted nucleation mechanism which shows that the significant refinement usually appear when UST activates the nucleation sites and they have more chance to survive at a lower melt temperature.

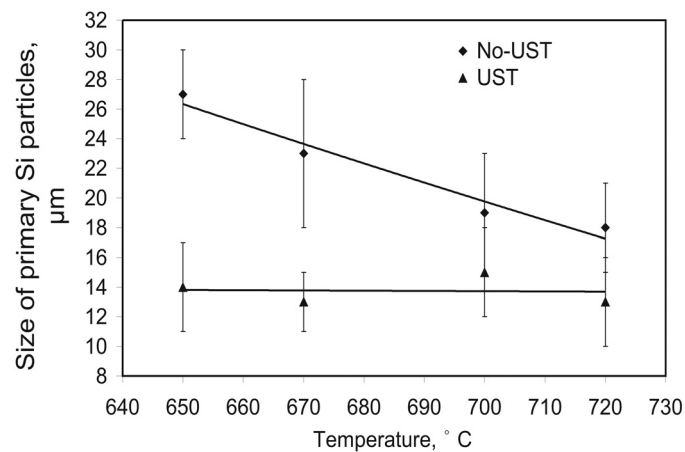Figure 3.15 Effect of ultrasonic treatment temperature and casting temperature on the size of primary Si crystals in the commercial piston alloy.
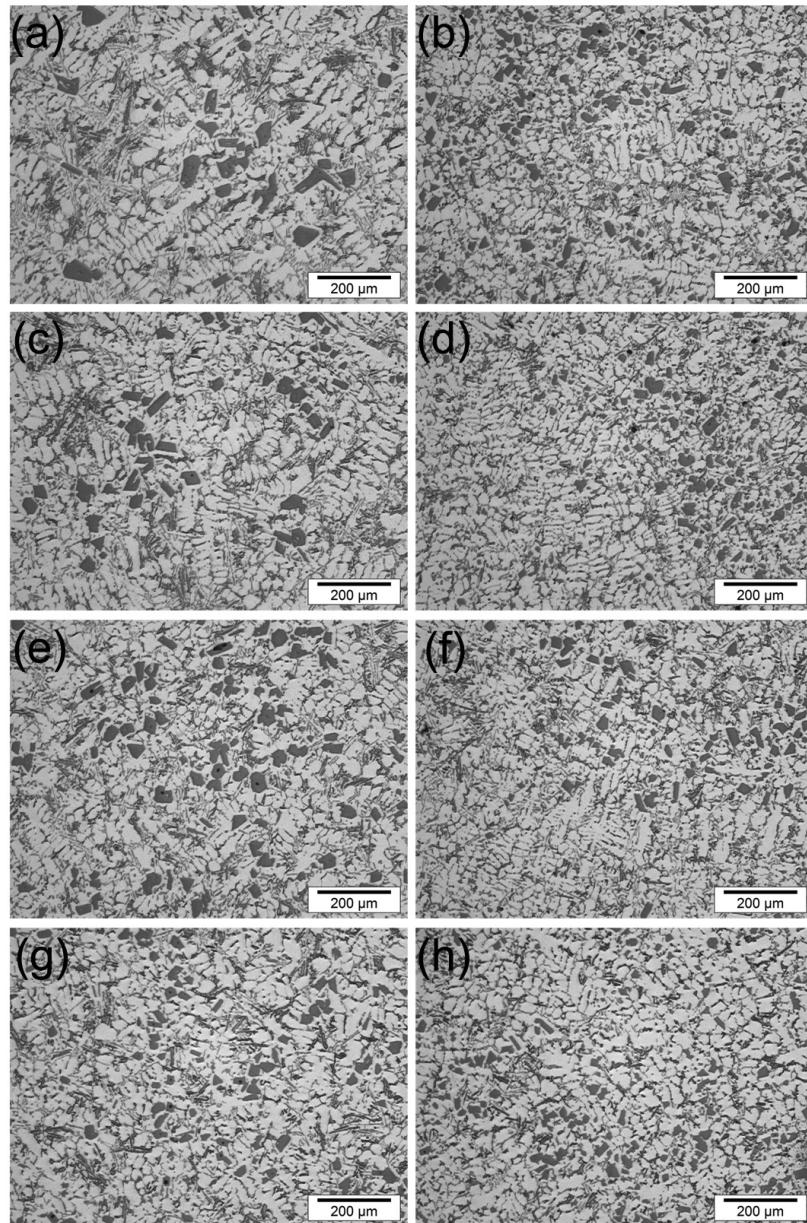
Figure 3.16 As-cast microstructure of a commercial Al-Si piston alloy. (a) No-UST, cast at 650 ˚C; (b) UST, cast at 650 ˚C; (c) No-UST, cast at 670 ˚C; (d) UST, cast at 670 ˚C; (e) No-UST, cast at 700 ˚C; (f) UST, cast at 700 ˚C; (g) No-UST, cast at 720 ˚C and (h) UST, cast at 720 ˚C.

3.5 Conclusions

Experimental results in this chapter clearly show that ultrasonic processing facilitates the refinement of primary particles. However, the primary particles have little effect on the refinement of Al grain structure. Instead, grain and eutectic coarsening effect was found in near-eutectic Al-Mn and Al-Fe alloys when UST was applied close to eutectic temperature. Obstruction of the interdependent relation of nucleation and growth between eutectic phases caused by UST close to eutectic temperature was considered as the main mechanism.

In Al-Si alloys, the most promising effect caused by ultrasonic processing is refinement of primary Si particles in hyper-eutectic alloys when UST is applied at relative high temperature. UST performed during further solidification near the eutectic temperature results in coarsening and agglomeration of primary Si and also of the eutectic Si phases. It is suggested that both temperature related mechanism and obstruction mechanism of eutectic reaction play a role in coarsening of eutectic Si phases.

Although good grain refinement can be still achieved in aluminum alloy of eutectic systems, a relative long time ultrasonic treatment at temperature range of the primary Al phase is necessary. Cavitation assisted fragmentation effect of the primary Al phase is suggested to be the main reason for grain refinement in aluminum alloys of eutectic systems. However, along with long time ultrasonic treatment, it is the continuous introduction of ultrasonic energy into the melt, which resulted in the heat input that slowed the cooling rate and changed the growth conditions of the crystals, especially when UST was applied close to eutectic temperature. Thus, it is suggested to avoid ultrasonic processing applied close to eutectic temperature.

References

[1] G.I.Eskin and D.G.Eskin, *Z. Metallkde.*, 2004. **95**: p. 682-690.

[2] H.K.Feng, S.R.Yu, Y.L.Li, and L.Y.Gong, *J. Mater. Process. Technol.*, 2008. **208**: p. 330-335.

[3] V.O.Abramov, O.V.Abramov, B.B.Straumal, and W.Gust, *Mater. Design*, 1997. **18**(4-6): p. 323-326.

[4] S.R.Yu, H.K.Feng, Y.L.Li, and L.Y.Gong, *J. Alloys Compd.*, 2009. **484**: p. 360-364.

[5] X.Jian, T.T.Meek, and Q.Han, *Scr. Mater.*, 2006. **54**: p. 893-896.

[6] H.Puga, S.Costa, J.Barbosa, S.Ribeiro, and M. Prokicc, *J. Mater. Process. Technol.*, 2011. **211**: p. 1729-1735.

[7] S.L.Zhang, Y.T.Zhao, X.N.Cheng, G.Chen, and Q.X.Dai, *J. Alloys Compd.* **470**: p. 168-172.

[8] A.H.Freedman and J.F.Wallace, *Trans. AFS*, 1957. **56**: p. 578-589.

[9] R.R.Burbure, I.Hareesha, and K.S.S.Murthy, *Br. Foundryman*, 1979. **72**: p. 34-38.

[10] K.Kocatepe and F.Burdett, *J. Mat. Sci.*, 2000. **35**: p. 3327-3335.

[11] N.Abu-Dheir, M.Khraisheh, K.Saito, and A.Male, *Mater. Sci. Eng. A*, 2005. **393A**(1-2): p. 109-117.

[12] G.I.Eskin, *Ultrasonic Treatment of Light Alloy Melts*. 1998, Amsterdam: Gordon and Breach Science Publishers.

[13] Y.Osawa, S.Takamori, T.Kimura, K.Minagawa, and H.Kakisawa, *Mater. Trans.*, 2007. **48**(9): p. 2467-2475.

[14] V.S.Zolotorevsky, N.A.Belov, and M.V.Glazoff, *Casting Aluminum Alloys* 2007, Oxford: Elsevier Science.

[15] M.M.Haque and M.A.Maleque, *J. Mater. Process. Technol.*, 1998. **77**: p. 122-128.

[16] G.Heiberg, K.Nogita, A.K.Dahle, and L.Arnberg, *Acta. Mater.*, 2002. **50**: p. 2537-2546.

[17] T.V.Atamanenko, *Cavitation-aided Grain Refinement in Aluminum Alloys*. 2010, Delft Univeristy of Technology: Delft.

[18] X.T.Li, T.J.Li, X.M.Li, and J.Z.Jin, *Ultrason. Sonochem.*, 2006. **13**: p. 121-125.

[19] A.Das and H.R.Kotadia, *Mater. Chem. Phys.*, 2011. **125**: p. 853-859.

[20] X.Jian, H.Xu, T.T.Meek, and Q.Han, *Mater. Lett.*, 2005. **59**: p. 190-193.

[21] J.A.Dantzig and M.Rappaz, *Solidification*. 2009, Boca Raton: CRC Press.

[22] O.V.Abramov, *Ultrasound in Liquid and Solid Metals*. 1994, Boca Raton,FL: CRC press.

Chapter 4

Parameters of ultrasonic processing

4.1 Introduction

Chapters 2 and 3 described systematic studies of different aluminum alloy systems under ultrasonic processing. The results clearly show a promising grain refining effect in aluminum alloys of both peritectic systems and eutectic systems. However, the main mechanism of ultrasonic-added grain refinement is different. In the alloys containing Zr and Ti, a short time ultrasonic processing applied in the solidification range of primary intermetallics (almost liquid state) ensures the formation of enough fine intermetallics, thus promoting a good grain refining effect via enhanced nucleation. In alloys of eutectic systems, cavitation assisted fragmentation effect of primary α-Al phase is suggested to be the main reason for grain refinement. However, a relatively long time ultrasonic treatment (UST) is necessary and ultrasonic processing applied close to eutectic temperature causes structure coarsening and is suggested to be avoided.

Since ultrasonic-aided grain refinement seems quite promising, why is ultrasonic processing rarely applied in real industrial operations? Looking through the reported data, there is a lack of systematic analysis of the parameters of ultrasonic processing. This does not only restrict the understanding of the mechanism of ultrasonic-aided grain refinement, but also constraints further applications of ultrasonic processing in industrial production. Besides different alloy systems used in experiments, the design of sonotrode, operational power of the generator, selected UST time, temperature range of UST, treated volume, holding time after UST, and even further solidification processing differ from study to study. In such a case, a robust ultrasonic processing technology can hardly be developed for industrial application.

In order to reach a more complete understanding of the effects of ultrasonic processing parameters, a systematic study was performed and is presented in this chapter. Aluminum alloys containing Zr and Ti were selected for this research and in following chapters as well. On one hand, the transition metals Zr and Ti allow the application of ultrasonic processing in liquid state (above the liquidus of Al) to result in a very good grain refining effect. This feature dramatically improves the flexibility of the application of ultrasonic processing. On the other hand, in several commercial aluminum alloys, such as 7xxx alloy, transition metal Zr and Ti are always present. The grain refining effect and cost efficiency can be improved by applying UST of these alloys during casting without adding extra master alloys.

Some preliminary analyses on the influence of some parameters of UST have been done by Dr. Atamanenko in the group at TU-Delft. It was found that for 0.18 kg/90 cm^3 of Al-0.18 wt% Zr-0.07 wt% Ti alloy, a UST of 7 to 10 s at 700 ˚C was necessary to refine the structure by a factor 3. However, with increasing the amount of melt, the grain size became coarser. The results are summarized in Fig. 4.1 and Fig. 4.2.

In this chapter, the parameters of UST were further studied. The effects of power of ultrasonic generator, initial sonotrode temperature, the temperature of ultrasonic treatment, holding time after ultrasonic processing and cooling rate during solidification on ultrasonic-aided grain refinement was experimentally studied in the aluminum alloys containing Zr and Ti in order to lay the foundation for industrial application of ultrasonic processing
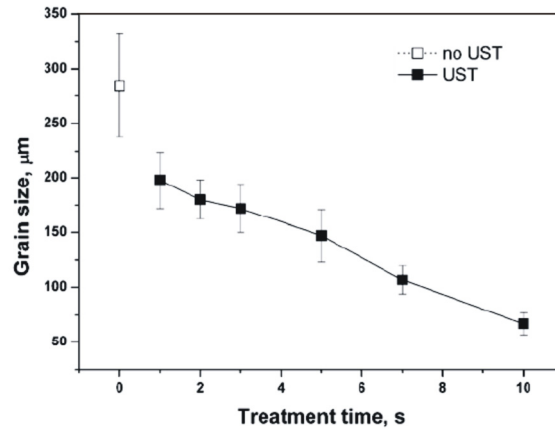
Figure 4.1 Influence of treatment time on the grain size of an Al-0.18 wt% Zr-0.07 wt% Ti alloy treated at 700 ˚C. The treated volume was about 90 cm^3 [1].
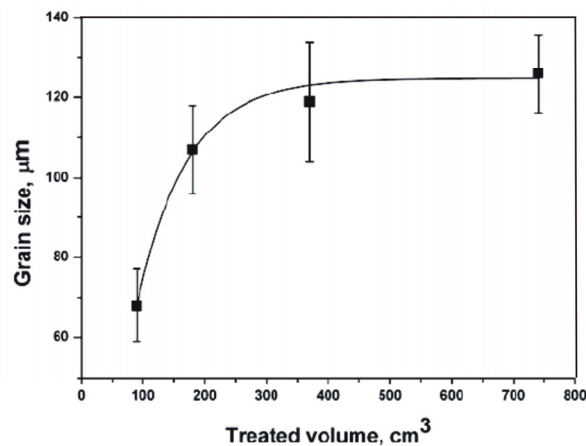
Figure 4.2 Influence of treated volume on the grain size of an Al-0.19 wt% Zr-0.08 wt% Ti alloy treated at 700 ˚C for 10 s [1].

4.2 Power of ultrasonic generator

In order to evaluate the level of grain refinement and the formation of primary intermetallics under different ultrasonic intensities, an Al-0.4 wt% Zr-0.12 wt% Ti alloy was subjected to UST at 4, 3.5, 3, 2.5 and 2 kW generator powers. The corresponding amplitudes of vibrations can be found in Fig. 2.2. During experiments, the Al-0.4 wt% Zr-0.12 wt% Ti alloy was first melted in an electric furnace, and then treated in the crucible (appr. 0.5 kg melt) by ultrasound for 10 s from the liquidus of Al$_3$Zr (790 ˚C) to approximately 750 ˚C (0.4-0.45% solid phase). After UST, the melt was poured into a metal mold, which provides 2.0 K/s cooling rate. Without UST the pouring melt temperature was 790 ˚C.

When UST was applied, $Al_3(Zr,Ti)$ intermetallics were found in two types of morphologies: separate plates and agglomerated particles. As shown in Fig. 4.3 and Fig. 4.4, the size of separate plates and agglomerated particles slightly increases with increasing the amplitude, while the number of agglomerated particles decreases dramatically. There are only few agglomerated particles found under the condition of 4 kW generator power. Higher intensity of UST causes more uniform distribution of intermetallics due to more intense acoustic flows and, therefore, more separate plates and fewer star-like agglomerated particles are observed. No intermetallics were found in the case of No-UST under given cooling conditions (Fig. 4.3 (a)). The reason was already suggested in section 2.3.1. The primary solidification of intermetallics might be suppressed at the relative high cooling rate used in this work.
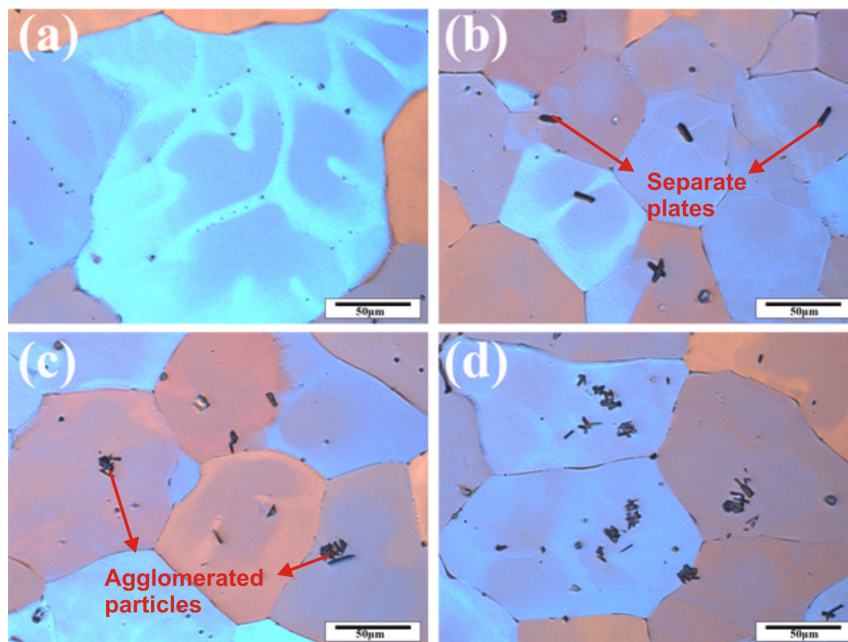

Figure 4.3 Grain structure and morphology of primary intermetallics in the Al-0.4 wt% Zr-0.12 wt% Ti alloy: (a) without UST; (b) UST at 4 kW generator power; (c) UST at 3 kW generator power and (d) UST at 2 kW generator power.
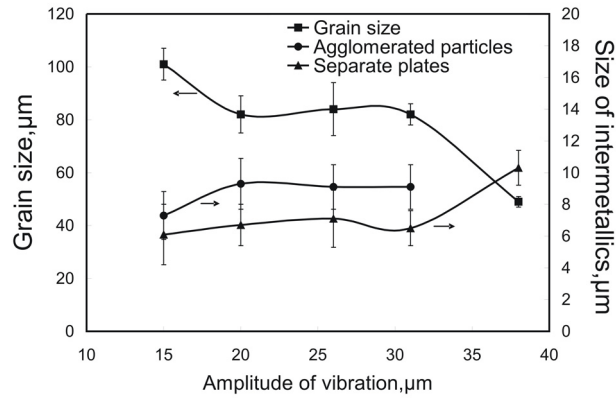
Figure 4.4 The effect of the amplitude of vibrations on the size of grains and intermetallics.

The separate plates usually appear in the center of the grains, as shown in Fig. 4.3 (b), which suggests that most of these plates acted as heterogeneous nucleation sites. Most of agglomerated particles consist of several fine intermetallics with the size ranging between 1-3 μm. The size of these fine intermetallics decreases with decreasing generator power as well. Although the agglomerated particles can also be found inside the grains, their distribution is much more random and does not have a clear association with the grain nucleation. Several agglomerated particles can be seen inside a single grain but at most one of these agglomerated particles could be the nucleation site, meaning the other ones were not active nucleation sites. As a result, the grain size decreases with increasing proportion of separate plates, i.e. with the increasing ultrasonic intensity, as illustrated in Fig. 4.4. The grain size in non-treated alloy was about 220 μm. UST with an amplitude of 38 μm applied during 10 s at 790 ˚C resulted in 4 times grain size reduction. These results suggest that the morphology and type of intermetallics may play a role in nucleation as important as their size and distribution. The separate plates might act much more easily as nucleation sites and promote the grain refining effect by heterogeneous nucleation than the agglomerated particles.

Based on this result, a higher power of ultrasonic generator is suggested for obtaining a better effect of grain refinement in the alloys containing Zr and Ti. Although stronger ultrasonic intensity means more ultrasonic energy input during ultrasonic processing, this heating effect can be neglected during short time ultrasonic processing.

The primary intermetallics shown in Fig. 4.3 resulted in dramatic grain refinement, however the presence of these particles is considered to be detrimental to the mechanical properties of aluminum alloys. The main purpose for this experiment and some previous experiments with 0.4 wt% Zr containing alloys was to observe these primary intermetallics clearly. So the amount of Zr was increased as compared to commercial alloys where the maximum allowable concentration of Zr is usually smaller. With this concentration the formation of intermetallics became obvious. In industrial application, only 0.18-0.25 wt%

Zr is recommended for ultrasonic aided grain refinement, because our previous experiments [1-6] and reported data [7] demonstrate that this amount of Zr is already sufficient for good grain refining effect without any risk of forming primary intermetallic particles of detrimental sizes.

4.3 Initial sonotrode temperature

When the melt first comes into contact with the sonotrode at the beginning of UST, the conditions of the sonotrode are of great importance, especially its initial temperature. On one hand, the Al melt can be cooled down or heated up depending on the temperature of the sonotrode. On the other hand, some primary phases might also form on the sonotrode surface if it is cold enough. In that case the detachment and dispersions of these phases due to the vibration of the sonotrode cannot be ignored.

In order to study these effects, three initial temperatures of sonotrode were selected for this experiment. The sonotrode was either at room temperature (20 ˚C), or preheated to 180 ˚C, or 400 ˚C by dipping it into overheated pure Al melt. These conditions are called 'cold sonotrode', 'warm sonotrode' and 'hot sonotrode', respectively, in this section. 7xxx based aluminum alloys were used with two concentrations of Zr, 0.1 and 0.17 wt%. Ti concentration was the same in all studied alloys, around 0.06 wt%. The melt was treated by ultrasound (4 kW) in the crucible (appr. 0.3 kg melt) for 10 s and then cast into a copper mold. Without UST, the melt was brought in contact with the warm sonotrode for 10 s before casting. The alloy compositions, casting procedures and recorded temperature conditions are summarized in Table 4.1.

Table 4.1. The alloy compositions, casting procedures and recorded temperature conditions in this research

Alloy	Composition, wt%				Used sonotrode and its temperature, ˚C	Initial melt temp. before UST, ˚C	Melt temp. after UST for 10 s, ˚C
	Cu	Mg	Zn	Additions			
7xxx based alloy	2.1	1.7	5.4	0.1 or 0.17 Zr+ 0.06 Ti	Cold, 20	710	687
					Warm, 180		693
					Hot, 400		705

Figure 4.5 gives the measured average grain size in the two studied alloys with and without UST. With decreasing the initial temperature of the sonotrode, the grain size decreased in both alloys containing different amount of Zr. Although the melt temperature after UST (casting temperature) was different, as shown in Table 4.1, the comparison of the microstructure without and with UST, both using the warm sonotrode and having then the same casting temperature, shows that UST clearly refines the grain structure. However,

enlarged temperature range of UST caused by lower initial sonotrode temperature might facilitate the formation of primary intermetallics, which can be suggested as one contributor for the refinement of grain structure.
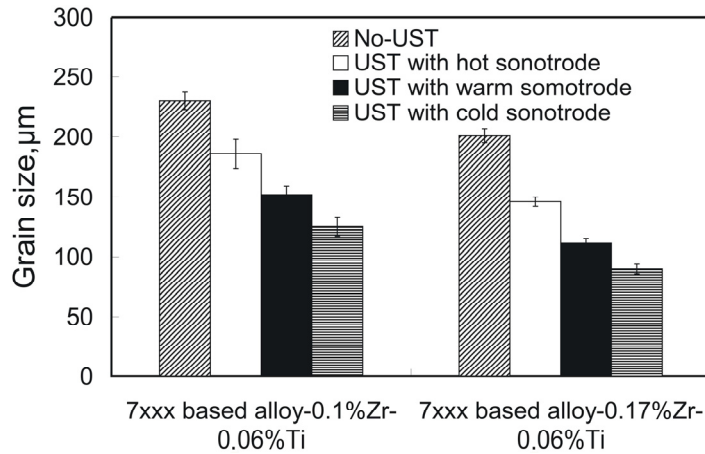
Figure 4.5 Grain size in the 7xxx based alloy with addition of Zr and Ti, after UST with the sonotrode at different temperatures.

The other factor which can produce this refinement is the detachment and dispersions of the phases growing on the sonotrode. Schematic view of this effect is illustrated in Fig. 4.6. The insertion of the sonotrode with a temperature below the liquidus will initiate the formation of crystals on the sonotrode, such as α-Al dendrites or primary intermetallics. The vibration of the sonotrode with high-frequency leads to a continuous growing and detachment of crystals from the surface of the sonotrode at the beginning of ultrasonic processing. These fragments can be distributed by acoustic streaming within the whole melt volume, increasing the number of nucleation site for heterogeneous nucleation. The lower the initial sonotrode temperature is, the stronger this effect.

Figure 4.6 Schematic view of the detachment of crystals from the sonotrode surface and cavitation in the melt.

When the initial sonotrode was preheated to high temperature, as shown in Fig. 4.5, the grain refining effect became weaker. This reflects the decreased proportion of "detachment" mechanism in grain refining. In the case of treating larger volumes or continuous treatment of melt flow, the sonotrode quickly acquires the temperature of the melt and the observed effects a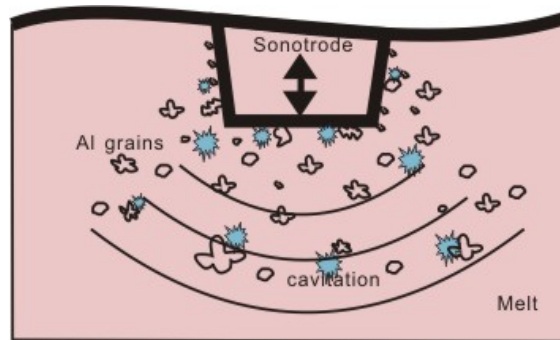re mostly due to the cavitation and acoustic streaming. The effect of the initial sonotrode temperature becomes insignificant. However, it is a very important factor that can dramatically influence the observed effects when the treated volume is small and the processing times are short. Thus, in industrial applications, certain amount of Zr (>0.18 wt %) would be necessary for a good ultrasonic refining effect.

4.4 The temperature of ultrasonic treatment

In Section 2.4, the temperature range of UST was found to play an important role. Ultrasonic processing at different melt temperatures directly influences the formation of primary intermetallics in the alloys containing Zr and Ti. In industrial application, this parameter is particularly important, because at different stages of industrial casting of aluminum alloys, the required melt temperature differs from place to place. This allows UST to be applied in several positions of casting, where appropriate. What is the optimized UST temperature? Or where is the optimum position for ultrasonic processing in industrial casting? The experiments used in this section were designed to study these questions.

In order to simulate the industrial casting process in a more realistic way than in Section 2.4, an ultrasonic processing setup with launder pouring system was designed, as shown in Fig. 4.7. The cross section of the launder is 6 cm × 5 cm with a length of 80 cm. In this experiment, the melt (appr. 1.0 kg) was poured into the launder, then passed under the ultrasonic horn and solidified in the steel mold (Ø50 mm × 250 mm, cooling rate 2 K/s).

The ultrasonic system was switched on (4 kW) before pouring. Temperature was monitored at both sides of the launder. The selected initial melt temperatures were 790 ˚C, 760 ˚C, 730 ˚C and 700 ˚C. Without UST, the melt was poured at 720 ˚C. 7xxx based alloys with addition of 0.2 wt% Zr and 0.07 wt% Ti were used in this study. The decrease of melt temperature when passing through the launder is summarized in Fig. 4.8. Note that in all cases the alloy was sufficiently fluid to fill the mould without any problems.
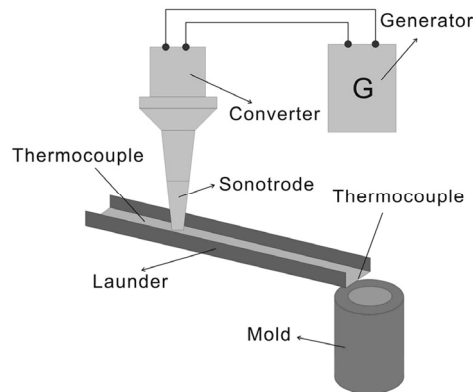
Figure 4.7 Schematic view of the experimental launder pouring system.
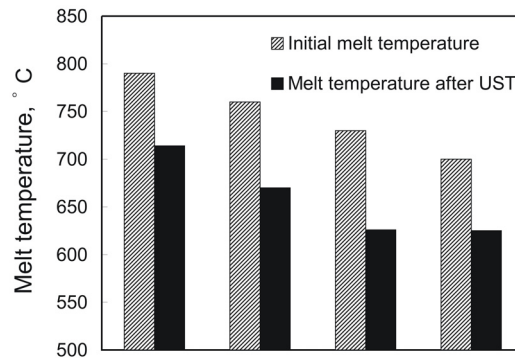
Figure 4.8 The decrease of melt temperature when passing through the launder,
monitored at both sides of the launder by thermocouple.

Figures 4.9 and 4.10 show the grain size and the structure of the studied alloys with and without UST. In non-treated alloy, the grains were dendritic and the grain size was about 350 μm. When UST was applied, the grain size decreased with decreasing pouring temperature; the grain size was smaller than 50 μm for a starting melt temperature of 700 ˚C. The morphology of grains started to change to globular at lower pouring temperature. The ultrasonic processing applied in lower temperature range of primary solidification is believed to create a higher amount of primary intermetallics, which results in better grain refining effect. This result also shows that under proper casting temperature, 0.2 wt% Zr is sufficient for promoting dramatic ultrasonic-added grain refinement.
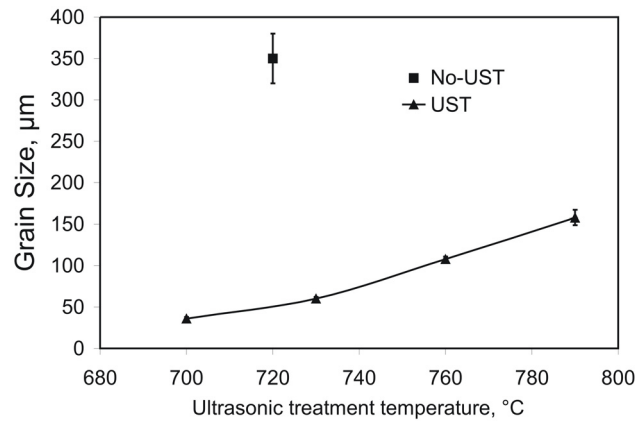
Figure 4.9 Effect of treatment temperature on grain size in 7xxx based alloys with addition of 0.2 wt% Zr and 0.07 wt% Ti cast through launder pouring system.

The ratio between ultrasonic treated volume and treatment time also determines the final grain structure in treated alloys. Generally, the active treatment occurs under the sonotrode tip, in a limited volume called cavitation zone. In these experiments with launder system, the passing time for a small elementary volume of the melt under the ultrasonic horn was less than 1 s as estimated from experimental setup. However, the treated volume at any time was small so that the ratio between ultrasonic treated volume and treatment time was small enough to result in significant grain refinement as seen in Fig. 4.9. Designing launder system in such a way that most of melt is able to pass through the cavitation zone increases the efficiency of UST effectively.

Therefore, for large amount of melt in industrial castings, it is suggested to apply ultrasonic processing in relative narrow spaces, such as in the launder. And the application of UST to the melt at a lower temperature is also recommended. Note that the typical casting temperature range for Al alloys during DC casting is 690-710 ˚C.
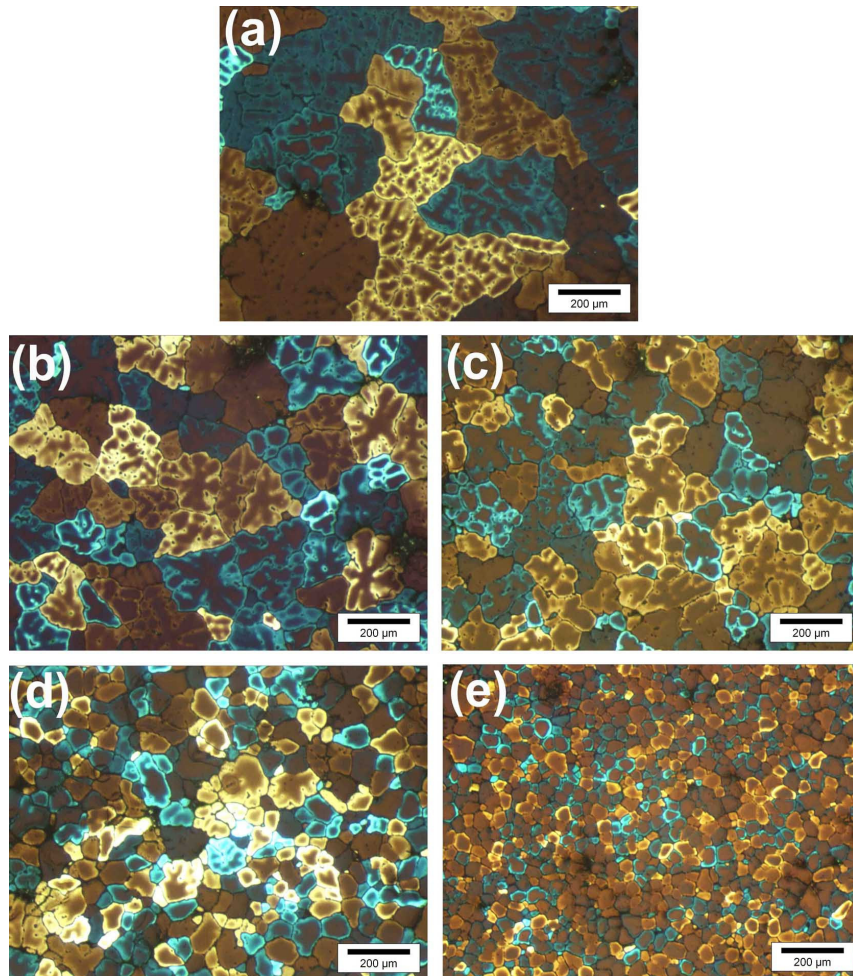
Figure 4.10 Grain structure in 7xxx based alloys with addition of 0.2 wt% Zr and 0.07 wt% Ti cast through launder pouring system: (a) No-UST, poured at 720 ˚C; (b) UST, poured at 790 ˚C; (c) UST, poured at 760 ˚C; (d) UST, poured at 730 ˚C and (e) UST, poured at 700 ˚C.

4.5 Holding time after UST

In previous sections, most of experiments were done by applying UST in the crucible. After the treatment, the melt was directly poured into the mold without any delay. However, in industrial casting, if ultrasonic processing is applied in the launder, as we suggested in previous section, the treated melt will not directly arrive to the mold after UST. It has to be transported over some distance before solidification. The same holds for foundries where the melt is usually treated in holding furnaces or ladles and then transported to the casting

mold. Thus, the effective survival of grain refinement effect after UST also needs to be considered.

An Al-2.5 wt% Cu alloy with 0.22 wt% Zr and 0.06 wt% Ti was used for this analysis. UST was applied in the crucible (appr. 0.2 kg melt) at 720 ˚C for 10 s. After UST, the melt was directly poured into a copper mold at 680 ˚C, or held in the furnace at 700 ˚C for 30 s, 60 s and 120 s, respectively. Without UST, the melt was poured at 720 ˚C.

The result shows a stable grain refinement effect in respect to holding time can be obtained after UST, as illustrated in Fig. 4.11. The grain size reduced from 280 µm to 60 µm on direct pouring after UST. With increasing holding time after UST, the ultrasonic-added grain refinement still remained significant.
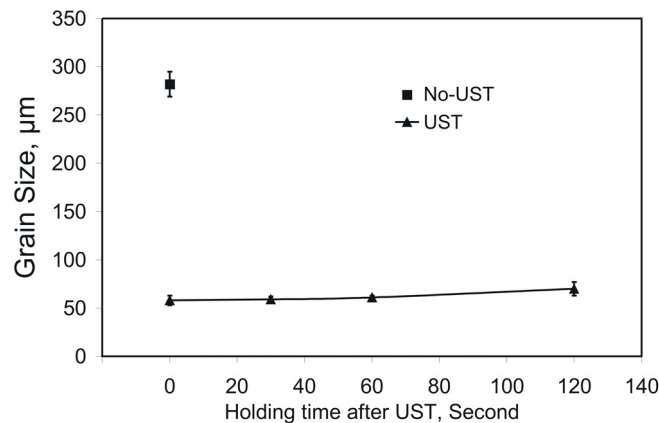
Figure 4.11 Effect of holding time at 700 ˚C after UST on the grain size of an Al-2.5 wt% Cu alloy with 0.22 wt% Zr and 0.06 wt% Ti.

Generally, two minutes is a considerable time in DC casting so these results are quite promising for this application. A stable effective duration of grain refinement after UST further increases the flexibility of the application of ultrasonic processing. The sonotrode does not necessary need to be located very close to the casting mold.

4.6 Cooling rate during solidification

4.6.1 Ultrasonic treated grain structure under different cooling rate

Cooling conditions are crucial to final microstructures in every casting process. For different purposes, cooling rate during solidification may vary considerably. In section 2.3.1, a graphite mold, giving a cooling rate of 0.8 K/s, was used in an Al-0.4 wt% Zr-0.12 wt% Ti alloy in order to observe the primary intermetallics more clearly than during tests with a higher cooling rate of 2.0 K/s. The results showed that the primary particles were refined from 50-100 μm without UST to 5-10 μm when UST was applied. However, an interesting phenomenon was found, which we did not cover in that section. The grain size after casting in the graphite mold increases from 115 μm in non-treated alloy to 185 μm in ultrasonic treated alloy. This is in opposition to significant grain refinement achieved in

other experiments described in Chapter 2 and in this chapter and also different to the coarsening effect in Chapter 3 when UST was applied close to eutectic temperature.

Looking back at all experiments in the alloys containing Zr and Ti, we can find that the major difference between the experiment which showed ultrasonic-aided grain refinement effect and those with grain coarsening effect is the cooling rate used during solidification. In all experiments where we observed ultrasonic-aided grain refinement effect, the cooling rate was around 2.0 K/s. Although refinement of primary particles by UST takes place in all experiments, no matter cast in a copper or graphite mold, the grain structure after UST was strongly dependent on the mold used. Why does cooling rate play such an important role in ultrasonic-related grain refinement?

In order to continue the analysis, a commonly used grain refiner Al3Ti1B master alloy was selected. Both methods of ultrasonic processing we used in the previous experiments (application in the crucible and in the launder) were applied again. A preliminary study of application of UST in DC casting was also performed with addition of the Al3Ti1B master alloy rod.

When UST was applied in the crucible, an AA2024 alloy was used with the addition of 0.02 wt% Ti in the form of an Al3Ti1B master alloy. The melt (appr. 0.5 kg) was treated from 750 ˚C to 700 ˚C for about 10 s. After UST, the melt was poured into a copper mold. Sample without UST was produced by casting from 720 ˚C. An AA7075 alloy with the addition of Al3Ti1B master alloy was cast in steel mold with launder pouring system under the same conditions as described in Section 4.4. The pouring temperature in the launder was 750 ˚C.

Table 4.2. Casting conditions of experiments using Al3Ti1B mater alloy

Alloy	Composition, wt%				Location of UST, ˚C	Mold	Cooling rate, K/s
	Cu	Mg	Zn	Additions			
AA 2024	3.3	1.3	-	0.02Ti as Al3Ti1B	Crucible	Copper mold	2.0
AA7075 alloy	1.5	2.1	5.4	0.01Ti as Al3Ti1B	Launder pouring system	Steel mold	2.0
Al-Cu	3.9	-	-	0.03Ti as Al3Ti1B	Launder during DC casting	Direct chill mold	6.0

In addition, DC casting of an Al-3.9 wt% Cu alloy was also performed with addition of the Al3Ti1B master alloy rod. The UST was applied in the launder during DC-casting, in a similar manner as during smaller scale experiments with the launder pouring system. A

1500-mm long billet was cast in a 200-mm hot top mold at a casting speed of 100 mm/min. Melt temperature in the furnace was 727 ˚C, melt temperature in the launder was 693 ˚C. The DC casting experimental setup used in this experiment is described in detail in Ref [1]. The detailed casting conditions of experiments using Al3Ti1B master alloy are summarized in Table 4.2.

When Al3Ti1B master alloy was added in typical quantities, the UST did not lead to additional grain refinement in the AA2024 alloy, as shown in Fig. 4.12. The grain size after UST even increased from 116 to 138 μm. Similar results were obtained when UST was applied to the AA7075 alloy with addition of Al3Ti1B while casting with launder pouring system. However, the grain size after UST decreased two-fold, from 60 to 30 μm, in the Al-Cu alloy with Al3Ti1B addition when UST was applied upon DC casting.

What did exactly make this difference? Before answering this question, let's summarize all representative results of the previous sections with respect to the cooling rate used during solidification. With taking the cooling rate into account, the mechanism behind the results might be more evident.
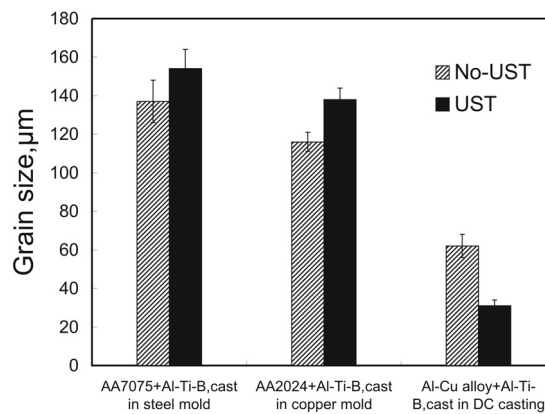
Figure 4.12 Grain size in the aluminum alloys with addition of Al-Ti-B master alloy, solidification under different cooling rate.

4.6.2 Discussion

Figure 4.13 presents a summary of all selected results obtained under different cooling rates and described in previous sections. Both cooling rate and potential substrates seem to greatly influence whether grains are refined or coarsened. Let first have a look at the cases with potential substrates $Al_3(Zr,Ti)$ and Al_3Ti.

The results in Sections 2.3 and 2.4 show clearly that UST refines primary intermetallics, which potentially may increase the number of nucleant particles, promoting heterogeneous nucleation. However, it is well known that the smaller size of primary particles requires larger undercooling for their activation according, e.g., to athermal heterogeneous nucleation theory [8]. Therefore, the distribution of primary particle sizes results in a distribution of required undercoolings.
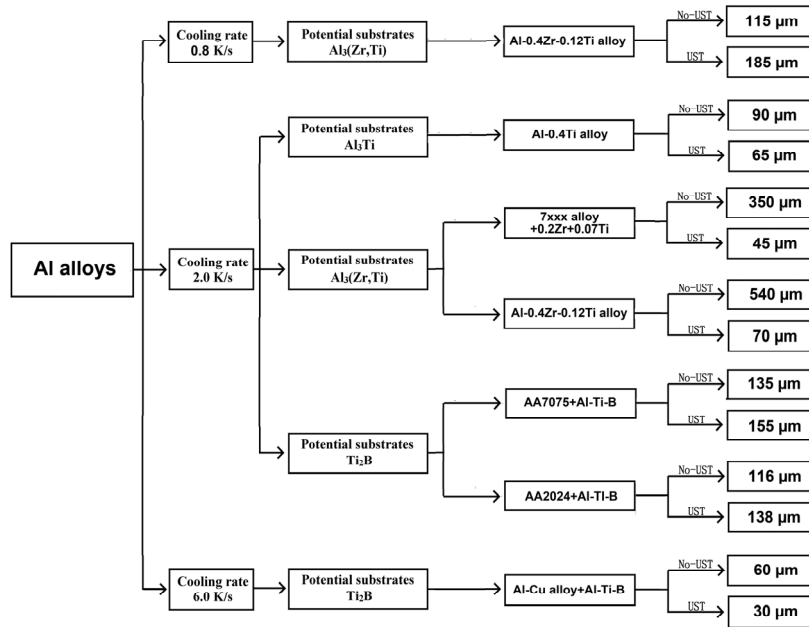
Figure 4.13 A flow chart of all representative results with final grain size from the previous sections with respect to the cooling rate.
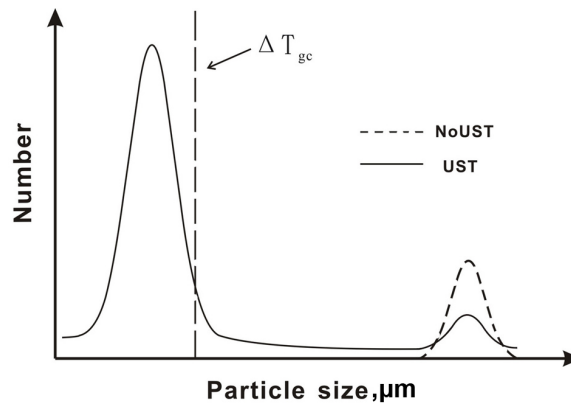
Figure 4.14 Schematic view of the effect of ultrasonic melt treatment on size distribution of particles. ΔT_{gc} is critical undercooling for nucleation under UST.

Figure 4.14 shows schematically the effect of UST on particles size distribution. When UST is applied, the main peak of particle size distribution shifts largely to the left, since most of primary particles are getting smaller. Simultaneously, the number of large particles decreases. To explain the effect of grain refinement, we assume that there is a critical undercooling ΔT_{gc} above which most of small primary particles produced by UST are not

79

activated. In our experiments, the primary particles after UST became about 3-10 μm in size in both the Al-Ti and Al-Zr-Ti alloys, which corresponds to the critical undercooling ΔT_{gc} of 0.044 K as estimated using Eq. (1.1). Usually in casting practice, the undercooling achieved during casting of aluminum alloys in metallic molds is about 0.2 K [9]. So the undercooling ΔT upon solidification in the copper mold should be more than ΔT_{gc} of 0.044 K. This is consistent with the observed effect of UST in the Al-0.4 wt% Ti alloy and in the Al-0.4 wt% Zr-0.12 wt% Ti alloy when they were cast in the copper mold (2 K/s): the refinement of primary intermetallics resulted in refining effect on Al grains. As shown in Fig. 2.7 and Fig. 2.14, the grain size reduces from 90 to 65 μm in the Al–0.4 wt% Ti alloy, and from 540 to 70 in the Al-0.4 wt% Zr-0.12 wt% Ti alloy, when UST was applied. The constitutional undercooling effect caused by Ti might further enhance the nucleation potency for fine Al_3Ti particles.

However, in the case of the lower cooling rate in the graphite crucible, the grain size increases from 115 μm without UST to 185 μm when UST is applied to the Al-0.4 wt% Zr-0.12 wt% Ti alloy.

When looking at these results from the positions of required undercooling and substrate size, it appears that the absence of grain refinement upon slow cooling can be logically explained. On one hand, the undercooling in the experiment with the low cooling rate might be less than the critical undercooling ΔT_{gc} (situation depicted in Fig. 4.14), which means that the undercooling is not enough to activate those smaller intermetallics fragmented by UST. As a result, the grain size increases with intermetallic refining because less large particles are available for nucleation when UST was used. On the other hand, UST promotes the dissolution of Ti in Al_3Zr particle, increasing the interfacial energy between α-Al and Al_3Zr particles [6]. The larger interfacial energy results in an even higher heterogeneous nucleation energy barrier. The increased heterogeneous nucleation energy barrier may lead to the delay of nucleation to larger undercooling. As a result, the activation of more refined particles and, consequently, greater grain refining effect requires larger undercooling such as has been apparently achieved in the Al-0.4 wt% Ti alloy and in the Al-0.4 wt% Zr-0.12 wt% Ti alloy cast in a copper mold. However, if the undercooling is too low, the efficiency of UST may be inhibited or even UST may produce the opposite effect than wanted.

As discussed above, UST increases the number of potent nucleants and promotes grain refinement under appropriate casting conditions. So in the experiments with the 7xxx based alloy containing Zr and Ti and cast in the steel mold (2 K/s) after UST in the melt flow in the launder, it was assumed that UST would produce fine Al_3Zr particles which would be activated by the sufficient undercooling and facilitate grain refinement (Fig. 4.10). Similar results in the Al-Cu alloy containing Zr and Ti also can be found in Fig. 4.11. However, the same experiment with the AA7075 alloys but performed with TiB_2 additions instead of Zr and Ti did not produce any additional grain refinement after UST (Fig. 4.12). Neither did the experiment with the AA2024 alloy with TiB_2 addition cast in the copper mold with the same cooling rate 2 K/s. Only DC casting of the Al-Cu alloy with TiB_2 additions demonstrated considerable grain refinement after UST. So what is responsible of the difference?

To answer this question, the cooling rate and the mechanism of grain refinement by TiB_2 should be firstly considered. Generally, it is accepted that TiB_2 acts as nucleation site for the α-Al phase either directly or through the Al_3Ti layer which is consumed during further solidification [10-12]. The average TiB_2 particle size in a commercial Al3Ti1B grain refining rod is around 1 μm [13], which corresponds to the critical undercooling ΔT_{gc} of 0.36 K. According to the typical achievable undercooling 0.2 K, the most active TiB_2 particles should have a size larger than 5 μm. In addition, titanium borides are usually agglomerated and only a fraction of them is available as nucleation sites under typical casting conditions. According to the athermal heterogeneous nucleation theory, finer TiB_2 particles means that a larger undercooling is needed for their activation. The UST might disperse agglomerated TiB_2 particles, which would result in finer separated particles thus increasing the demand for greater undercooling ΔT_{gc} in the solidification process. In casting, larger undercooling usually results from a higher cooling rate. DC casting may provide just that – the measured cooling rate is 6 K/s versus 2 K/s in metallic molds used. Therefore, when the steel or copper mold was used (relatively low cooling rate compared to the DC casting), less percentage of TiB_2 particles and only the larger ones could act as nucleation sites because of dispersion of TiB_2 particles caused by UST. However in DC casting the undercooling might be large enough to activate at least part of these dispersed TiB_2 particles, increasing the amount of nucleants and reducing the grain size in the DC-cast alloy.

Through these results, we can see that although UST can refine the intermetallics dramatically when it is applied in the temperature range of their primary solidification, whether these particles can be involved in further solidification process and result in further grain refining effect in aluminum alloys depends on the undercooling achieved during solidification. Thus, high cooling rate is suggested in order to get a better ultrasonic-aided grain refinement in application of ultrasonic processing. In the cases of lower cooling rates during casting, other mechanisms of UST may be utilized instead of dispersion of substrates.

4.7 Conclusions

In this chapter, a more precise understanding of the mechanism of UST was obtained by studying the influence of the parameters of ultrasonic processing on the as-cast microstructure. This knowledge is of great importance for further industrial application of ultrasonic processing. Through the analysis, several suggestions can be presented based on the improved understanding of ultrasonic-aided grain refinement.

(1) A minimum amount of Zr (>0.18 wt %) is necessary for a good ultrasonic refining effect. However, excessive Zr will result in the presence of large particles, visible by optical microscopy, which are considered to be detrimental to the mechanical properties of aluminum alloys. Thus, the composition range 0.18-0.25 wt% Zr is suggested for ultrasonic-aided grain refinement. This amount of Zr is already sufficient for a good grain refining effect without any risk of including too large primary intermetallic particles.

(2) The use of highest ultrasonic power available from the experiment is suggested for obtaining a better effect of grain refinement in the alloys containing Zr and Ti, unless the introduction of ultrasonic energy causes the undesired increase of the melt temperature.

(3) For treating large amounts of melt encountered in industrial castings, it is suggested to place the sonotrode in relative narrow spaces, such as in the launder, to ensure all the melt flows close to it and is treated by ultrasound.

(4) The application of UST to the melt at low enough temperature is recommended to optimize the grain refinement. The sonotrode is not necessary to be located very close to the solidification mold because the effect of ultrasonic processing on the melt remains for a certain time after the end of UST and will still influence the solidifying microstructure.

(5) High cooling is suggested for getting a better ultrasonic-aided grain refinement in application of ultrasonic processing.

References

[1] T.V.Atamanenko, *Cavitation-aided Grain Refinement in Aluminum Alloys*. 2010, Delft Univeristy of Technology: Delft.

[2] L.Zhang, D.G.Eskin, A.Miroux, and L.Katgerman, *IOP Conf. Ser.: Mater. Sci. Eng*, 2012. **27,012002**: p. 1-6.

[3] L.Zhang, D.G.Eskin, A.Miroux, and L.Katgerman. in *13th International Conference on Aluminum Alloys*. 2012: TMS, p. 1389-1394.

[4] L.Zhang, D.G.Eskin, and L.Katgerman, *J. Mater. Sci.*, 2011. **46**: p. 5252-5259.

[5] T.V.Atamanenko, D.G.Eskin, L.Zhang, and L.Katgerman, *Metall. Mater. Trans. A*, 2010. **41A**: p. 2056-2066.

[6] T.V.Atamanenko, D.G.Eskin, M.Sluiter, and L.Katgerman, *J. Alloys. Comp.*, 2011. **509**: p. 57-60.

[7] G.I.Eskin, *Ultrasonic Treatment of Light Alloy Melts*. 1998, Amsterdam: Gordon and Breach Science Publishers.

[8] J.A.Dantzig and M.Rappaz, *Solidification*. 2009, Boca Raton: CRC Press.

[9] T.E.Quested and A.L.Greer, *Acta Mater.*, 2004. **52**(3859-3868).

[10] A.L.Greer, P.S.Cooper, M.W.Meredith, W.Schneider, P.Schumacher, J.A.Spittle, and A.Tronche, *Adv. Eng. Mater.*, 2003. **5**: p. 81-91.

[11] M.Easton and D.Stjohn, *Metall. Mater. Trans. A*, 1999. **30A**: p. 1613-1623.

[12] P.Schumacher, A.L.Greer, J.Worth, P.V.Evans, M.A.Kearns, P.Fisher, and A.H.Green, *Mater. Sci. Technol.*, 1998. **14**: p. 394-404.

[13] W.A.Schneider, T.E.Quested, A.L.Greer, and P.S.Cooper, *Light Metals 2003*, P.N.Crepeau, Editor. 2003, TMS: Warrendale, PA. p. 953-959.

Chapter 5

Application of ultrasonic processing in DC casting

5.1 Introduction

In previous chapter, the parameters of ultrasonic processing have been studied systematically, which provides a good foundation for further industrial application of ultrasonic processing. In this chapter, we will present the results of the preliminary research of ultrasonic processing in DC casting.

As we introduced in Chapter 1, DC casting is the most widely used technology for producing aluminum ingots and billets for further manufacturing processing. The commercial use of DC casting could be dated back to the 1930s. Several important developments in this casting technique were made in the past 80 years in order to refine grain structure, alleviate macrosegregation, prevent the formation of cracks and increase productivity [1].

The main casting process parameters in this technology, such as casting speed, casting temperature, melt flow feeding system and cooling water flow conditions, are crucial to the evolution of microstructures during solidification, as well as for the formation of defects. Generally, a higher casting speed results in a finer microstructure [2-5], but in more severe macrosegregation and higher cracking susceptibility, while cooling water-flow rate has relatively minor effect on these features [6, 7].

The application of ultrasonic processing in continuous casting of aluminum alloys is not a new area of study. Several successful attempts have been done in order to refine the grain structure or alleviate the macrosegregation, thus improving the casting quality of billet/ingot [8-10]. Fig. 5.1 shows an example of the AA2324 billet obtained by casting with ultrasound in the Soviet Russia in the 1980s. Nondendritic grain structure was achieved in this billet according to the report [10]. Not only grain refinement in the billet/ingot, but also surface quality and macrosegregation can also be improved by ultrasonic processing in large casting billets/ingots [8].

Figure 5.1 A billet with non-dendritic grain structure produced using UST (an AA2324 alloy, diameter 1200 mm, weight 10 t) [8, 10].

This industrial research showed a promising perspective for the application of ultrasonic treatment (UST) in continuous casting. However, the specific technological details of continuous casting with UST are not fully reported and the mechanisms of structure modification are still not fully clear. In addition, in order to obtain a uniform grain refinement over the billet/ingot cross section, several ultrasonic sources were used in the liquid pool of the billet. This increases the difficulty of sonotrode design and the cost of the casting, which restricts the real industrial application of ultrasonic processing.

The aim of this chapter is to improve the efficiency of ultrasonic processing in DC casting through a further study this technology based on our results reported in previous chapters. The distribution of alloying elements in a billet cast under UST was investigated as well. In order to analyze the mechanism of UST on macrosegregation in DC casting, an extended research was preformed using different melt feeding schemes applied in real industrial scale DC casting. The results of this extended research are very helpful for us in understanding the mechanism of macrosegregation under ultrasonic processing.
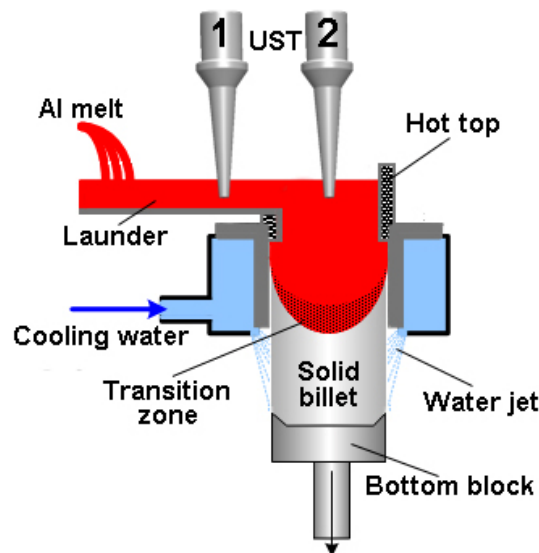
Figure 5.2 A simplified schematic view of DC casting installation used in this experiment. UST was performed either in the launder (1) or in the hot top (2). Modified from [11].

5.2 Experimental procedure

The DC casting installation used in this experiment was located at TU-Delft. A simplified schematic view of this set up is shown in Fig. 5.2. The molten metal was first prepared in an electrical resistance tilting furnace (up to 200 kg of aluminum melt). During DC casting, the melt was delivered into a water-cooled mold (with a hot top made of refractory material) through a launder, which was usually preheated to about 700 ˚C before casting. The water-cooled mold was made of aluminum alloy with a diameter of 200 mm and an effective

mold height of 20 mm. When the solidified shell was formed around the mold wall and at the bottom of the mold due to the primary cooling, the bottom block was then steadily withdrawn using a hydraulic moving system (a maximum length of 1200 mm). The tilting of the furnace, melt level in the launder and in the hot top were controlled by a melt level laser sensor during whole casting. All casting parameters, including melt temperature, melt level, water flow rate and casting speed etc. were recorded by a data acquisition system (National Instruments).

UST was performed either in the launder or in the hot top, as illustrated in Fig. 5.2. The detail casting conditions will be introduced in each section.

The extended analysis using different melt feeding schemes was preformed at Tata Steel Europe, the Netherlands. The details of that DC casting installation will be introduced in the relevant section.

5.3 Ultrasonic processing applied in the launder during DC casting

5.3.1 Water-model optimization of UST

Before performing the ultrasonic processing in DC casting, the first question that comes into mind is how to increase the volume percentage of treated melt when the melt continuously passes through the launder. As shown in Chapter 4, a good grain refinement was achieved when UST was applied to small volume of the melt in the crucible or in the small launder. However, the width of the launder in real DC casting setup usually is much larger than the diameter of the sonotrode. This means not all melt passes through the effective cavitation zone under the sonotrode tip. The simplest way to deal with this problem is increasing the diameter or the number of sonotrodes in the launder, but it leads to the increasing complexity of ultrasonic equipment and the rising of the costs. A probable alternative solution is the modification of launder in order to force more melt to pass through the cavitation zone under the sonotrode. It seems to be a feasible method, however, few reports are available on this topic.

In this research, water modeling of the melt flow using water instead of liquid aluminum, a transparent launder, a transparent hot top and ultrasonic equipment was preformed in order to establish the flow pattern around the sonotrode and to find favorable conditions for UST in the launder. The experimental setup is shown in Fig. 5.3 (a). The water was continuously running from the upper end of the launder (left in Fig. 5.3) to the entry of the hot top (right in Fig. 5.3). The water flow rate was selected to be 3.14 l/min (corresponding to casting speed 100 mm/min in our DC casting set up for a billet 200 mm in diameter), and was controlled by a water flow meter. The water level in the transparent launder remained the same (40 mm to the bottom) in all experiments, which was similar to the melt level in the launder during DC casting. The sonotrode was located in the launder close to the transparent hot top.
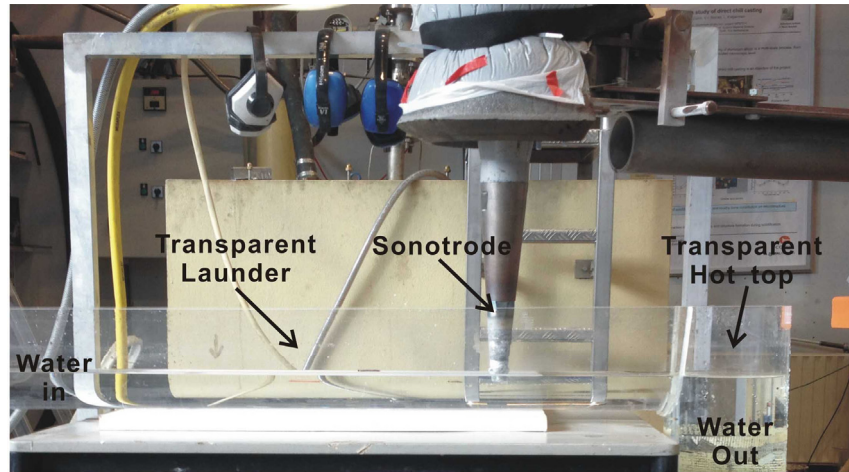
(a)
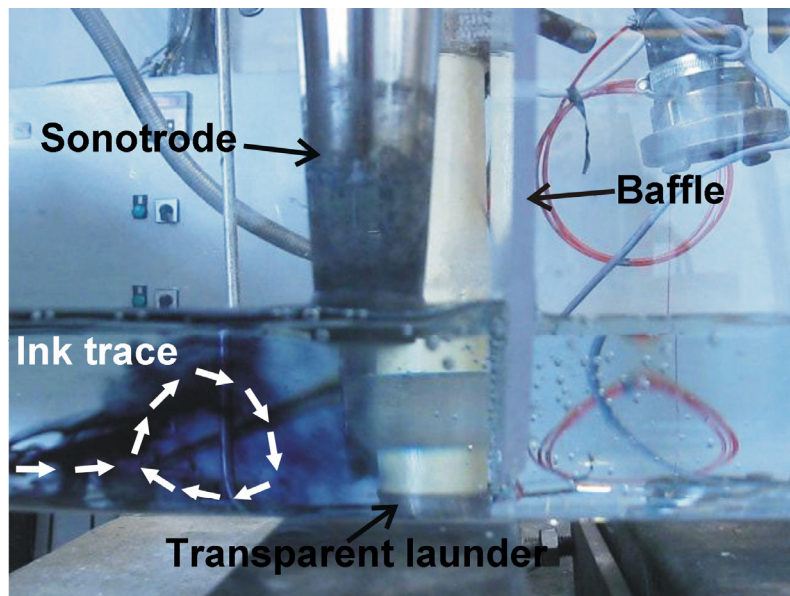
(b)

Figure 5.3 Water modeling setup: (a) the transparent launder and hot top used in this study and (b) ink trace during water modeling. Melt flow from the left to the right. A convection flow caused by UST was clearly shown using white arrows.

During the experiments, black/blue ink was added drop by drop on the upstream part of the launder. The movement of the ink passing through the ultrasonically treated area was recorded by a camera. An example is illustrated in Fig. 5.3 (b).

The first factor we analyzed using water modeling was the submerging depth of sonotrode in the melt. Fig. 5.4 is a schematic view of typical flows created by ultrasonic horn at different submerging depths. The increasing depth of sonotrode in the water decreased the treated area under the sonotrode tip and created a larger secondary convective flow. Generally, the active treatment occurs under the sonotrode tip, and the secondary flow is considered to have minor effect on structure refinement. In addition, the strong secondary flow near the surface area can easily entrain the oxide film into the melt, which is always not desired during casting processing. So through these results, the smaller submerged depth of the sonotrode is better.
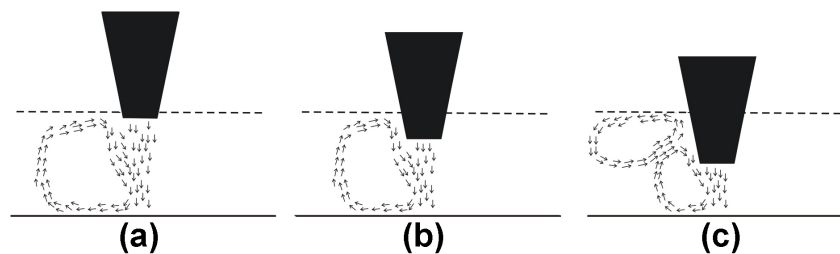
Figure 5.4 Flow patterns under different submerged depth of sonotrode: (a) 3mm, (b) 10 mm and (c) 20 mm. Melt flow from the left to the right.

Different designs of baffles in the launder were studied as well, in order to optimize the flow for ultrasonic treatment conditions in DC casting launder. A definite change of the flow patterns for different designs under ultrasound can be observed in the videos and are shown schematically in Fig. 5.5. Although the quantitative information cannot be provided in this experiment, it is clearly shown from the recorded videos/movies that with the confined space under the sonotrode tip, such as the designs in Fig. 5.5 (d) and (h), the ultrasonic treatment was more effective because in these designs, the convective flows were observed to be constrained under the sonotrode tip and the dispersion of the ink was more violent and rapid.

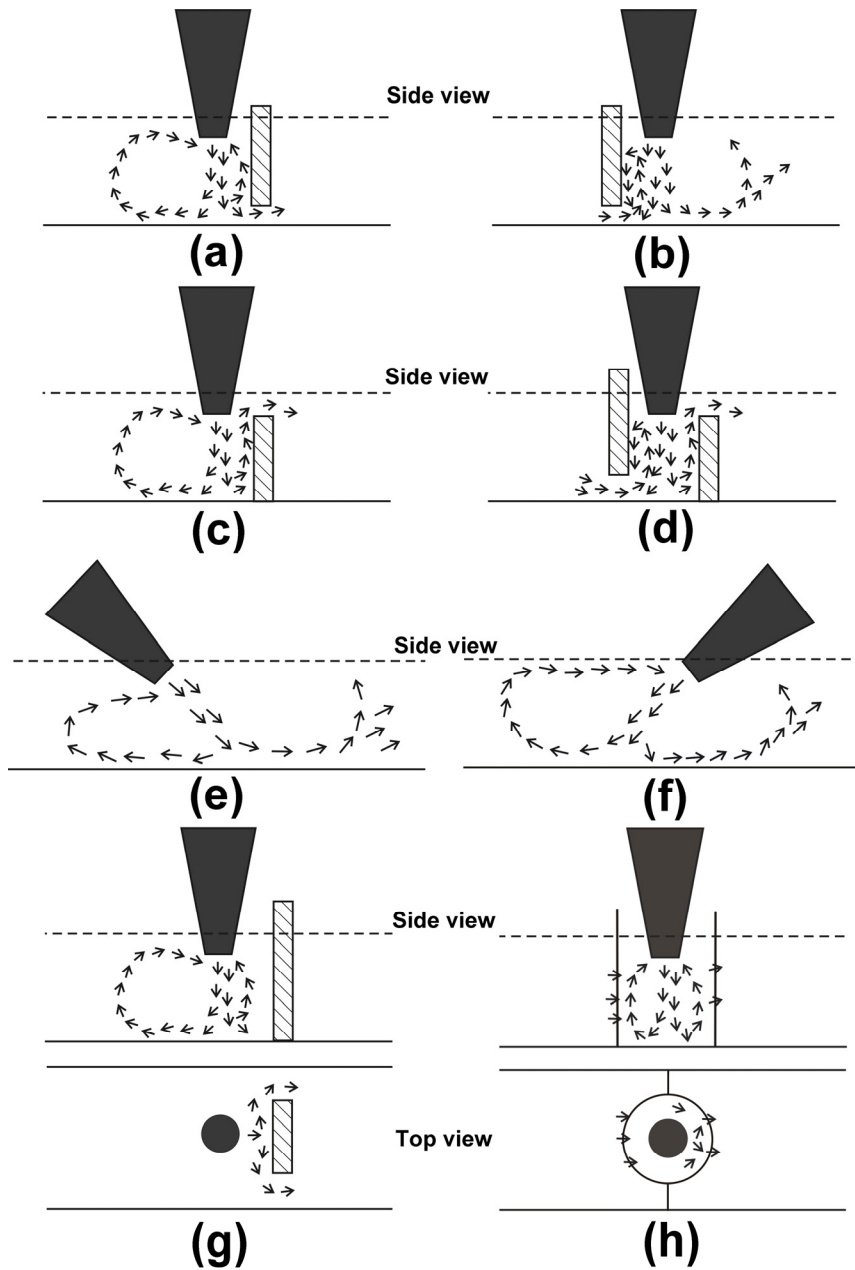Figure 5.5 Flow patterns under different baffle designs: (a),(b),(c),(d),(e),(f) side view, baffles were across the whole width of the launder. (g) and (h) top view and side views respectively. The main flow is from left to right.

5.3.2 UST in the optimized launder design

According to the water modeling results in previous section, the baffle design in Fig. 5.5 (d) was selected for up-scaling DC casting. The real baffle design in our DC casting launder is shown in Fig. 5.6. The ultrasonic horn was placed at the center between the baffles during DC casting. An AA7050 billet with the addition of 0.12 wt% Zr and 0.08 wt% Ti was cast at a casting speed of 100 mm/min. Melt temperature in the furnace was about 720 ˚C and melt temperature in the launder was about 690 ˚C. After casting a certain length of the billet without UST, ultrasound was switched on until the end of casting. The water flow rate was maintained constant at 140 l/min.
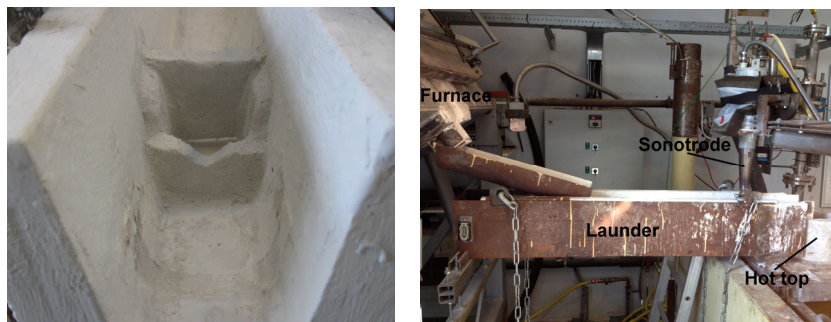
Figure 5.6 The baffle design in DC casting launder (left). The width of launder is 110 mm. The right picture shows the set up during DC casting with UST.

Two slices were cut from the billet in positions where the steady state was reached for both cases of with and without UST. The slices were then cut into smaller samples across the billet diameter in order to analyze the microstructure from the surface to the center of the billet.
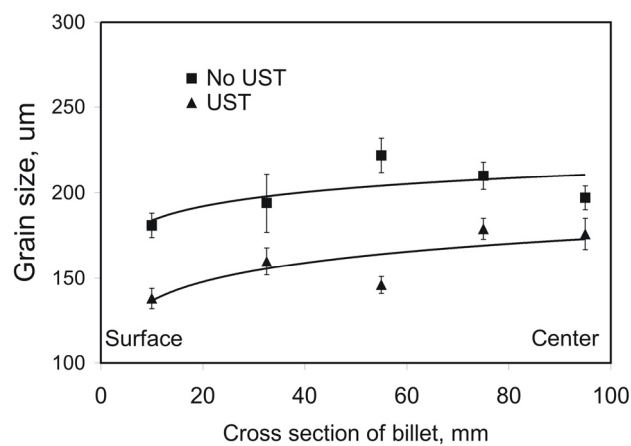
Figure 5.7 Distribution of grain size in DC casting billet across the billet radius with and without UST.

Figure 5.7 gives the distribution of grain size from the surface to the center. The average grain size decreased clearly when UST was applied in the launder. The grain structures for both conditions across the billet radius can be found in Fig. 5.8. Although this refinement was less significant as compared with small scale experiments in Chapters 2 and 4 due to the lower amount of Zr and time/volume ratio of treated melt, it still confirmed that the baffle design used in this experiment had positive effect of grain refinement caused by UST, and also showed some potential for improving baffle design for a better grain refinement. Its should be noted that improper baffle designs in the launder were reported to even result in structure coarsening in DC casting of aluminum alloy [12].
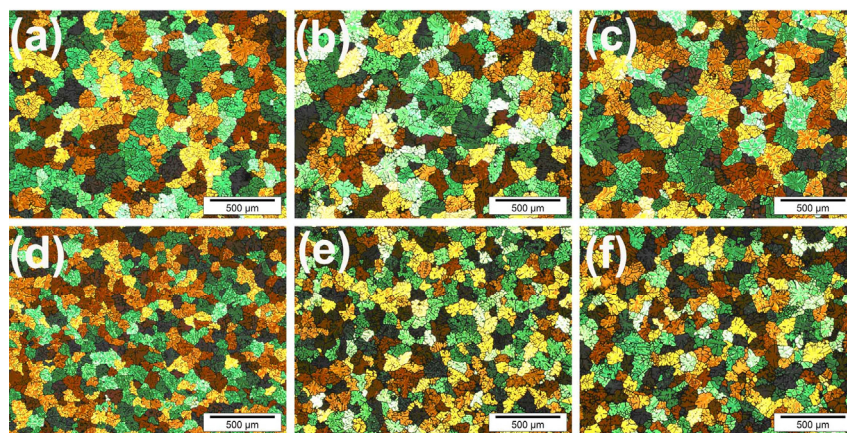
Figure 5.8 Grain structure in the horizontal section of the DC casting billet: (a) near the surface, 10 mm away from the surface, No-UST; (b) quarter of the billet, 55 mm away from the surface, No-UST; (c) in the center, No-UST; (d) near the surface, 10 mm away from the surface, UST; (e) quarter of the billet, 55 mm away from the surface, UST; (f) in the center, UST.

5.4 Ultrasonic processing applied in the hot top and extensional analysis

5.4.1 UST applied in the hot top

In this study, the UST was placed in the center of the hot top instead of in the launder during DC casting. The experiment was preformed together with Dr. T. Atamanenko, who was supervised by Prof. L. Katgerman and Prof. D.G. Eskin during her PhD study at TUDelft.

An Al-3.7 wt% Cu-0.21 wt% Zr-0.06 wt% Ti alloy was used for this experiment. The casting speed was 100 mm/min and cooling water flow rate was 160 l/min. At least 300 mm of billet were cast either without or with UST applied in the hot top.

After analyzing the billet, it was found that UST in the hot top still resulted in 50% decrease in grain size. The structure after treatment was homogeneous, equiaxed and dendritic. The detail structure information can be found in [12].

The most interesting result obtained in this experiment was the macrosegregation pattern across the billet diameter when UST was applied in the center of the hot top, as shown in Fig. 5.9.
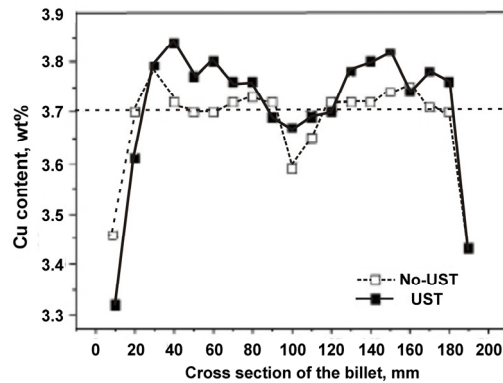
Figure 5.9 The distribution of Cu concentration across billets diameter with and without UST in the hot top [12].
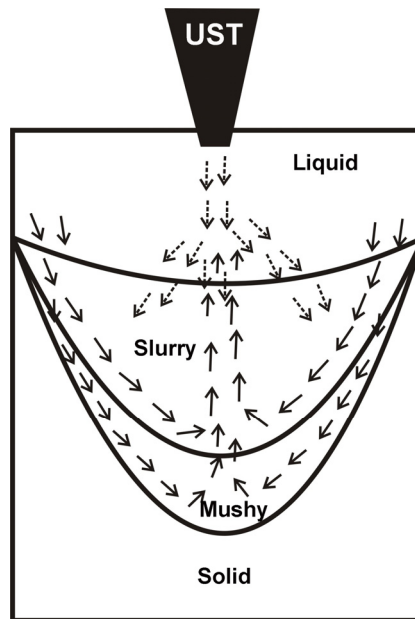
Figure 5.10 A diagram showing the mechanism of macrosegregation when UST was applied in the hot top. Solid arrows: the thermosolutal convection; dashed arrows: the downward acoustic streaming caused by UST.

A decrease of deviation of Cu concentration in the center of the billet can be found in the ultrasonic treated billet, while a stronger positive segregation appeared at mid-radius. The

changing of flow patterns in the transition region is believed to be the main reason for the decrease of Cu segregation in the center. As we introduced in Chapter 1, the thermosolutal convection, on one hand, pushes the solute-rich liquid ($k<1$) from the surface to the center, and causes the positive centerline segregation. On the other hand, the upstream flow in the center will take the solute-rich liquid out of the central transition zone back to the liquid pool. The downward acoustic streaming caused by UST in the center of hot top forced this solute-rich liquid back to the transition regions in the center or at mid-radius, which compensated for the shrinkage-induced negative segregation in the center and enhanced the positive segregation at mid-radius. A schematic view of this mechanism is shown in Fig. 5.10.

5.4.2 Modification of flow pattern during DC casting

The results in previous section clearly show the potential of controlling the macrosegregation in DC casting billet by modifying the melt flow during casting. This effect was also confirmed by other investigators in our research group, who successfully applied forced flow to modify the macrosegregation by using a mechanical flow control device (pump) [13, 14]. The results showed that with proper downward forced flow along the centerline of a billet, the macrosegregation can be suppressed significantly.

Looking into this result, the following question naturally came into our mind: Can UST produce the same effect than the pump on macrosegregation under proper casting conditions? If the answer is 'Yes', then the application of UST in DC casting not only has the potential to refine the grain structure but also can simultaneously alleviate the macrosegregation .

It seems to be a very interesting subject for industry and definitely worth further investigating, however, the limitation of our laboratory scale ultrasonic setup restricts further upscaling, since it cannot provide enough powerful streaming for a large scale DC casting.

Therefore, as an alternative, two industrial round AA7050 DC casting billets were cast with different melt feeding schemes at Tata Steel Europe, the Netherlands, in order to simulate the application of powerful UST at different positions in the liquid pool during DC casting.

The diameter of cast billets was 315 mm. The melt was first degassed in the furnace at 730 ˚C and then cast with a conventional DC casting mold without hot top. The casting temperature was around 680 ˚C. Both billets were grain refined by the same amount of an Al5Ti1B master alloy, 2 kg/tonne, in order to simulate the potential grain refining effect caused by ultrasonic processing.

Two melt feeding distributors were used. The melt was poured to the DC casting mold from the launder either through a semi-horizontal feeding distributor or a vertical feeding distributor, as shown in Fig. 5.11 (a) and (b).

In the semi-horizontal feeding scheme, the melt was diverted to four branches through a cross-shaped splitter. The changing of melt flow pattern caused by this semi-horizontal feeding can represent the similar effect caused by four evenly distributed ultrasonic sonotrodes at mid-radius.

In vertical feeding scheme, all melt was poured directly in the center of the mold. The result from this billet might provide us similar information as when powerful UST was applied in the center of casting mold. The detailed casting information at the steady state casting and the average alloy composition are shown in Table 5.1.
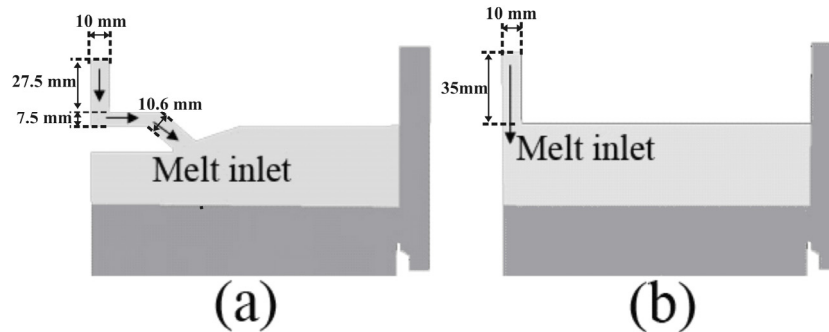

Figure 5.11 Geometry of melt feeding distributors used in experiments: (a) semi-horizontal melt feeding scheme; and (b) vertical melt feeding scheme. Only half of the billet is shown, centerline is on the left.

Table 5.1. The composition and casting parameters of the billets

Alloy	Composition, wt%					Melt feeding scheme	Casting speed, mm/min	Cooling water flow rate, l/min
	Cu	Mg	Zn	Zr	Ti			
AA 7050	2.2	2.1	6.2	0.13	0.03	Semi-horizontal	50	40
						Vertical	50	35

In order to analyze the effect of melt feeding geometry on flow pattern during DC casting and how these modified flow patterns in the liquid and transition regions affect microstructure and macrosegregation, computer simulation was also performed using ALSIM6 (a casting-simulation software developed by the Norwegian Institute for Energy Technology, Kjeller, Norway). The simulated geometry consisted of the mold, water jet, bottom block and the casting moving domain (i.e. Arbitrary Eulerian–Lagrangian description domain). In this 2D computer simulation, the heat, fluid flow, mechanical properties, casting and solidification modules were included in the ALSIM6 modeling set-up. The ALSIM program also calculates the heat transfer along the billet wall from the cooling water flow rate. The air gap formed between the mold and billet, which reduces the heat transfer, is also taken into account for heat transfer calculation. On average the heat transfer is found to be higher for the semi-horizontal feeding than for the vertical feeding geometry. The Navier–Stokes equations are solved in the model by considering a Darcy solidification term. Low Rayleigh number (LRN) turbulent energy-pseudoturbulent dissipation (κ-ε) model was chosen to solve the turbulence problem in this simulation. The

94

velocity of the solid phase is equal to the casting speed throughout the transition region. A more detailed description of the software setup and models involved can be found elsewhere [15, 16]. The thermo-physical parameters for AA7050 alloy and mechanical database used in this simulation are given in Refs. [17-19].

The fully understanding of this experiment both through experiments and computer simulation will help us to further understand the effect of UST in DC casting and point the way to the next step for real DC casting trials using industrial scale ultrasonic setup.

5.4.2.1 Experimental results and computer simulation

In the semi-horizontal feeding billet, due to the inhomogeneous melt introduction caused by four inlets and potential implications for the macrosegregation and microstructure, the chemical composition and grain size were measured along three directions (at 45° angle from each other), The segregation patterns and distribution of grain size were found to be similar, which attests for the negligible effect of this feeding scheme on the cylindrical symmetry of the segregation and microstructure. So in this chapter, we only present the composition measurements and grain structure along one diameter.
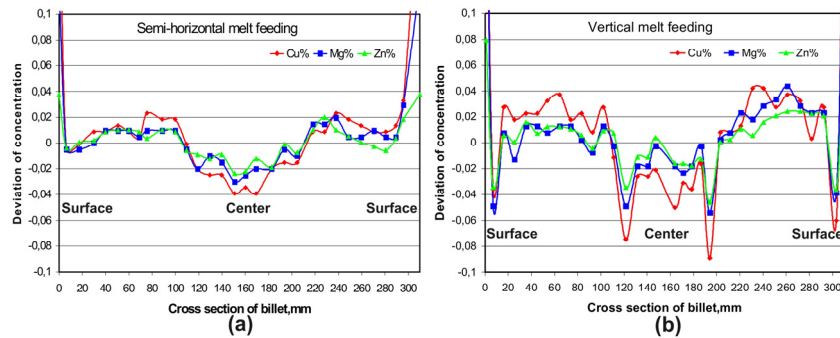

Figure 5.12 Relative deviation of alloying element concentration across billets diameter: (a) semi-horizontal melt feeding billet; and (b) vertical melt feeding billet.

The relative deviation of Cu, Mg and Zn concentrations from the average composition across the billet diameter are shown in Fig. 5.12 (a). A negative central segregation for these elements can be observed. In the vertical feeding billet, as shown in Fig. 5.12 (b), the maximum negative segregation for Cu, Mg and Zn appears 40-50 mm away from the center. The extent of maximum segregation is also getting larger, although the negative centerline segregation was suppressed to some extent as compared with the semi-horizontal feeding billet. The Cu maximum negative deviation almost reached 10 rel.%. At the chilled surface, a strong positive segregation can be observed in both semi-horizontal and vertical feeding billets. We can also see that the extent of deviation of alloying elements in both melt feeding schemes closely follows the magnitude of the partition coefficient. Such as partition coefficient for Cu is 0.17, which is far away from 1, resulted in a stronger segregation as compared with Mg and Zn, which partition coefficients are 0.43 and 0.45, respectively.

95

The grain size variation across the billet diameter is shown in Fig. 5.13. In the semi-horizontal feeding billet, the grains were coarser towards the center, while the minimum grain size was observed near the surface. The distribution of grain size in the vertical melt feeding billet was totally different as compared to that obtained upon semi-horizontal feeding. The minimum grain size was found in the center of billets. In addition, in the vertical melt feeding billet, a layer of coarser grains was found around 40 mm away from the center, as illustrated in Fig. 5.14. The thickness of that layer was approximately 1 mm. The exact positions are shown in Fig. 5.13 with dashed lines. It should be mentioned that the presence of coarse grains near the center was not taken into account during measurement of grain size in Fig. 5.13 because this layer is too thin as compared with the whole billet diameter.
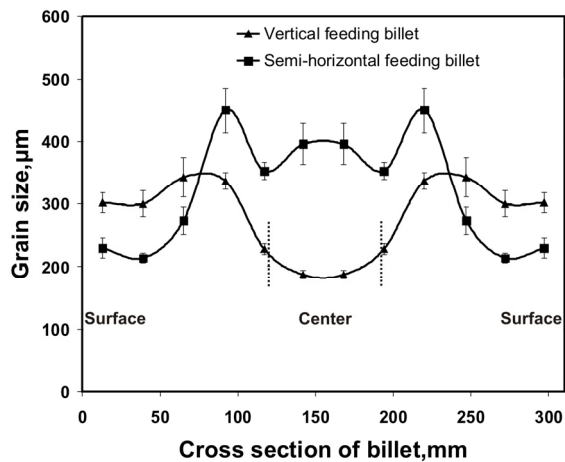
Figure 5.13 Grain size across billets diameter in the semi-horizontal melt feeding billet and the vertical melt feeding billet.
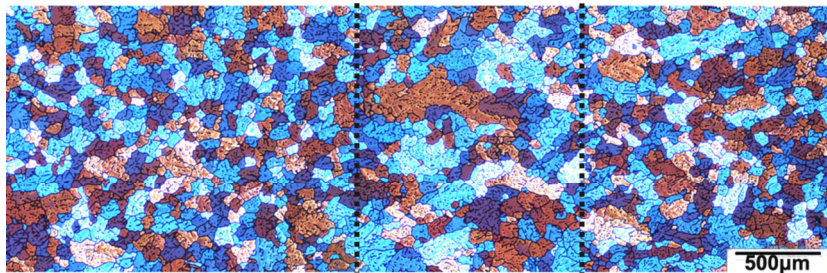
Figure 5.14 A typical layer of coarse grains near the center (40 mm away from the center) found in the billet with the vertical melt feeding. Coarse grains layer is shown in the dashed line area. Note that the length of Fig. 5.14 is only about 4 mm.

Sump profiles and flow patterns in the billet were simulated for both melt feeding schemes, as shown in Fig. 5.15. In the billet cast with semi-horizontal feeding (Fig. 5.15 (a)), the

slope of solidification front is relative gentle. The sump depth in the center (from the melt level in the mold to the solidus) is about 12 cm. The movement of solid and liquid phases (velocity) in the liquid and in the transition region is most intense near the surface, while a moderate upstream flow can be observed in the center. In the billet cast with vertical feeding, vertical melt flow inlet in the center causes a cliff-shaped sump, as shown in Fig. 5.15 (b). The slope increases dramatically at the position 40 mm away from the center. The solidification front drops vertically and the solidification rate at this point is almost zero. The sump depth in the center is about 17 cm. The flow is more pronounced and directed downwards in the center and upwards off-center instead of being intense near the surface as in the case of semi-horizontal feeding.
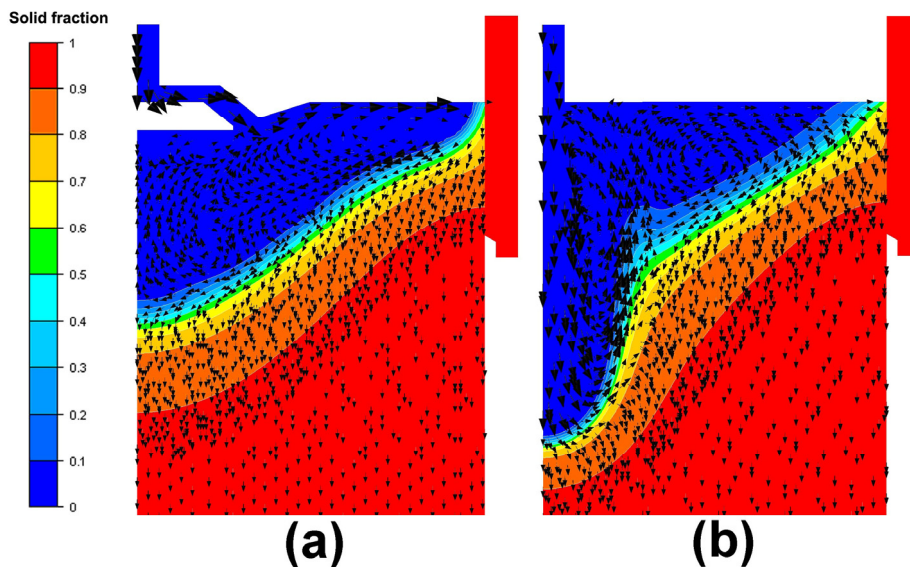

Figure 5.15 Simulated sump profiles and flow patterns during DC casting: (a) semi-horizontal melt feeding billet, maximal magnitude of velocity around melt inlet area is 2.4 mm/s; (b) vertical melt feeding billet, maximal magnitude of velocity around melt inlet area is 30 mm/s. Centerline is on the left.

Fig. 5.16 (a) gives the computer-simulated magnitude of melt flow velocity in the slurry zone in both semi-horizontal and vertical feeding billet. The solid fraction at coherency is taken as 0.5 for our alloy, because both billets in this research are grain refining [20]. The flow velocity in the slurry zone shown in Fig. 5.16 (a) is taken around the 0.4 solid fraction iso-contour. The distribution of vertical distances between liquidus (628˚C) and solidus (472˚C) along the billet radius is also shown in Fig. 5.16 (b). Taking casting speed and the thickness of the transition region into consideration, we can directly estimate the cooling rate during solidification along the billet radius, as shown in Fig. 5.16 (c). In semi-horizontal feeding billet, the maximum cooling rate is achieved at approximately 20 mm from the billet surface. The cooling rate then generally decreases from the surface towards the center. In the vertical feeding billet, the cooling rate rapidly increases near the center after a continuous decrease from the surface.
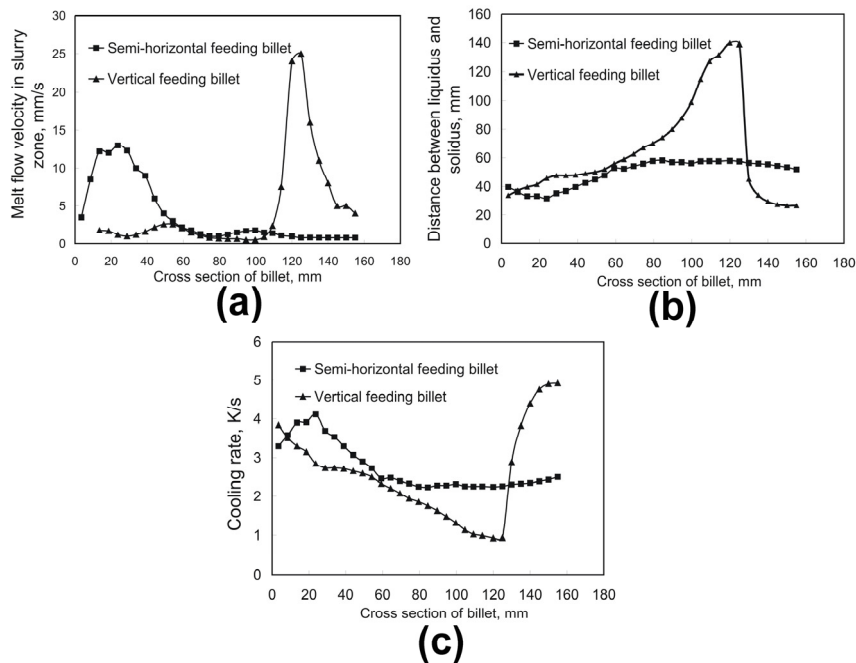
Figure 5.16 Computer-simulated parameters in transition region in both billets with different feeding: (a) the magnitude of melt flow velocity in the slurry zone; (b) the distance between liquidus and solidus along the vertical direction; and (c) estimated cooling rate determined using casting speed and the distance between liquidus and solidus. The abscise goes form surface (0 mm) to center (160 mm).

5.4.2.2 The evolution of grain structure in transition region

The distribution of structure parameters in the horizontal section of a DC casting billet (along the radius or diameter) is of great importance since it determines the homogeneity of technological properties during downstream processing. As mentioned in Chapter 1, the grain size, on one hand, depends on the cooling rate during solidification, on the other hand, strongly depends on the amount of nucleation sites, which can be increased by multiplication of solidification sites by fragmentation through intense forced convection. The transport of nucleating particles, e.g. TiB_2, can be yet another factor in the degree of grain refinement influenced by the melt flow. It is well known that only small fraction of these particles is realized as nucleation substrates [21] so we expect that the effect of the overall melt flow on their distribution will be subtle.

Although the detailed information of fragmentation effect can not be directly obtained from computer simulation, the magnitude of melt flow velocity in the slurry zone is known to be related to this effect. Thus, in this research, we use this parameter to represent the fragmentation effect of growing dendrites during DC casting.

98

Looking at the magnitude of melt flow velocity in Fig. 5.16 (a) and cooling rate in Fig. 5.16 (c), we can find the grain size is clearly determined by a combination of movement/fragmentation effect and cooling rate. In semi-horizontal feeding billet, as shown in Fig. 5.16 (a), the peak of flow velocity in the slurry zone represents stronger fragmentation effect close to the surface (around 20 mm away from the surface). When we look back in Fig. 5.13, we can find that due to this strong fragmentation effect, the grain size decreases near this area, but with 20 mm shift along the flow direction (around 40 mm away from the surface). This can be explained by the movement and settling of substrates created by fragmentation along the flow in the slurry zone. Similarly, in vertical feeding billets, the grain size starts to decrease (from the position 100 mm away from the surface, as shown in Fig. 5.13) when the fragmentation effect is getting stronger, as shown in Fig. 5.16 (a). The transport of fragments is weakened in this case due to the vertical solidification front. Although the flow velocity in the center is relative weak, the cooling rate in the center is quite high. This is why small grain size can be still obtained in the center.

5.4.2.3 The relative movement of solid and liquid phase in slurry zone

It is well known that the convection flow in the liquid and slurry zone results in the redistribution of alloying elements in the DC casting billet. As shown in Fig. 5.15(a) and Fig. 5.16 (a), in semi-horizontal feeding billet the penetration of melt flow into the slurry zone is more pronounced near the surface area. This means that the effect of washing out of solute-rich liquid from the slurry zone in this area is larger than in the quarter and center of the billet. This solute-rich liquid moves then towards the quarter and central areas along with the convection flow, which results in the lack of alloying elements near the surface area and the positive segregation in the quarter position.

In the vertical feeding billet, the flow pattern changed totally because of different melt inlet (Fig. 5.15 (b)). There are two convection flows as illustrated in Fig. 5.15 (b). One is near the center area, counter-clockwise. Another is at the quarter and surface of the billet, in the clockwise direction. Two flows collide at the position 40-50 mm away from the center. As we can see from Fig. 5.16 (a), the most pronounced washing out of solute-enrich liquid from the slurry zone happens around the cliff-shaped solidification front (40 mm away from the center). This strong upstream flow in the slurry zone might wash out the enriched solute either to the center or to the surface area, which causes negative segregation in this area, as shown in Fig. 5.12 (b). It should be mentioned here that it has been reported that strong forced unidirectional flow in the center may cause a consistent change of the concentration along the billet axis, which can be detected in the last stages of casting [13]. However, in this research, we only selected one slice for each billet in the middle of steady state casting and did not take this effect into account.

The movement of solid grains along with convection flow is also one of the mechanisms of macrosegregation. The 'floating' grains, which form at an earlier stage of solidification, are usually depleted of the main alloying elements in Al alloys such as Cu, Mg, Zn. These grains float with convection flow and usually settle in the center of DC casting billet, causing centerline negative segregation [22]. These grains typically demonstrate coarse dendrite arms reflecting their longer individual solidification time.

In this research, we could not find any typical 'floating' grains in both the semi-horizontal and vertical billets. However, the layer of coarse grains found in the vertical melt feeding billet, as shown in Fig. 5.14, might be related to off-center negative segregation (40 mm away from the center) in Fig. 5.2 (b) if we interpret this phenomenon as follows.
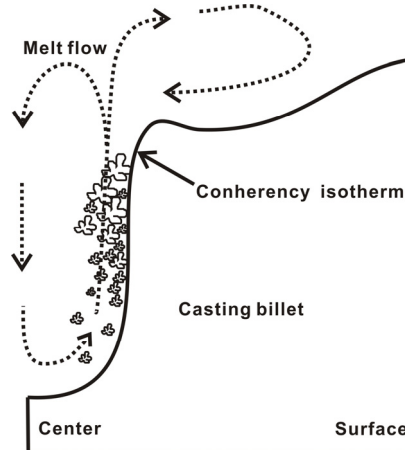

Figure 5.17 Schematic view of relative movement of melt and grains along cliff-shaped sump in vertical melt feeding billet.

Figure 5.17 is the schematic view of cliff-shaped sump in the vertical melt feeding billet. A cliff-shaped sump leads to an almost vertical solidification front approximately 40 mm away from the center. The grains, which are formed in the slurry zone around this vertical solidification front or formed earlier at other position then arrived in this area with melt flow, will stack and grow at the same position of almost vertical solidification front because of strong upstream melt flow and gravity. The low cooling and solidification rates in this region (Fig. 5.16 (c)) further promote the formation of these coarse grains.

It is also worth to notice that in Fig. 5.15 (b), there is a collision area of clockwise and counter-clockwise flows. In this area there is almost no horizontal velocity component. In this case, solid grains cannot be displaced from that cliff-shaped front due to stack of grains, but solute enriched melt can. As a result, the strong upstream flow will continue to take the solute enriched liquid away from this slurry zone but leave the solute depleted grains. This might enhance negative segregation in this cliff shaped sump area (40 mm away from the center).

5.4.2.4 Solidification shrinkage-driven flow in mushy zone

As an important mechanism of macrosegregation, the solidification shrinkage-driven flow in the mushy zone usually determines the inverse (negative) centerline segregation in DC casting billets of aluminum alloys. This shrinkage flow is caused by the pressure difference over the solidifying layer of the mushy zone, which results in the movement of the solute-rich liquid to the deeper part of mushy zone in the direction perpendicular to the solidification front.

A simple analytical model was suggested by Du and Eskin in order to analyze the effect of the mushy zone geometry on the degree of shrinkage-induced macrosegregation in DC casting of aluminum alloys [23]. In this research, we used this model to make a simple analysis for segregation of Cu (Mg and Zn follow the same trend) and the effect of melt inlet on shrinkage-induced macrosegregation.

The main idea of this model is that the centerline negative segregation is caused by the horizontal component of the shrinkage-driven flow from the center to the surface of the billet. By taking solidification shrinkage and solidification front inclination into account, the total amount of the transferred solute at different positions during the solidification period (L_m/V_{cast}) is as follows [23]

$$L_h = \int_0^{L_M/V_{cast}} C_l f_l V_{cast} \beta (\sin 2\alpha)/2 dt \, , \qquad (5.1)$$

Where V_{cast} is the casting speed; β is shrinkage ratio (0.1 for an aluminum alloy); α is the local slope of the coherency isotherm; L_m is the vertical thickness of the mushy zone; C_l is liquid phase concentration; and f_l is the volume fraction of liquid phase. This equation can be reduced for Cu (partition coefficient K_{Cu} is taken as 0.171) [23] as

$$L_h = 0.78 C_0 L_M \beta (\sin 2\alpha)/2 \, , \qquad (5.2)$$

The derivative of Eq. (5.2) dL_h/dr (r is the radial distance from the billet center) is the net efflux and is a measure of the macrosegregation caused by solidification shrinkage. The detail derivation of these equations can be found in Ref [23].

Fig. 5.18 (a) is the distribution of transferred solute L_h from the center to the periphery of the semi-horizontal feeding billet. This curve represents the balance between the amount of solute coming to one point and the amount of the solute coming out of this point. When the slope is positive, the in-coming solute is less than out-coming solute, which causes negative segregation at this position by shrinkage driven flow. On the contrary, the negative slope results in positive solute income at this position. Fig. 5.18 (b) is the relative segregation of Cu ($-(dL_h/dr)/C_{cu}$), obtained by the derivative of the polynomial fit shown in Fig. 5.18 (a) with respect to radial distance from the center of semi-horizontal billet (with the negative sign). It is clearly shown that shrinkage driven flow causes a negative segregation in the center of the billet until the position 60 mm away from the center, then a positive segregation occurs. Near the surface of the billet, the segregation changes to negative again.

If we compare the calculated shrinkage-induced segregation in Fig. 5.18 (b) with real Cu segregation distribution in the semi-horizontal feeding billet (Fig. 5.12 (a)), a good agreement on the distribution of Cu segregation can be found. It should be noted that the segregation curve in Fig. 5.18 (b) reflects only the calculated segregation caused by shrinkage-driven flow. As discussed before, the movement of solute-enrich liquid in the slurry zone from the surface to the center contributed to a centerline positive segregation. Taking into this account, negative 6.5 rel.% deviation of Cu in the center caused by the shrinkage flow (Fig. 5.18 (b)) might be compensated by the effect of convection flow in the

101

slurry zone. As a result, the negative centerline segregation in the real casting billet reduces to about 4 rel.%, as shown in Fig. 5.12(a).
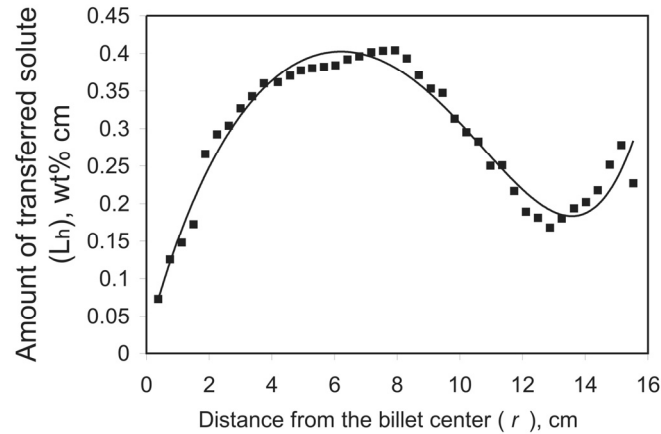
(a)
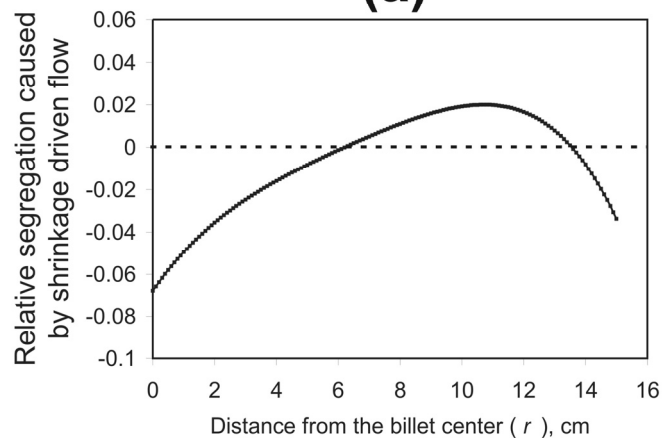
(b)

Figure 5.18 Effect of shrinkage driven flow on macrosegregation in the semi-horizontal melt feeding billet: (a) amount of transferred solute from the center to the surface and its polynomial fit; and (b) relative segregation caused by shrinkage driven flow, obtained by the derivative of the polynomial fit.

Same analysis has also been done for the vertical melt feeding billet. Fig. 5.19 (a) shows the distribution of transferred solute L_h from the center to the periphery. Due to relatively complex distribution of L_h, we divided the distribution in Fig. 5.19 (a) into two parts and made the polynomial fits separately in order to obtain better fitting accuracy. By the derivative of L_h distribution in Fig. 5.19 (a), we obtain the relative Cu segregation from the center to the surface of the vertical feeding billet, as shown in Fig. 5.19 (b). The agreement

between shrinkage-induced segregation in Fig. 5.19 (b) and real segregation distribution in Fig. 5.12 (b) is not as good as in semi-horizontal feeding billet. But we still can see that there is an obvious negative segregation at the position 40-50 mm away from the center, which shows the shrinkage driven flow might also contribute to the strong off-center negative segregation in addition with the convention flow and "floating" grains as discussed above.
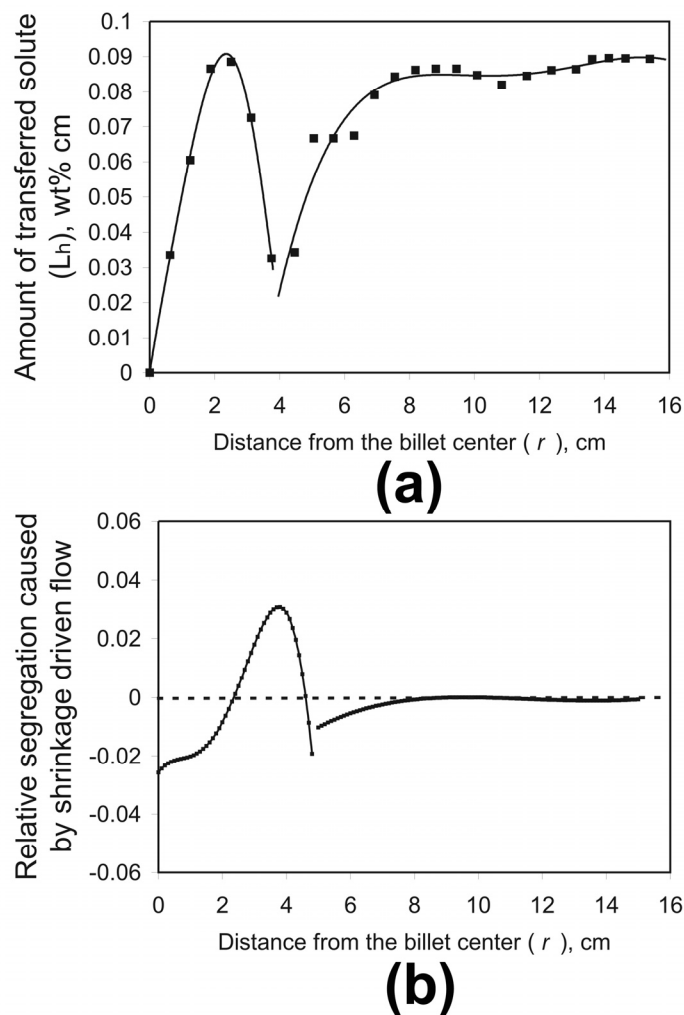

(a)

(b)

Figure 5.19 Effect of shrinkage driven flow on macrosegregation in vertical melt feeding billet: (a) amount of transferred solute from the center to the surface and its polynomial fits; and (b) relative segregation caused by shrinkage driven flow, obtained by the derivative of the polynomial fit.

The shrinkage driven flow also causes a positive segregation at the position 25-40 mm away from the center, as shown in Fig. 5.19 (b). Although the positive segregation in this area does not appear in real segregation curve in Fig. 5.12 (b) (only a slight increase in the concentration can be observed), it becomes logical when the melt flow in slurry zone is also considered. This positive segregation area caused by shrinkage driven flow coincides with the position where a strong upstream flow is. Therefore the liquid near the coherency isotherm could be already depleted by this upstream flow and might not be rich enough to allow the shrinkage driven flow to create such a positive segregation. In addition, the redistribution of solute to the surface area in combination with a flat region of almost no shrinkage-induced segregation (from quarter to the surface of the billet), leads to a positive segregation in this region, as shown in Fig. 5.12 (b).

As for the strong positive segregation at chilled billet surface we observed in both billets, similar results have been reported elsewhere [2, 4, 22]. It is a result of shrinkage driven flow toward to the chilled surface, where there is no out-coming flow. Thus, the solutes will accumulate at the chilled surface and usually lead to a negative segregation in the sub-surface region, as shown near the surface area in Fig. 5.12 (a) and (b).

The results presented in this section show in exaggerated form the possible effects of ultrasound-induced flows on the structure and macrosegregation formation. Together with the results shown in the previous sections, these data demonstrate that the flows induced by ultrasound (or other means of forced convection can dramatically change the grain size and composition distribution in the billet cross section.

5.5 Conclusions

The results presented in this chapter clearly show a promising application prospect of UST in DC casting. Although the UST in the launder using the baffles design did not result in the same degree of grain refinement as in small-scale experiments, the positive effect of baffles design in the launder on ultrasonic-aided grain refinement was revealed. Water modeling facilitated the choice of baffle design.

The application of UST in the hot top did not only benefit grain structures, but also influenced the distribution of alloy elements in DC casting billet. However, the limitation of our laboratory scale ultrasonic setup restricted upscaling of the effects, since it could not provide enough powerful streaming as would be required in large scale DC casting. Therefore, an extended analysis was performed using different melt feeding schemes in real industrial DC casting billets in order to simulate the application of powerful UST at different positions in the liquid pool during DC casting. The experimental and computer simulation results showed that the modification of flow patterns and the geometry of the sump caused by different melt feeding scheme resulted in significant changes in the distribution of grain structures and macrosegregation across the billet diameter. This research provides us very useful information that if the UST can be powerful enough and placed in proper positions of liquid pool during DC casting, the flow patterns in the liquid and slurry zone, even the geometry of the sump can be optimized in the way suitable for control of macrosegregation and structure. In this case, both grain refinement effect and uniform distribution of alloying elements in the billets can be achieved through ultrasonic processing in DC casting. The further attempts to modification flow patterns and sump in

real DC casting trials using UST in the liquid pool is suggested to be a very interesting industrial subject worth of investigating.

References:

[1] D.G.Eskin, *Physical Metallurgy of Direct Chill Casting of Aluminum Alloys*. 2008, New York: CRC Press.

[2] D.G.Eskin, Jr.J.Zuidema, V.I.Savran, and L.Katgerman, *Mater. Sci. Eng. A*, 2004. **384A**: p. 232-244.

[3] D.G.Eskin, V.I.Savran, and L.Katgerman, *Metall. Mater. Trans. A*, 2005. **36A**: p. 1965-1976.

[4] R.Nadella, D.G.Eskin, and L.Katgerman, *Metall. Mater. Trans. A*, 2008. **39A**: p. 450-461.

[5] L.Zhang, D.G.Eskin, A.Miroux, T.Subroto, and L.Katgerman, *Metall. Mater. Trans. B, DOI:10.1007/s11663-012-9711-x*, 2012.

[6] R.C.Dorward and D.J.Beerntsen, *Light Metals 1990*, C.M.Bickert, Editor. 1990, TMS: Warrendale,PA. p. 919-924.

[7] V.A.Livanov, R.M.Gabidullin, and V.S.Shepilov, *DC Casting of Aluminium Alloys*. 1977, Moscow: Metallurgiya.

[8] G.I.Eskin, *Ultrasonic Treatment of Light Alloy Melts*. 1998, Amsterdam: Gordon and Breach Science Publishers.

[9] Z.H.Li, X.X.Li, M.Zhang, and X.H.Xu, *The Chinese J. Nonferrous Metals*, 2011. **21**(2): p. 318-424.

[10] G.I.Eskin, *Ultrason. Sonochem.*, 2001. **8**: p. 319-325.

[11] http://www.substech.com/dokuwiki/doku.php?id=direct_chill_dc_casting.

[12] T.V.Atamanenko, *Cavitation-aided Grain Refinement in Aluminum Alloys* 2010, Delft University of Technology: Delft.

[13] D.G.Eskin, A.Jafari, and L.Katgerman, *Mater. Sci. Tech.*, 2011. **27**: p. 890-896.

[14] D.G.Eskin, A.N.Turchin, and L.Katgerman, *Int. J. Cast Metals Res.*, 2009. **22**: p. 99-102.

[15] D.Mortensen, *Metall. Mater. Trans. B*, 1999. **30B**: p. 119-133.

[16] D.Mortensen, H.G.Fjær, D.Lindholm, M.Rudshaug, and E.A.Sørheim, *Mater. Sci. Forum*, 2011. **693**: p. 187-195.

[17] M.Lalpoor, D.G.Eskin, D.Ruvalcaba, H.G.Fjær, A.TenCate, N.Ontijt, and L.Katgerman, *Mater. Sci. Eng. A*, 2011. **528**: p. 2831-2842.

[18] O.Ludwig, J.M.Drezet, C.L.Martin, and M.Suery, *Metall.Mater.Trans.A*, 2005. **36A**: p. 1525-1535.

[19] M.Lalpoor, *Study of Cold Cracking during DC-casting of High Strength Aluminum Alloys*. 2010, Delft University of Technology: Delft.

[20] L.Arnberg, L.Bäckerud, and G.Chai, *Dendrite Coherency, in: Solidification Characteristics of Aluminum Alloys, vol. 3*. 1996, Des Plaines, IL: American Foundrymen's Society.

[21] A.L.Greer, P.S.Cooper, M.W.Meredith, W.Schneider, P.Schumacher, J.A.Spittle, and A.Tronche, *Adv. Eng. Mater.*, 2003. **5**(1-2): p. 81-91.

[22] D.G.Eskin, R.Nadella, and L.Katgerman, *Acta Mater.*, 2008. **56**: p. 1358-1365.

[23] D.G.Eskin, Q.Du, and L.Katgerman, *Scripta Metall.*, 2006. **55**: p. 715-718.

Chapter 6

Effect of ultrasonic processing on thermal contraction during and after solidification

6.1 Introduction

The contraction of aluminum alloys during and after solidification has a decisive effect on the quality of casting products (see Chapter 1). The formation of cracks, which is considered as an irreversible failure in aluminum alloys casting, depends to a great extent on the contraction behavior during and after solidification.

The initiation of hot tearing usually is a result of the inadequate feeding compensation of the shrinkage and thermal stresses caused by uneven thermal contraction duo to temperature gradients in the solidifying casting [1, 2]. As for the cold cracks, the accumulation and concentration of residual stresses in the casting during cooling after the end of solidification under conditions of high temperature gradients and low ductility is given as a main reason for the brittle failure [3]. The solidification shrinkage above the solidus and thermal contraction above and below the solidus, are the constitutive mechanisms that govern the formation of stresses and eventually the cracking of the casting. Therefore, the understanding of the contraction behavior is of the essence for the analysis of stress–strain development and modeling of hot tearing and cold cracks.

Generally, contraction behavior in aluminum alloys is affected by microstructure [4], composition [5-7], as well as melt quality [4, 8]. In previous chapters, the focus was mainly on the modification of grain structures caused by ultrasonic processing. It was observed that UST results in the refinement of grain structure, which may have a direct influence on the contraction behavior. In addition, other beneficial effects provided by ultrasonic processing might also play a role on the contraction behavior in Al alloys. However, although all these effects, as introduced in Chapter 1, have been reported in various sources, their potential influence or the effect of ultrasonic processing itself on the contraction behavior during solidification was rarely addressed.

The results presented in this chapter constitute a first step to a throughout understanding of the contraction behavior in aluminum alloys under UST. The first part of this chapter presents a study on contraction behavior under ultrasonic processing during solidification, such as the temperature of contraction onset and linear thermal contraction during solidification in different Al alloys or under different UST temperatures. Then several factors affecting thermal contraction at different temperature ranges after solidification are analyzed. The research in this chapter is a key step to the further analysis of how UST may affect the cracking susceptibility, as well as the properties of casting products.

6.2 Experimental procedure

In order to analyze the contraction behavior of metals, a special technique was developed to measure the linear contraction at temperatures above and below solidus [7]. It is based on the idea suggested by Novikov [5]. The experimental set-up comprises the following parts: a T-shape graphite mold with one moving wall, a water-cooled bronze base which provides high cooling rate during solidification (5-10 K/s) that is similar to the conditions in DC casting, a linear displacement sensor (linear variable differential transformer (LVDT)), a K-thermocouple, and a computer-based data acquisition system.

Fig. 6.1 and Fig. 6.2 show a picture and the schematic view of the experimental setup used in this research, respectively. The cross-section of the main cavity is 25 mm×25 mm with a gage length of 100 mm. The cross-section of the T-shape cavity is thinner than that of the main cavity, which allows the melt to solidify faster at the T-shape end. The solidifying sample is therefore fixed on this side. On the opposite side, a metallic rod is attached to the moving wall to create a rigid connection between the solidifying metal and the moving wall. The position of the moving wall is detected by the LVDT, which is accurate to 6 μm m or 0.006% of the gage length. The temperature is monitored with a 0.1-mm thin, open tip K-thermocouple standing vertically in the center of the mold at about 1.5 mm above the mold bottom to avoid the problem of filling the gap between the thermocouple tip and the mold bottom. During the experiments, the temperature in the main cavity and displacement of moving wall are recorded simultaneously by the data acquisition system.
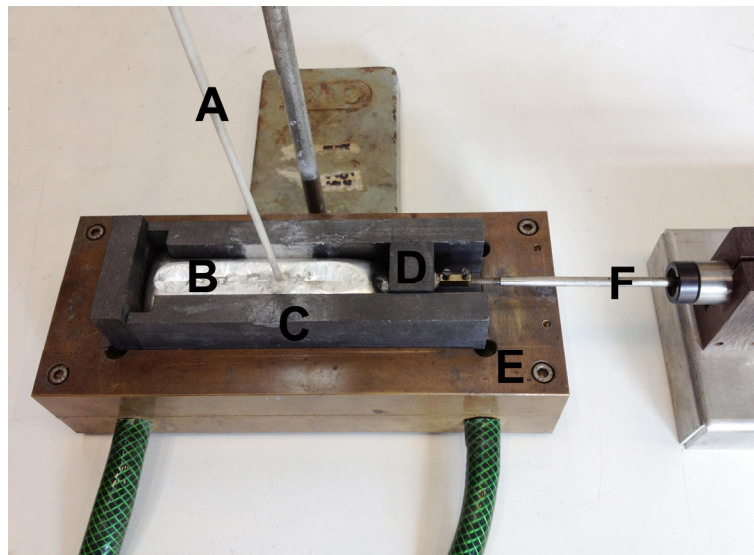

Figure 6.1 Experimental setup for contraction measurement. A, thermocouple; B, solidifying aluminum alloy; C, graphite mold with T-shaped end; D, moving wall; E, water-cooled bronze base; F, linear variable differential transformer.

Based on previous experience in our group [7], a refractory paint (bone ash) was applied onto the internal walls in the central part of the mold, as shown in Fig. 6.2, in order to equalize cooling rates, reduce temperature gradient, and assure that the first contact between opposite coherent parts of the sample occurs in the area where the temperature is measured.

An Al-4 wt% Cu alloy was selected in these experiments because of the well known phase diagram, and structural and thermal-physical features [9, 10]. During experiment, the alloy (appr. 0.2 kg melt) was firstly molten in an electric furnace, and then treated by ultrasonic processing (4 kW) for about 10 s directly in the crucible. The detail of ultrasonic processing was introduced in Chapter 2. The tip of the sonotrode was preheated by dipping it in a large

volume of molten Al prior to the experiment. After ultrasonic treatment, the melt was poured into the main cavity next to thermocouple up to the certain level (12 mm height). Without ultrasonic treatment, the melt was poured into the mold directly when the temperature reached to 710 ˚C after taken out from the furnace. Microstructure and composition analysis were made on the cross section taken from the middle of the samples near the thermocouple. Two or three samples were prepared for each condition to verify the repeatability.

After the test, the temperature was plotted versus time in order to derive the cooling curves from which the cooling rate and characteristic temperatures in the solidification range were obtained. After this, the data were reconstructed to observe the direct dependence of displacement on temperature.
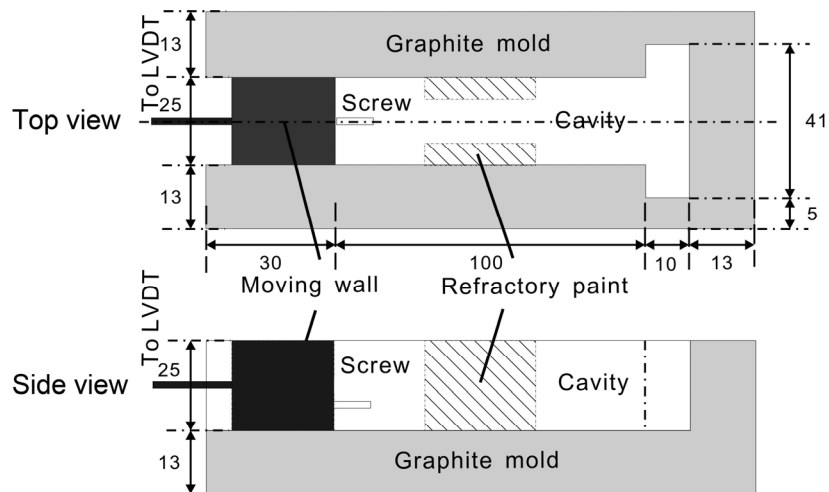

Figure 6.2 Schematic view of the contraction experimental setup. Dimensions are given in millimeters.
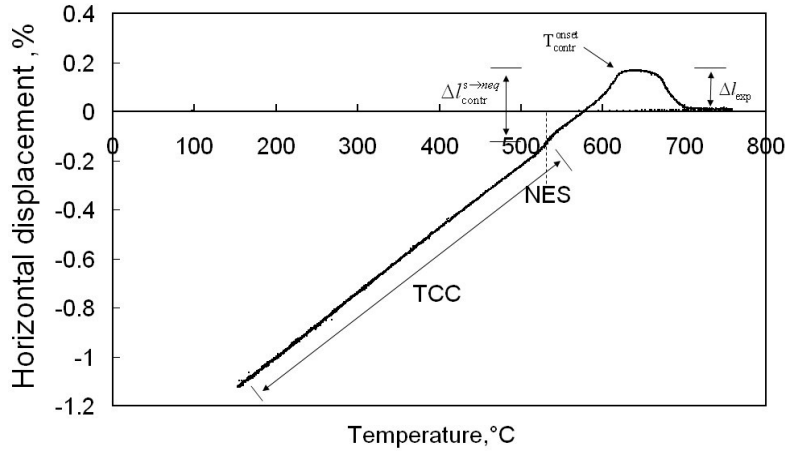
Figure 6.3 Examples of data obtained from contraction experiments. $\Delta l_{\exp}$ is the pre-shrinkage expansion; T_{contr}^{onset} is the temperature of the contraction onset; $\Delta l_{contr}^{s \to neq}$ is the amount of contraction in the non-equilibrium solidification range, and TCC indicates the range where the linear thermal contraction coefficient can be calculated.

Figure 6.3 shows an example of the contraction curve for an Al alloy. From this curve, the temperature of the contraction onset T_{contr}^{onset}, the pre-shrinkage expansion $\Delta l_{\exp}$, the amount of contraction in the non-equilibrium solidification (NES) range $\Delta l_{contr}^{s \to neq}$ and the thermal contraction coefficient (TCC) at sub-solidus temperature can be extracted directly.

The pre-shrinkage expansion is calculated in the temperature range between the temperature of expansion onset and the temperature of contraction onset.

The linear thermal contraction during solidification (the amount of contraction in the solidification range) is determined as follows [5, 7]:

$$\varepsilon_s = \frac{l_s + \Delta l_{\exp} - l_f}{l_s}, \qquad (6.1)$$

Where l_s is the initial length of the cavity (100 mm); l_f is the length of the sample at the non-equilibrium (NEQ) temperature of solidus. It is worth to note that at the used cooling rates (5-10 K/s), the solidification range was considered as NEQ, hence the solidification ended at the (non-equilibrium) eutectic temperature.

The average TCC between two temperatures T_2 and T_1 ($T_2 > T_1$) below the solidus is calculated as follows:

111

$$TCC = \frac{l_{T_2} - l_{T_1}}{l_{gage}(T_2 - T_1)}, \qquad (6.2)$$

Where l_{T_2} and l_{T_1} are the positions of the displacement sensor at T_2 and T_1, respectively; and l_{gage} is the gage length of the sample.

6.3 The contraction behavior under UST during solidification

6.3.1 Effect of transition metals Zr and Ti

The addition of transition metals Zr and Ti has shown a promising grain refining effect under UST (see Chapter 2 and Chapter 4). In this part of the study, we continue to use these additions in order to reveal how ultrasonic processing and transition metals Zr and Ti affect the thermal contraction in aluminum alloys.

Four alloys were selected for this experiment: Al-4 wt% Cu, Al-4 wt% Cu-0.2 wt% Zr, Al-4 wt% Cu-0.2 wt% Zr-0.03 wt% Ti and Al-4 wt% Cu-0.2 wt% Zr-0.06 wt% Ti. The melt (appr. 0.2 kg), when still in the crucible, was subjected to UST (4 kW) at 710 ˚C for 10 s, and then immediately poured into the main cavity. Sample without UST were produced by casting at 710 ˚C.

The temperature of non-equilibrium solidus for the Al-4 wt% Cu alloy is about 548 ˚C, as observed from the cooling curves and agrees well with literature data [9, 10] and Thermocalc calculation. The effect of small amount of Zr and Ti used in this study on NES was considered to be negligible, as observed from the cooling curves and calculated from Thermocalc.

The results show that the pre-shrinkage expansion was unaffected by both transition metals and ultrasonic processing in these experiments. This level is different from the ones previously measured with an AA7075 alloy. In that research on AA7075 [4], a relatively large pre-shrinkage expansion (0.1-0.4 %) was found. Usually, the pre-shrinkage expansion is believed to be related to the evolution of gases (mainly hydrogen) at the onset of solidification and upon further solidification until the rigid solid skeleton is formed. There are two factors that may explain the different behavior of two alloys. On one hand, the hydrogen liquid solubility in the Al-4 wt% Cu alloy used in these experiments and in the AA7075 alloy used in previous experiments is different, being larger in the latter [11]. As a consequence, the different initial volume of hydrogen in the melt was directly reflected in different amount of pre-shrinkage expansion. In addition, the sample height was reduced from 25 mm in previous experiments to 12 mm in these experiments in order to reduce the inhomogeneity of the solidifying sample. As a result, the time for the evolution of gases in the 12 mm height sample became shorter, which additionally decreased the degree of expansion.

After the expansion, when the rigidity solid skeleton is formed, the sample starts to contract. From this moment, stresses and strains begin to build up, and feeding of the liquid into the mushy zone becomes more and more difficult. These factors directly determine the quality

112

of the castings. Therefore, in this research, we mainly focused on the contraction behavior started from the temperature of the contraction onset.
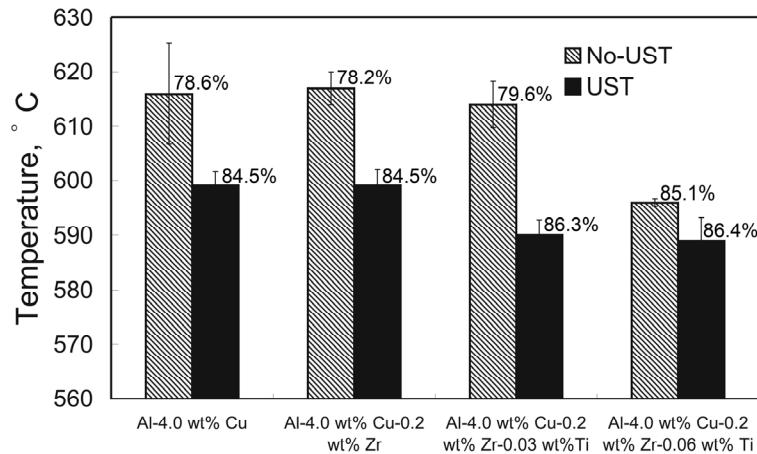

Figure 6.4 The temperature of contraction onset for different experimental alloys with and without ultrasonic processing. Numbers on the top of each column are the solid fraction at contraction onset temperature.

Figure 6.4 summarizes the temperatures of contraction onset for the different experimental alloys with and without ultrasonic processing. The temperature of contraction onset decreases when UST was applied in all alloys. The solid fraction at the onset of contraction for each alloy, which is calculated from Thermocalc, is also shown in Fig. 6.4. When UST was used, the solid fraction at onset of contraction increases in all experimental alloys.

The contraction onset is believed to reflect the formation of a rigid solid skeleton. In our experiments, the thermocouple was standing vertically in the center of the mold at about 1.5 mm above the mold bottom, which means that we measured the contraction onset temperature reflecting the onset of bridging between two opposite walls (in the longitudinal direction) of the mold. At the beginning of the contraction, the solid skeleton might only formed close to the bottom, while the above area was still in the semi-liquid or liquid state, which hardly contributes to the contraction. Since the grain structure is crucial for the formation of rigidity skeleton, the grain structure close to the bottom area will govern the temperature of contraction onset.

Figures 6.5 to 6.8 demonstrate the grain structures in all experimental alloys at the bottom and in middle part of the samples produced without and with UST.
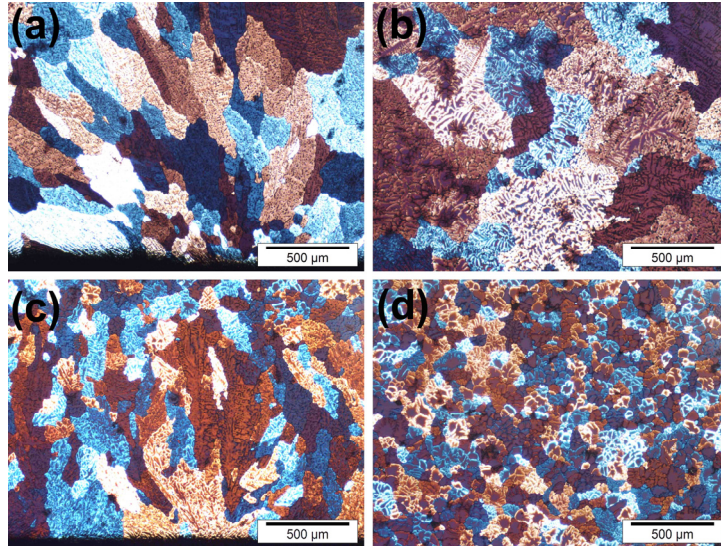
Figure 6.5 The grain structure in the Al-4 wt% Cu alloys: (a) without UST, at the bottom part of the sample; (b) without UST, in the middle part of the sample; (c) with UST, at the bottom part of the sample and (d) with UST, in the middle part of the sample.
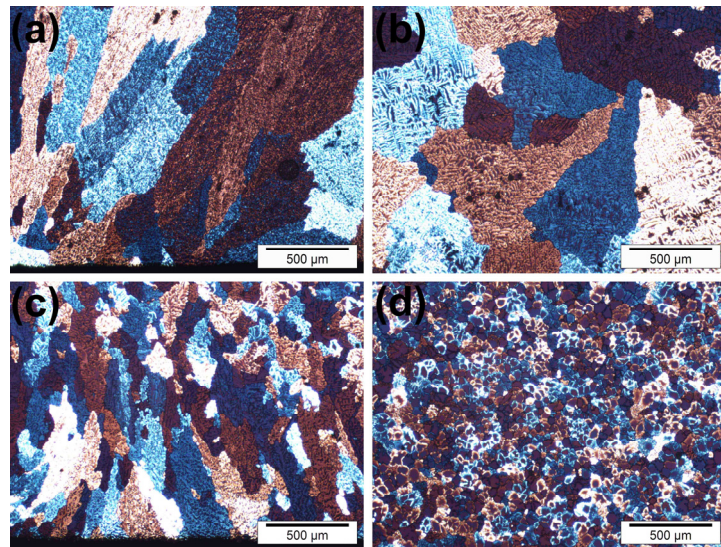

Figure 6.6 The grain structure in the Al-4 wt% Cu-0.2 wt% Zr alloys: (a) without UST, at the bottom part of the sample; (b) without UST, in the middle part of the sample; (c) with UST, at the bottom part of the sample and (d) with UST, in the middle part of the sample.

114

Figure 6.7 The grain structure in the Al-4 wt% Cu-0.2 wt% Zr-0.03 wt% Ti alloys: (a) without UST, at the bottom part of the sample; (b) without UST, in the middle part of the sample; (c) with UST, at the bottom part of the sample and (d) with UST, in the middle part of the sample.

Figure 6.8 The grain structure in the Al-4 wt% Cu-0.2 wt% Zr-0.06 wt% Ti alloys: (a) without UST, at the bottom part of the sample; (b) without UST, in the middle part of the sample; (c) with UST, at the bottom part of the sample and (d) with UST, in the middle part of the sample.
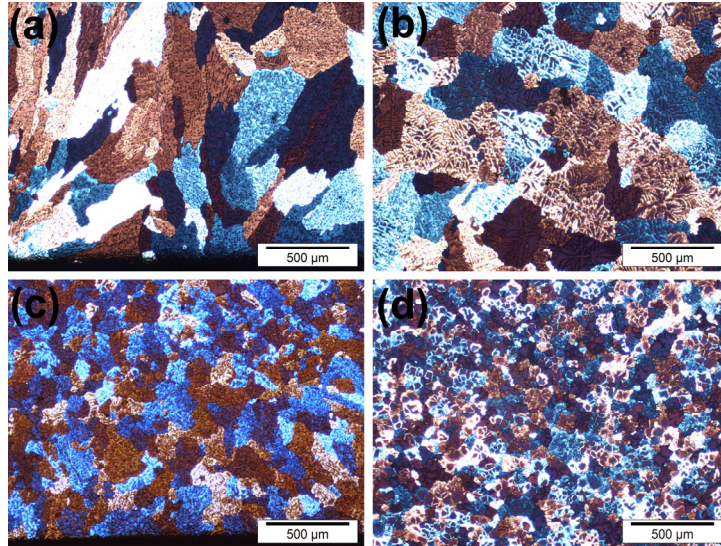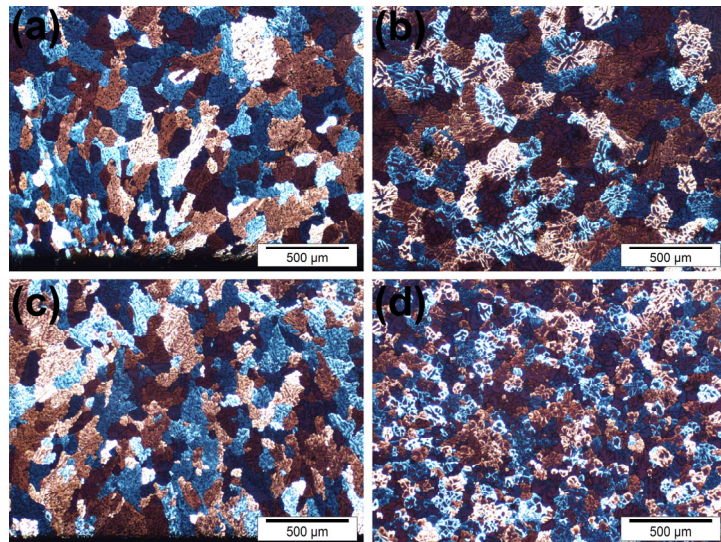
115

In the Al-4 wt% Cu alloy, a large columnar structure is found close to the bottom, as shown in Fig. 6.5 (a). With the help of ultrasonic processing, the columnar structure in Fig. 6.5 (c) was inhibited to some extent, but it is still visible. Similar result can be found in the Al-4 wt% Cu-0.2 wt% Zr alloy, as illustrated in Fig. 6.6 (a) and (c). When 0.03 wt% Ti was added in the Al-4 wt% Cu-0.2 wt% Zr alloy, although similar columnar structure was still found in non-treated alloy (Fig. 6.7 (a)), UST resulted in a nearly equiaxed dendrite structure close to the bottom, as shown in Fig. 6.7 (c). This is in agreement with our previous conclusion in Chapter 2 that small amount of Ti should be added together with Zr in order to obtain a better grain modification effect. With further increasing Ti to 0.06 wt%, the columnar structure became weaker even in the non-treated alloy and disappeared in the ultrasonic treated alloy, as illustrated in Fig. 6.8 (a) and (c).

Taking these structural features close to the bottom into account, we can conclude that higher contraction onset temperature is usually associated to alloys with larger columnar structure close to the bottom. The inhibition of columnar structure or the transformation of columnar structure to equiaxed grains caused by ultrasonic processing results in the reduced temperature of contraction onset. It is suggested that the structure related delay of the formation of rigid solid skeleton [12, 13] near the bottom is the main reason for this temperature decrease.

A schematic view of this effect is shown in Fig. 6.9. After the melt is poured into the mold, it begins to solidify from the two edges (where the sample is fixed) toward the center of the mold. Then at a certain time (as shown in Fig. 6.9), the melt on the bottom layer must reach the solid fraction at rigidity, and form a rigid skeleton (region A in Fig. 6.9). But above this point the rest of the sample is still in the semi-liquid or liquid state (region B in Fig. 6.9).

When a continuous rigid skeleton just forms in the samples with columnar structures close to the bottom, the contraction of the sample can be recorded, as shown in Fig. 6.9 (a). However, the solid fraction at this temperature is not higher enough for the formation of a continuous rigid skeleton in the samples with small equiaxed grains (Fig. 6.9 (b)) because the required solid fraction for coalescence of grains is higher than the samples with columnar structures. Therefore, the temperature of contraction onset is usually lower in the samples with lesser or non-columnar structures. UST facilitates the formation of equiaxed dendrite structure close to the bottom, especially when Zr and Ti are present in the melt, as a result, reduces the contraction onset temperature.
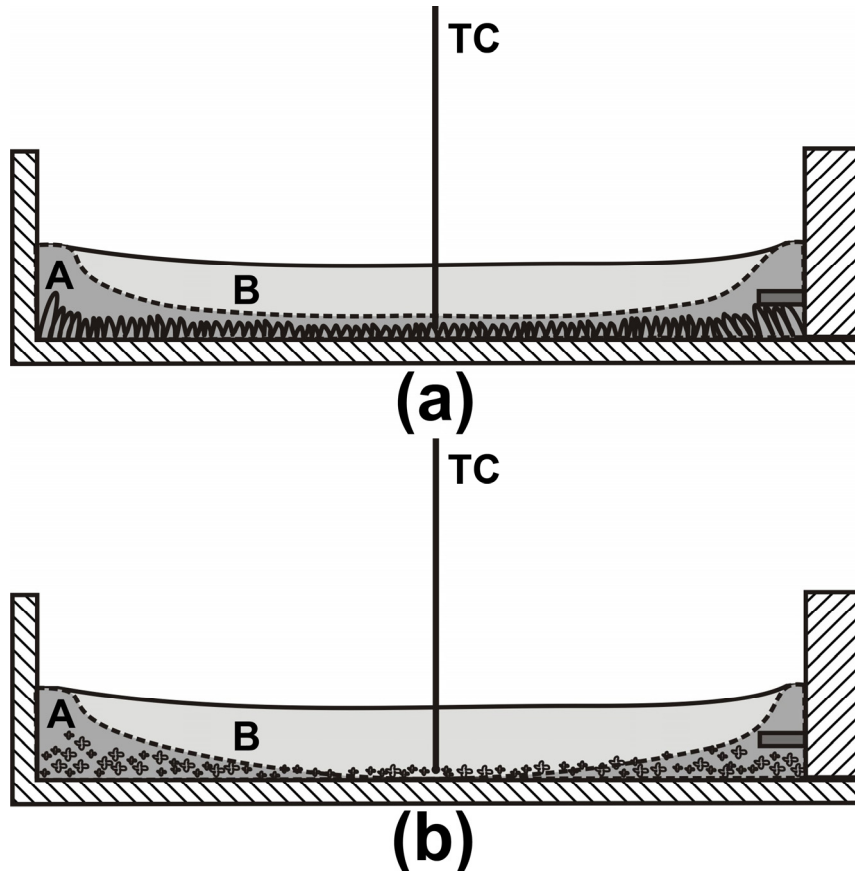
Figure 6.9 A schematic view of solidification progress in the mold (longitudinal direction) near the contraction onset temperature: (a) columnar structures close to the bottom and (b) equiaxed grain structures close to the bottom. A, rigidity skeleton zone; B, semi-liquid/liquid zone; TC, thermocouple.

UST did not only reduce the onset temperature, but also affected the further thermal contraction during solidification, as shown in Fig. 6.10. The linear thermal contraction during solidification decreased when UST was applied. In non-treated Al-4 wt% Cu and Al-4 wt% Cu-0.2 wt% Zr alloys, the ε_s was approximately 0.23-0.25%. With increasing of Ti, this value was reduced to 0.18% and further to 0.14% in the non-treated Al-4 wt% Cu-0.2 wt% Zr-0.03 wt% Ti alloy and the non-treated Al-4 wt% Cu-0.2 wt% Zr-0.06 wt% Ti alloy, respectively. The application of UST resulted in a reduction of ε_s to 0.16% in the Al-4 wt% Cu alloy, and to around 0.1% in the rest experimental alloys containing Zr or both Zr and Ti.

There may be two factors acting here. On one hand, the decreasing of contraction onset temperature caused by UST directly results in the shortening of the effective solidification interval, which is between the temperature of contraction onset and the non-equilibrium solidus. As a consequence, the thermal contraction in this solidification interval is reduced.
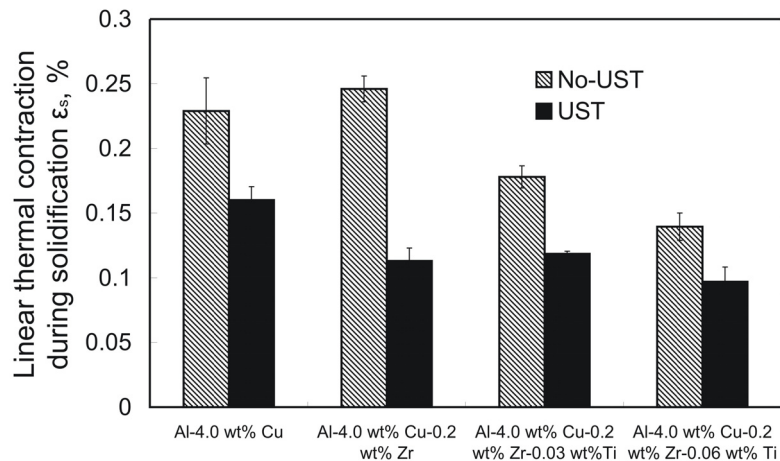

Figure 6.10 Linear thermal contraction during solidification in the four experimental alloys with and without ultrasonic processing.
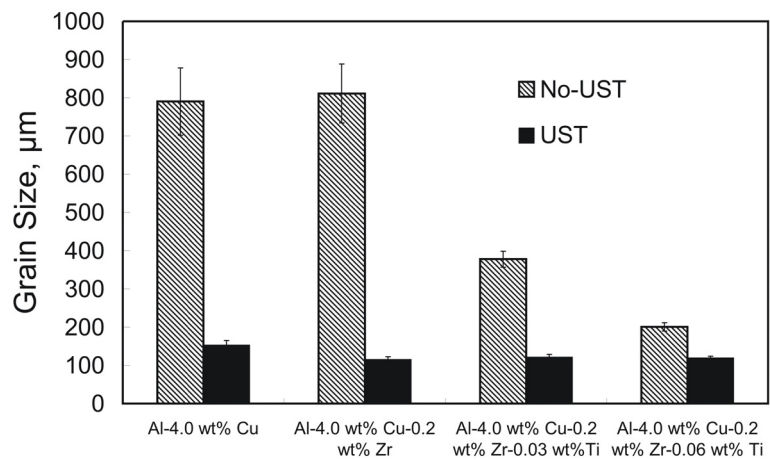
Figure 6.11 The quantitative information of grain size in the middle of the samples without and with UST.

On the other hand, during further solidification after the contraction onset, the refinement of grain structure in the middle part of the sample caused by UST might also delay the formation of the rigid skeleton in this region (region B in Fig. 6.9), and therefore, decreasing the contribution by this region to the total amount of contraction during solidification. The grain structures in the middle part of the samples are shown in Fig. 6.5 to

118

Fig. 6.8, and the quantitative information is summarized in Fig. 6.11. By re-plotting the grain size in the middle part of the samples with respect to the amount of thermal contraction during solidification, the correlation between grain structures in the middle part of the samples and thermal contraction during solidification can be revealed clearly in Fig. 6.12. Another probable factor affecting this decrease in this semi-liquid or liquid region is the gas evolution and expansion. It is well known that cavitation facilitates the diffusion of dissolved gas to the ultrafine bubbles existing in the liquid [14, 15]. The coalescence of fine bubbles as a result of acoustic streaming, radiation pressure, as well as Bjerknes and Bernoulli forces, offers a potential for degassing [15]. However, a short term ultrasonic processing and the relatively high cooling rate used in our experiments might not be able to provide enough time for the formation or floating up of large bubbles. In this case, UST has minor effect on degassing, but still might strongly influence the evolution of gases during solidification. It is suggested that UST accelerates the gas evolution and expansion in semi-liquid or liquid region, which offers more resistance to contraction during solidification, and results in the decrease of linear thermal contraction during solidification. The refinement of grain structure in these regions caused by UST further enlarged this effect, because it provided more interfaces for gas precipitation.
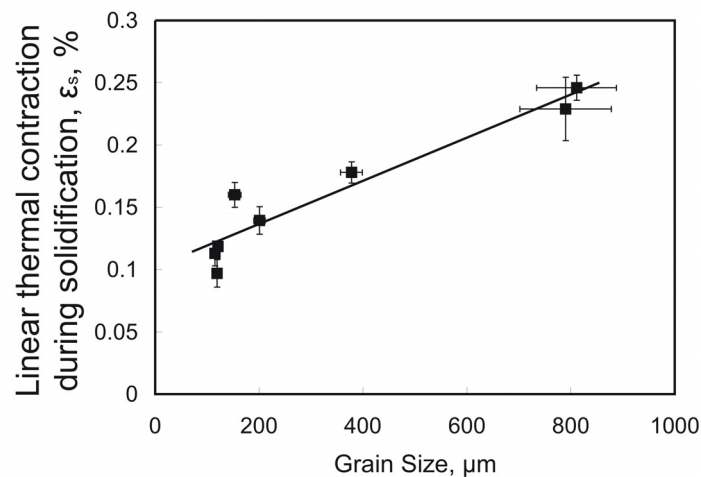
Figure 6.12 The effect of grain structure in the middle part of the samples on thermal contraction during solidification

6.3.2 Effect of the temperature of UST

Melt temperature is one of the important factors determining the efficiency and mechanisms of UST, as have been shown in section 4.4. The aim of this part of the research is to analyze the effect of the temperature of UST on grain structures both close to bottom and in the middle of the sample, and then to evaluate the effect of these structures on contraction behaviors during solidification.

The Al-4 wt% Cu alloy was again selected. The melt (appr. 0.2 kg) in the crucible was subjected to UST (4 kW) at 810 ˚C, 760 ˚C or 710 ˚C for 10 s. After UST, the melt was

either cast at 710 ˚C (UST at 810 ˚C and 760 ˚C) or directly cast into the cavity (UST at 710 ˚C). Sample without UST were produced by casting at 710 ˚C.

Figure 6.13 shows the grain structures in the Al-4 wt% Cu alloy after UST at 810 ˚C and 760 ˚C, respectively. The grain structures in non-treated alloys and the treated alloy at 710 ˚C can be found in Fig. 6.5. In the Al-4 wt% Cu alloy, columnar structures close to bottom and large Al grains in the middle were found in the alloys treated at 810 ˚C (Fig. 6.13 (a) and (b)) and 760 ˚C (Fig. 6.13 (c) and (d)). These structures are similar to the structures in non-treated alloy, as shown in Fig. 6.5 (a) and (b). The grain refinement only appeared in the alloy treated at 710 ˚C (Fig. 6.5 (c) and (d)) as a result of fragmentation of dendrites caused by UST. The grain size in the middle of samples is summarized in Fig. 6.14.
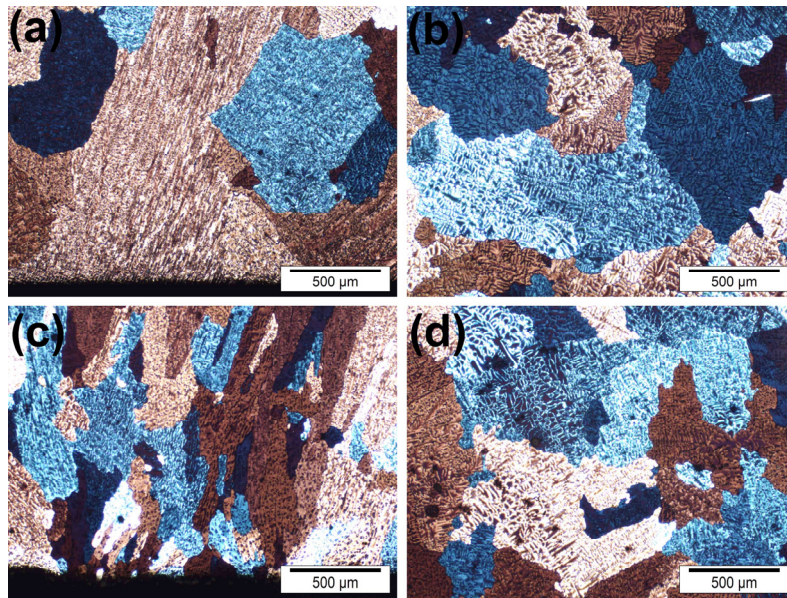

Figure 6.13 The grain structure in the Al-4 wt% Cu alloys: (a) UST at 810 ˚C, at the bottom part of the sample; (b) UST at 810 ˚C, in the middle part of the sample; (c) UST at 760 ˚C, at the bottom part of the sample and (d) UST at 760 ˚C, in the middle part of the sample.
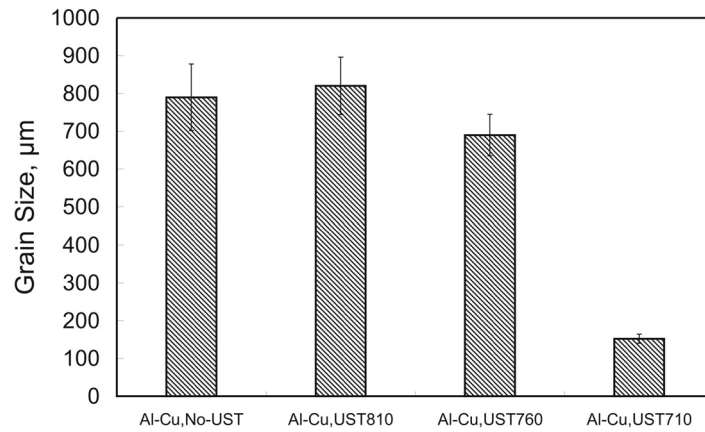
Figure 6.14 Grain size in the middle of Al-4 wt% Cu alloy samples without and with UST at different temperatures.

From the observation of the different grain structures caused by UST, we can analyze the contraction behavior in these alloys. Fig. 6.15 shows the effect of UST temperature on the contraction onset of the Al-4 wt% Cu alloy. The contraction onset temperature decreases with decreasing UST temperature. When compared with non-treated alloy, we can find that UST at high temperature (810 ˚C and 760 ˚C) did not result in a decrease of contraction onset temperature, since large columnar structures still appeared close to the bottom after UST. This confirmed our suggestion in previous section that grain structures close to the bottom area mainly determine the temperature when the rigidity skeleton forms, thus, influences the contraction onset temperature.
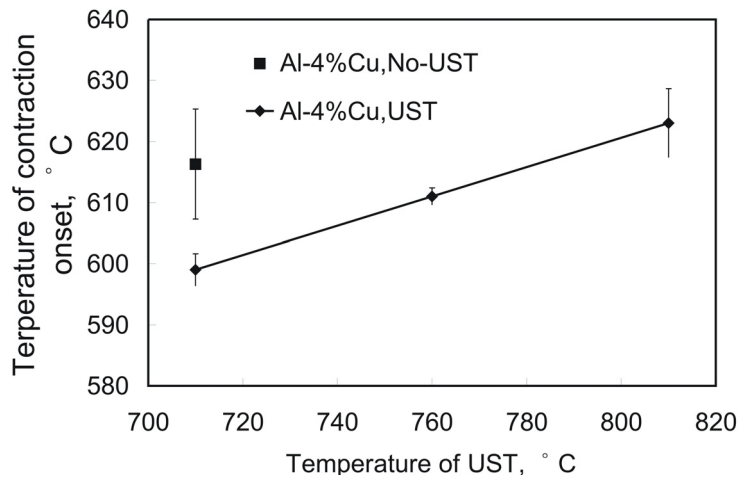

Figure 6.15 The effect of UST temperature on the contraction onset in the Al-4 wt% Cu alloy.
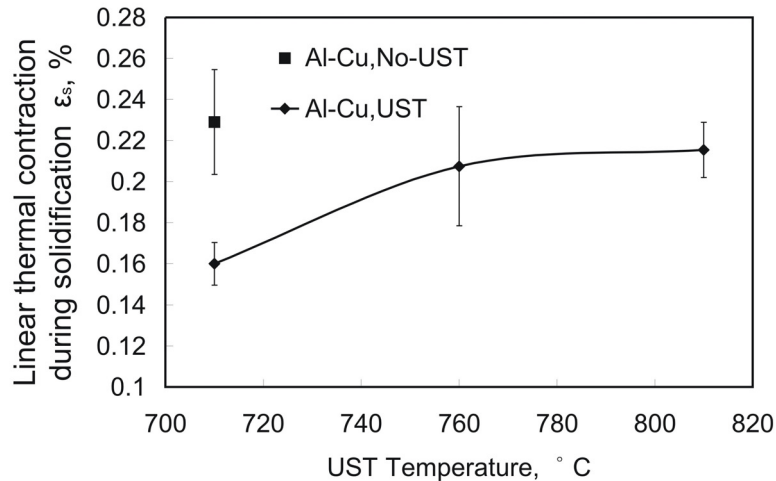
Figure 6.16 The effect of UST temperature on the linear thermal contraction during solidification in the Al-4 wt% Cu alloy.

The same trend can be found for the linear thermal contraction during solidification, as shown in Fig. 6.16. The grain structure in the middle part of the sample is suggested as one of the main factors since it influences the contribution by this region to the amount of total contraction during solidification of the sample and also the gas evolution. A slight decrease of ε_s in the alloys treated at 810 ˚C and 760 ˚C as compared with non-treated alloy can still be found while similar grain structure was obtained in the middle of these alloys. This might be the result of the acceleration of the gas evolution and expansion in semi-liquid or liquid region caused by UST, as we suggested in previous section.

6.4 Factors affecting thermal contraction after solidification

6.4.1 Decreasing of TCC at high temperature caused by UST

After the measured temperature reached the non-equilibrium solidus, the further contraction is represented by thermal contraction coefficient (TCC). We wanted to verify first if the ultrasonic processing further affect the thermal contraction in the solid state. Let us first have a look at the TCC at different temperatures in the Al-4 wt% Cu alloy treated at different melt temperatures (810 ˚C, 760 ˚C and 710 ˚C), which is shown in Fig. 6.17. The plotted TCC is the average TCC for each 100°C temperature range or for the range [500 ˚C, NES].
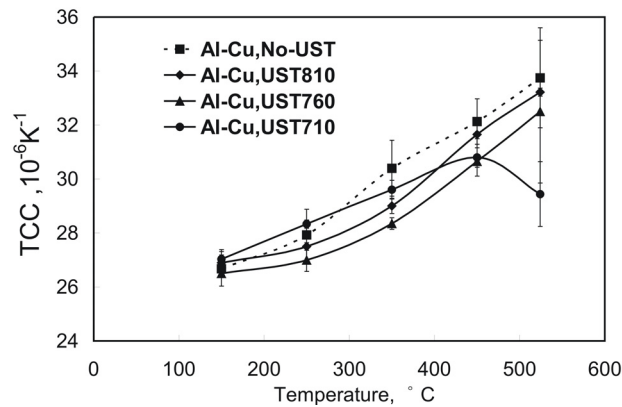
Figure 6.17 The TCC at different temperature in the Al-4 wt% Cu alloy treated
at different melt temperature. Dashed line, No-UST; Solid lines, UST.

The most notable observation in this figure is that at high temperature close to non-equilibrium solidus, the TCC decreased significantly, only when UST was applied at 710 ˚C. Therefore, the question is what might cause this TCC drop?

In order to answer this question, it is necessary to consider the previous experimental results obtained in our research group using an AA7075 alloy [4]. During that research, different sample heights were studied, 25 mm and 12 mm. In the case of a 25-mm high sample, the TCC decreased with decreasing temperature in the non-grain refined AA7075 alloy, as shown in Fig. 6.18 (a). This is in good agreement with reported data [5, 16, 17] and our current results. However, when the grain refiner was used, the TCC increased with decreasing temperature. In the case of a 12 mm high sample, the TCC decreased with decreasing temperature in both the grain-refined alloy and the non-grain-refined alloy, as illustrated in Fig. 6.18 (b).
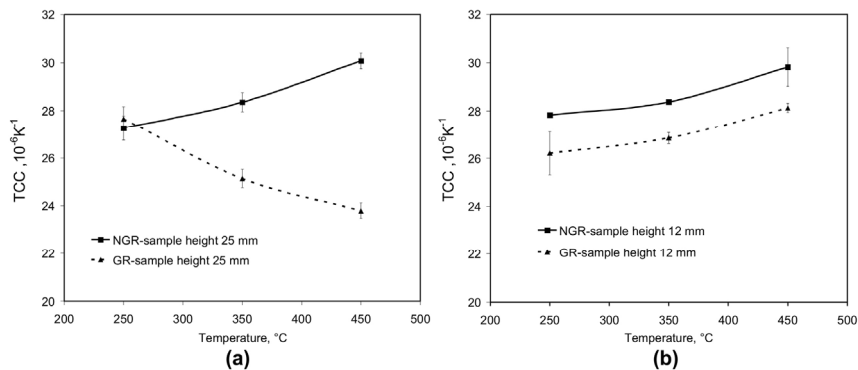

Figure 6.18 Effect of sample height on the linear thermal contraction
coefficient in an as-cast AA7050 alloy with (0.05% Ti) and without grain
refiner: (a) sample height 25 mm and (b) sample height 12 mm [4].

Two factors were suggested to explain these results. Firstly, the inhomogeneity of the solidifying sample, see Fig. 6.9, resulted in the uneven contraction for the whole samples (duo to the sample is not yet fully solid) at high reference temperatures. The volume of the sample, which was still liquid or in transition region above the rigidity point and did not undergo contraction at relatively high reference temperatures, increased with grain refining. However, the measured temperature corresponding to the rigidity point (contraction onset), did not depend on the sample height. So the higher the sample was, the more time or the more temperature decrease it needed to "activate" the whole sample's contraction, and the less the calculated TCC at high temperature was. This trend became more intense when a larger amount of grain refiner was employed. Secondly, a higher sample provided more time for the gas evolution and expansion, which offered the resistance to the contraction and should be more pronounced in the grain-refined alloy as there were more interfaces available for gas precipitation.

Based on these results, we reduced the sample height to 12 mm in our experimental setup, which has a positive effect on reducing the inhomogeneity of the solidifying sample and it is believed that the results obtained with the 12-mm high sample better represent the real material properties.

Coming back to our experiments and to the grain structures in the middle part of the samples shown in section 6.3.2, we can observe that a remarkable grain refinement only took place in the alloy treated at 710 ˚C (Fig. 6.5 (d)), while coarse grains were observed in the alloys treated at 810 ˚C (Fig. 6.13 (b)) and 760 ˚C (Fig. 6.13 (d)), as well as in the non-treated Al-Cu alloy (Fig. 6.5 (b)).

According to this result, admittedly, inhomogeneity of solidifying sample and the corresponding changes in the measured TCC persisted in the samples when the grains were refined by UST. However, the 12 mm sample height selected in these experiments, had already been proved to suppress the unusual trend of TCC in the AA7075 alloy with grain refiner. Therefore, why do we observe a decrease of the TCC in the Al- 4 wt% Cu alloy when treated by UST at 710 ˚C, and only at high reference temperature?

To answer this question, we can have a look at the TCC in other experimental alloys, which were analyzed in section 6.3.1. Fig. 6.19 shows the variation of the TCC with temperature in the Al-4 wt% Cu alloy, the Al-4 wt% Cu-0.2 wt% Zr alloy, the Al-4 wt% Cu-0.2 wt% Zr-0.03 wt% Ti alloy and the Al-4 wt% Cu-0.2 wt% Zr-0.06 wt% Ti alloy. The most common change when UST was applied is that the TCC at high temperature decreased as compared to non-treated alloys. This effect becomes even more obvious when Zr and Ti were added, as shown in Fig. 6.19 (c) and (d). However, a similar grain structure in the middle of the samples was observed in the treated alloys containing Zr or both Zr and Ti, as shown in Fig. 6.11. Thus, it seems that the decreasing of TCC at high reference temperatures that was observed in these treated alloys is not only related to inhomogeneity, which is mainly determined by grain structure in the center. Two other aspects of ultrasonic processing, besides the grain refinement in the centers, should be taken into account in order to explain this TCC decrease at high temperature.
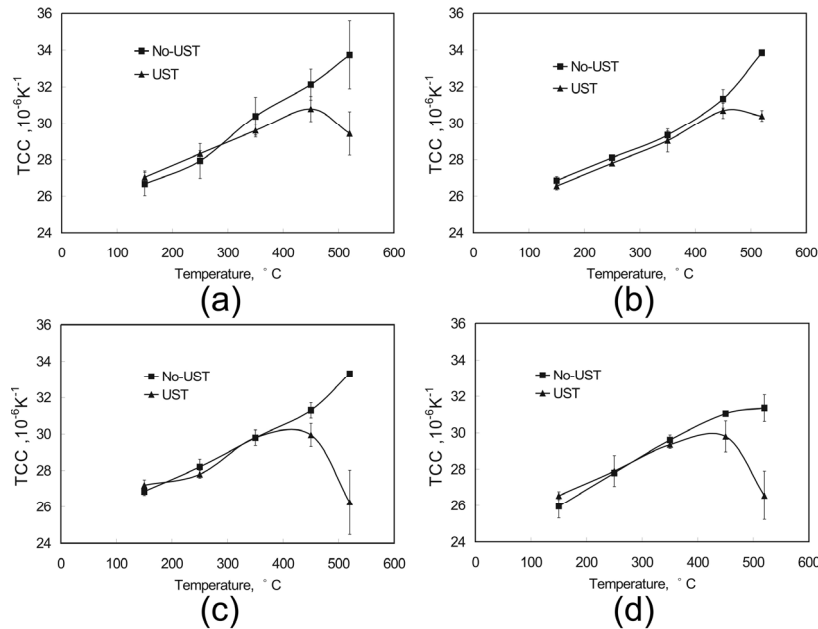
Figure 6.19 The TCC at different temperatures without and with UST at 710 ˚C: (a) the Al- 4 wt% Cu alloy; (b) the Al- 4 wt% Cu-0.2 wt% Zr alloy; (c) the Al- 4 wt% Cu-0.2 wt% Zr-0.03 wt% Ti alloy and (d) the Al- 4 wt% Cu-0.2 wt% Zr-0.06 wt% Ti alloy.

As we mentioned before, when the measured temperature (close to the bottom) reached the non-equilibrium solidus, a solid layer is formed and starts to contract, while the above region is still in semi-liquid or liquid state. The gas precipitation in this solid region might have a direct impact on the calculated TCC at high temperature close to the non-equilibrium solidus. The precipitation of the gas after solidification has been shown to offer a noticeable contraction resistance [4, 8]. Thus, the grain refined structure close to bottom caused by UST provides more interfaces for the gas precipitation than the large columnar structure in those non-treated alloys. This is probably the reason why UST at high temperature, such as 810 ˚C (Fig. 6. 13 (a)) and 760 ˚C (Fig. 6.13 (c)), did not result in a decrease of TCC at high reference temperature in the Al-4 wt% Cu alloy. Similar explanation can be offered for the observed smaller decrease in the treated Al-4 wt% Cu alloy at 710 ˚C (Fig. 6.5 (c)) and the treated Al-4 wt% Cu-0.2 wt% Zr alloy (Fig. 6.6 (c)), which still contained columnar structure after UST. However, The refined grain structure close to bottom in the treated Al-4 wt% Cu-0.2 wt% Zr-0.03 wt% Ti alloy (Fig. 6.7 (c)) and the treated Al-4 wt% Cu-0.2 wt% Zr-0.06 wt% Ti alloy (Fig. 6.8 (c)) resulted in a large decrease in TCC at high reference temperature close to non-equilibrium solidus.

Another factor affecting the TCC decrease might also come from the acceleration of the gas evolution and expansion in semi-liquid or liquid region caused by UST. This effect becomes significant only if the grain structure is fine enough to delay the formation of the rigidity skeleton in the center, thus providing more time for gas evolution and expansion in

125

semi-liquid or liquid region at high reference temperature. This might be the reason why the TCC only decreased at high reference temperature.

6.4.2 Solid thermal contraction at low temperature

As cooling progresses, the TCC measured at lower temperature is also an important physical property of the materials. Conventionally, the linear thermal expansion coefficient (LTEC) is used as a reference data for this property. It is worth to note that there is no direct comparison between the TCC we measured in this work and the reference data on LTEC, because of essentially different experimental conditions [7]. Firstly, LTEC is usually determined by a dilatometer on long cylindrical (one-dimensional) samples under nearly isothermal conditions (i.e., no thermal gradients in the sample) [7]. Secondly, these samples are carefully homogenized to achieve the equilibrium state of the alloy. This situation is very different from the real contraction conditions of a just solidified and cooling bulk sample in which the processes of excess-phase precipitation may well continue [7].

From Fig. 6.19, we can see that UST has no obvious effect on the TCC at low temperature range under the given casting conditions of these alloys. However, UST applied at high temperature (810 ˚C and 760 ˚C) resulted in a slight decrease in the TCC at low temperature when comparing with the alloy treated at 710 ˚C and the non-treated alloy, as illustrated in Fig. 6.16. A possible reason is that the initial absorbed hydrogen in the melt increased with increasing melt superheat. The gas precipitation in the solid state at low temperature counteracted the contraction, which results in the decrease of TCC at low temperature [4, 8]. The melt which was treated at 810 ˚C should have more hydrogen content as compared with the melt treated at 760 ˚C, and then have smaller TCC at low temperature. However, our experimental results on TCC were the other way around in these two alloys. A suggested reason is that after UST at 810 ˚C, the melt was still at high temperature above the casting temperature of 710 ˚C. The time for cooling of the melt to the casting temperature gives the possibility of the floating up of large bubbles after UST until cast into the mold. Therefore, in this case, the hydrogen content in the alloy treated at 810 ˚C might be lower than that in the alloy treated at 760 ˚C, as a result of ultrasonic degassing.

6.4.3 Role of gas precipitation in the solid state on TCC

In the discussion above, the gas precipitation in the solid state was always suggested to play an important role in the decreasing of TCC at lower temperature. In this section we study this effect in more details.

In our previous experiments with AA7075 alloy, the effect of initial gas saturation was also studied [4]. Two charges were prepared in the following manner. (1) A steel container with water was placed in the furnace along with the crucible with the melt. Water evaporated and created a humid atmosphere in the closed furnace. Before contraction experiments, the melt was exposed for 30 min to the humid air in the furnace. (2) The same amount of melt was prepared under dry (normal atmospheric) conditions. It is suggested based on the literature [3, 14] that the hydrogen concentration was about 0.8-1.0 cm^3/100 g in the case of

126

humid air; and 0.3-0.4 cm^3/100 g in the case of dry air. The sample height was 25 mm in this experiment.

Figure 6.20 demonstrates the TCC for AA7050 alloys cast under different conditions. The TCC in the case of dry-air atmosphere is higher than that in the case of vapor-enriched atmosphere, also in lower temperature range, although the inhomogeneity of solidifying samples strongly influenced the trend of TCC in the 25-mm high sample, as shown in section 6.4.1. The main mechanism was believed to be the precipitation of the gas after solidification.
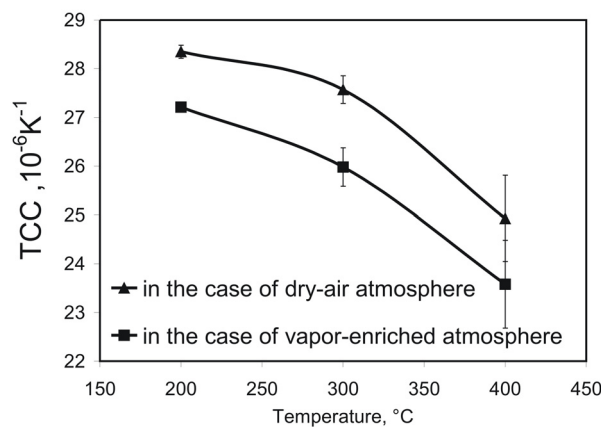

Figure 6.20 The effect of gas saturation on the linear thermal contraction
coefficient in a grain-refined as-cast AA7050 alloy. Sample height 25mm [4].

Since the gas precipitation was found to be an important factor affecting TCC, therefore, it is worth to study the effect of cooling rate after solidification on TCC, because it directly influences the time available for gas precipitation and it is also an important factor for cracking susceptibility.

The Al-4 wt% Cu alloy was used for this study. The casting condition is the same as that in section 6.4.1 except for the cooling rate. In this experiment, the cooling water was switched off before casting so that no water was running through the water cooled base during the whole solidification. Fig. 6.21 is the recorded cooling curves in the experiments with and without cooling water. The cooling conditions above 400 ˚C were roughly the same, which means that even without cooling water, the bronze base was still able to provide a high cooling rate when the melt first contacted the mold. The cooling rate started to decrease below 400 ˚C in the experiment without cooling water.

Due to similar cooling conditions at the beginning of casting, the temperature of contraction onset, and the linear thermal contraction during solidification in the samples cast without cooling water were pretty consistent with the results from the samples cast with cooling water, which were presented in section 6.4.1. It confirms that the used technique is highly reproducible.

The effect of cooling rate below 400 °C vividly reflected in the TCC curves at low temperature ranges, as shown in Fig. 6.22. Lower cooling rate resulted in lower TCC at all temperatures below 400 °C, both with and without UST. The longer time available for gas precipitation due to the lower cooling rate is considered as the main reason for the decrease of TCC at low temperature. Therefore, a lower thermal contraction coefficient at lower cooling rate may be one of the contributors to the lower cracking susceptibility, which is introduced in section 1.2.2.
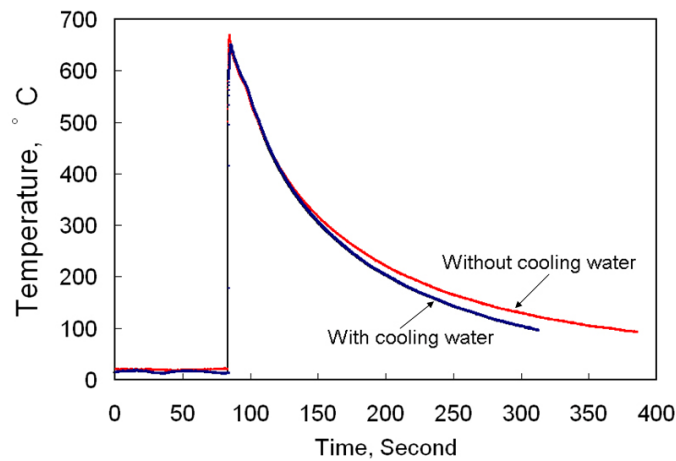

Figure 6.21 Recorded cooling curves in the cases of with cooling water and without cooling water during experiments in the Al-4 wt% Cu alloy.
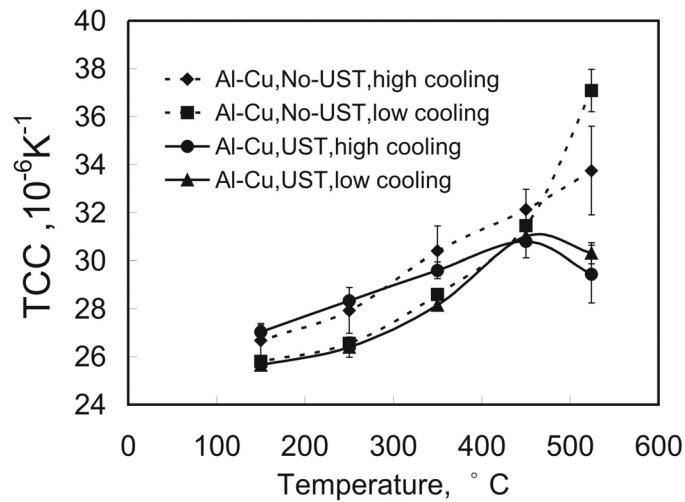

Figure 6.22 The TCC at different temperatures in the Al-4 wt% Cu alloy cast with and without cooling water. Dashed line, No-UST; Solid lines, UST.

6.5 Conclusions

Through the results of this chapter, a relationship among grain structures, ultrasonic processing and thermal contraction behavior in aluminum alloys were revealed. The temperature of contraction onset mainly depends on the grain structure in the region where the first rigid skeleton is formed and contributes to the contraction. UST facilitates the formation of equiaxed dendrite structure close to the bottom, especially when Zr and Ti are present in the alloy, and as a result, decreases the contraction onset temperature.

This decrease in the onset temperature directly leads to shortening of the effective solidification interval, and therefore, to lower linear thermal contraction during solidification. UST may also contribute to the decreased solidification contraction through other two effects. On one hand, the refinement of grain structure in the center of the sample delays the formation of rigid skeleton in the upper layers of the sample, which deceases the contribution of these layers to the total measured contraction during solidification. On the other hand, UST may accelerate the gas evolution and expansion during solidification in semi-liquid or liquid region, which offers more resistance to contraction during solidification, and decreases the overall linear solidification contraction. This promising effect of UST on linear solidification contraction is significant since it determines the amount of thermal strain/stress accumulated in the solidification range.

Grain refinement by UST may also be responsible for the apparent decrease of the TCC at high temperature close to non-equilibrium solidus. The inhomogeneity of solidifying sample due to the experimental setup used in this work can contribute to the decreased TCC at high reference temperature when the grains are refined by UST. In addition, more intensive gas precipitation in the refined semi-solid region might also play a role in this decrease.

At lower temperature in the solid state, UST has no obvious effect on the TCC. The gas precipitation in the whole solid sample is the main factor affecting the TCC at low temperature. A lower cooling rate in the solid state resulted in the decrease of TCC. This might be explained by the increasing of the time for gas precipitation in the solid state. Thus, a lower thermal contraction coefficient observed at a lower cooling rate may be one of the contributors to the lower cracking susceptibility.

References:

[1] J.Campbell, *Castings*. 1991, Oxford, U.K.: Butterworth-Heinemann.

[2] D.G.Eskin and L.Katgerman, *Metall. Mater. Trans. A*, 2007. **38A**: p. 1511-1519.

[3] V.A.Livanov, R.M.Gabidullin, and V.S.Shipilov, *Continuous Casting of Aluminum Alloys*. 1977, Moscow: Metallurgiya.

[4] L.Zhang, D.G.Eskin, M.Lalpoor, and L.Katgerman, *Mater. Sci. Eng. A*, 2010. **527**: p. 3264-3270.

[5] I.I.Novikov, *Hot Shortness of Nonferrous Metals and Alloys*. 1966, Moscow: Nauka.

[6] E.C.Ellwood and J.M.Silcock, *J. Inst. Met.*, 1948. **74**: p. 457-467.

[7] D.G.Eskin, Suyitno, J.F.Mooney, and L.Katgerman, *Metall. Mater. Trans. A*, 2004. **35A**: p. 1325-1335.

[8] V.K.Afanas'ev and V.F.Frolov, 2002. **44**: p. 9-10.

[9] L.F.Mondolfo, *Aluminum alloys: Structure and Properties*. 1979, London: Butterworths.

[10] N.A.Belov, D.G.Eskin, and A.A.Aksenov, *Multicomponent Phase Diagrams: Applications for Commercial Aluminum Alloys*. 2005, Amsterdam: Elsevier.

[11] P.N.Anyalebechi, *Scripta Metal. Mater.*, 1995. **33**(8): p. 1209-1216.

[12] L.Arnberg, L.Bäckerud, and G.Chai, *Dendrite Coherency, in: Solidification Characteristics of Aluminum Alloys, vol. 3*. 1996, Des Plaines, IL: American Foundrymen's Society.

[13] A.Stangeland, A.Mo, and D.G.Eskin, *Metall. Mater. Trans. A*, 2006. **37A**: p. 2219-2229.

[14] G.I.Eskin, *Ultrasonic Treatment of Light Alloy Melts*. 1998, Amsterdam: Gordon and Breach Science Publishers.

[15] O.V.Abramov, *Ultrasound in Liquid and Solid Metals*. 1994, Boca Raton,FL: CRC press.

[16] J.R.Davis, ed. *ASM Specialty Handbook: Aluminum and Aluminum Alloys*. 1993, ASM International, Materials Park, OH, pp. 696–697.

[17] A.E.Vol, *Handbook of Binary Metallic Systems: Structure and Properties, vol. 1*. 1966, Jerusalem: Israel Program for Scientific Translations.

Chapter 7

Fluidity of aluminum alloy melts under UST and ultrasonic degassing

7.1 Introduction

A fine grain structure, a uniform distribution of alloying elements and a low cracking susceptibility are the goals of engineers and foundry workers for improving the properties of Al alloys. As we presented in previous chapters, the proper application of ultrasound may help in achieving this goal. However, having only these features does not guarantee a prefect casting. Other casting properties, such as fluidity and soundness (less porosity), strongly influence the quality of final products. This chapter will focus on these two casting properties.

The fluidity of molten metal is especially important in net shape castings. More and more complicated component designs and a growing demand for mechanical properties of aluminum alloys in aerospace and automobile applications make the filling of the mold an overarching priority. Although the pressure-assisted die casting largely overcomes this problem, the further improvement of fluidity is still necessary for meeting the stringent requirements in the thinner section of the investment and gravity-casting molds. The application of ultrasonic processing provides a possibility for improving the fluidity of molten aluminum alloys, since several benefits have been reported, such as grain refinement, melt purification etc. [1, 2]. However, few reports are available on the effect of UST on the fluidity of molten aluminum alloys. Therefore, one of the main objectives in this chapter is to study how ultrasonic processing affects the fluidity in aluminum castings.

Degassing processing in industrial aluminum castings is crucial to minimize the detrimental effect caused by hydrogen porosity defects. As we mentioned in Chapter 1, the most common method for industrial degassing is the rotary degassing. The inert gas (argon or nitrogen) is introduced in the molten aluminum alloy and is dispersed into large amount of tiny bubbles by a rotor [3]. The floating up of these bubbles together with absorbed hydrogen results in a degassing effect. However, a high purity inert gas without oxygen [4] and a long term treatment are required for this degassing processing, which increases the production cost. Ultrasonic degassing, as an environmentally clean and relative inexpensive technique, has attracted a lot of research [5-10]. Therefore, in this chapter, a preliminary analysis was preformed in order to demonstrate the promising degassing effect caused by UST.

The present chapter starts with experimental results on the effect of ultrasonic processing on the fluidity in an Al-4 wt% Cu alloy. The effect of additions of Zr and Ti, as well as the effect of melt quality (oxide inclusions) on the fluidity under ultrasonic processing is studied. The second part of this chapter presents the effect of ultrasonic processing on degassing in an Al-4 wt% Mg alloy. The ultrasonic degassing effect under different ultrasonic processing times and initial hydrogen contents in the melt are shown and discussed.

7.2 Experimental procedure

7.2.1 Fluidity test procedure

A simple mold shape was used in this research to measure the fluidity. A schematic diagram of this setup is shown in Fig. 7.1. It mainly consists of a pouring cup with a

stopper on the bottom, a brass base with two identical straight flow channels and a graphite cover on the top of the brass base during testing. At the end of each flow channel, a narrow hole was drilled for the escape of the gases. In order to reduce the rate of heat removal and smooth the surface of the channel, a BN coating was used on the surface of the flow channel and the bottom side of the graphite cover. Before the experiment, the whole system was preheated to 80-90 ˚C. The temperature was measured by a K thermalcouple attached to the graphite cover.
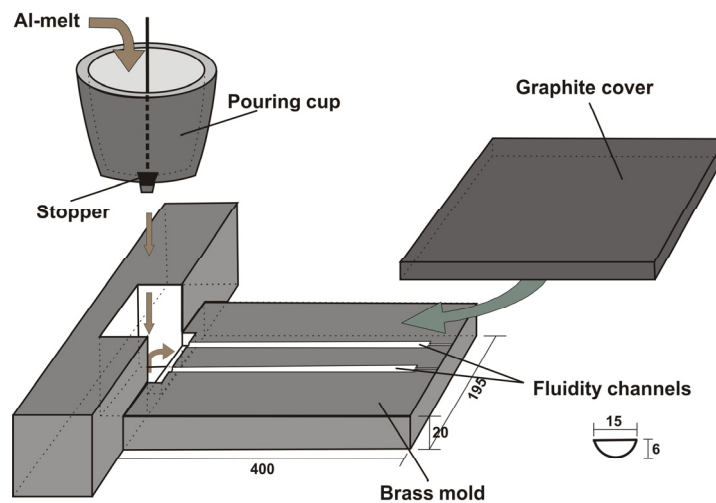

Figure 7.1 A schematic diagram of the fluidity test mold in this research.
Brown arrows indicate the melt flow path. Dimensions are given in
millimeters.

During the experiment, a fixed amount of melt (appr. 0.35 kg) was first treated by ultrasound (4 kW) at 740 ˚C or 770 ˚C in the crucible for 10 s, cooled in air until 710 ˚C, and then cast into the preheated pouring cup. Without UST, the melt was directly cast into the pouring cup at 710 ˚C. After filling the cup, the stopper was removed immediately and the melt filled the flow channels. The average flow length of two channels is taken as the fluidity value of the test. An example of cast sample is shown in Fig. 7.2.

Before the experiments, the accuracy of the measurement of fluidity using this setup was evaluated. Five fluidity tests were preformed under the same casting conditions and the results were used to calculate the variance of the tests. This variance was assumed valid for all tests and was used to calculate the interval of confidence for each test, with a confidence level of 95%. The interval of confidence is plotted as the error bar.
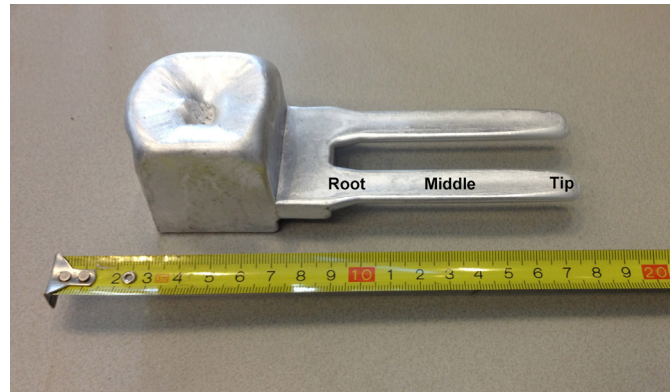
133

Figure 7.2 An example of cast sample for fluidity test. The microstructure was examined in root, middle and tip areas.

The alloy used for the experiment on fluidity was Al-4 wt% Cu. For some tests 0.16 wt% Zr and 0.06 wt% Ti was added in order to study the effect of grain structure on the fluidity. The effect of oxide inclusions on the fluidity under UST was also studied through mixing extra aluminum oxide films into the melt. The grain structure was examined along the cast strip length at three different positions: root, middle and tip areas, as marked in Fig. 7.2.

7.2.2 Degassing test procedure

For the ultrasonic degassing experiments, an Al-4 wt% Mg alloy was selected in order to obtain a higher (due to Mg presence) initial hydrogen content in the melt. During experiments, the melt was first prepared in the furnace with dry atmosphere, and then treated by UST (4 kW) in the crucible (appr. 0.4 kg melt) at 720 ˚C. Different ultrasonic processing times, from 30 s to 10 min, were used. In order to prevent the solidification during the early stage of ultrasonic processing, the crucible was placed in a resistance furnace with a temperature of 700 ˚C during UST. However, if during the UST the melt temperature increases again above 720 ˚C, both the crucible and sonotrode were moved out of the furnace. After UST, the melt was directly cast into a copper mold (melt temperature is lower than 720 ˚C after UST) or at 720 ˚C (melt temperature is higher than 720 ˚C after UST). Without UST, the sample was produced by casting the melt directly at 720 ˚C.

The effect of a higher content of initial hydrogen was also studied through exposing the melt to a vapor-enriched furnace atmosphere for 40 min before the ultrasonic processing. The following procedure steps were the same with the case of dry furnace atmosphere above.

After casting, the grain structure of all samples was examined in the middle of the sample by using an optical microscope. Afterwards, the lower part of the sample (not including the shrinkage cavity) was cut into small pieces in order to measure the density of the specimens, which was used to determine the porosity level of the melt. The measurement of the density in this research was done using the apparent density measurement method [11]. The

134

specimens were weighed in air and in water. The density D, of the specimen is given by the following equation:

$$D = \frac{m_a}{m_a - m_w} \; ,$$

(7.1)

Where m_a and m_w are the weights of the specimen measured in air and water, respectively. The error bar in this experiment was determined using the same procedure as that in the section 7.2.1.

7.3 The fluidity of molten Al alloy under UST

7.3.1 Effect of grain structure on the fluidity

In previous chapters, we showed the grain refinement caused by UST. In this section, an Al-4 wt% Cu alloy and an Al-4 wt% Cu-0.16 wt% Zr-0.06 wt% Ti alloy were treated at different ultrasonic processing temperatures, 740 ˚C and 770 ˚C, in order to analyze the effect of UST and grain structure on the fluidity.

Figure 7.3 shows the measured fluidity length under different casting conditions. As we can see, the fluidity remained roughly the same when UST was applied to the Al-4 wt% Cu alloy as compared to non-treated alloy, although a slight increase in fluidity was found after a treatment at 770 ˚C. When UST was applied to the Al-4 wt% Cu-0.16 wt% Zr-0.06 wt% Ti alloy, a noticeable increase of the measured fluidity length was observed, both in the alloys treated at 740 ˚C and 770 ˚C.
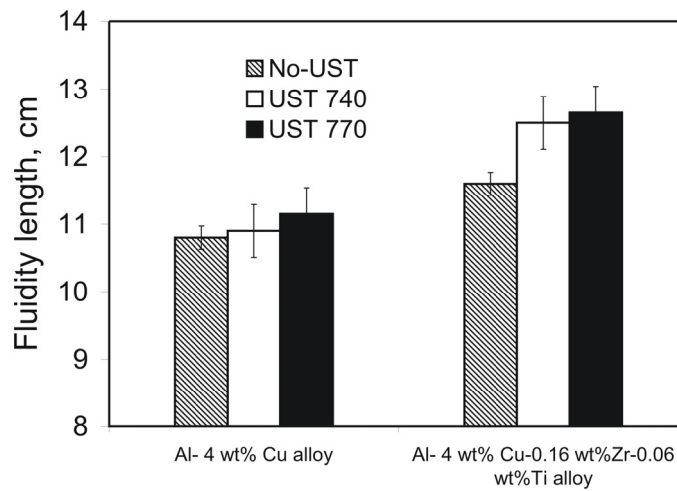

Figure 7.3 The measured fluidity length under different ultrasonic treatment temperatures in the Al-4 wt% Cu alloy and in the Al-4 wt% Cu-0.16 wt% Zr-0.06 wt% Ti alloy.

135

Among several factors affecting the fluidity, which we introduced in Chapter 1, the grain structure was considered as the main factor in this research. Looking deep into the grain structures, we can find that the equiaxed dendritic grain structure was formed along the whole fluidity strip, no matter where the sample was taken: in the root, middle or tip areas. The grain size in all studied alloys is summarized in Fig. 7.4. The grain structures in the middle of some selected samples can be found in Fig. 7.5. The grain size decreased more or less when UST was applied. This is in agreement with our conclusions in previous chapters, but it is not the focus of the research in this section.
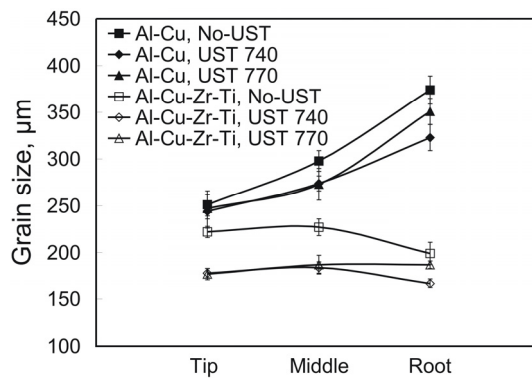

Figure 7.4 The grain size at different positions along the fluidity strips in all studied alloys.
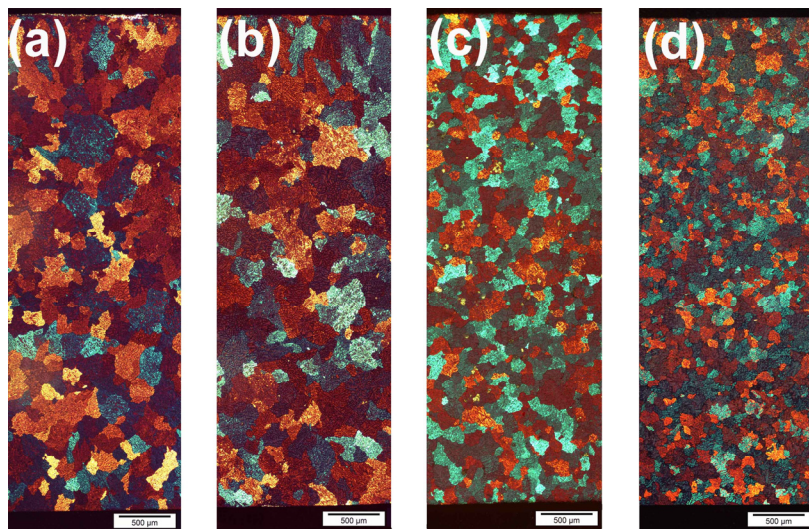

Figure 7.5 The grain structures in the middle of some selected samples: (a) the Al-4 wt% Cu alloy, without UST; (b) the Al-4 wt% Cu alloy, UST at 740 ˚C; (c) the Al-4 wt% Cu-0.16 wt% Zr-0.06 wt% Ti alloy, without UST; and (d) the Al-4 wt% Cu-0.16 wt% Zr-0.06 wt% Ti alloy, UST at 740 ˚C.

By plotting the fluidity length versus the grain size in the middle areas, as illustrated in Fig. 7.6, we can find that a clear correlation between the fluidity length and the grain size. A smaller grain size means a higher solid fraction of dendritic crystals in semi-liquid melt required for the impingement of the grains and then the formation of mixture stiffens, which provides more resistant to flow. This result is consistent with several reported data which showed the benefit of grain refinement for the fluidity of molten aluminum alloys [12, 13].
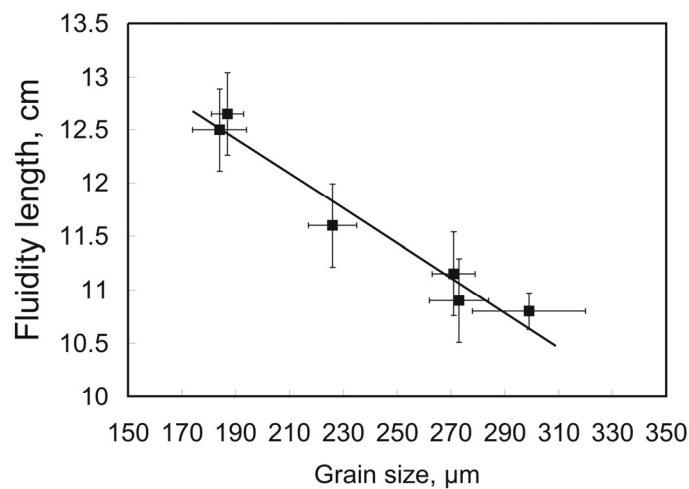

Figure 7.6 The correlation between the fluidity length and the grain size in all studied alloys.

7.3.2 Effect of oxide inclusions on the fluidity

In previous section, the results clearly show the grain refinement caused by UST resulted in the increasing of the fluidity. However, a slight improvement of the fluidity can be observed when UST was applied at a higher temperature, although the grain structure did not change much. Although this might due to the scatter of results, it might be also related to other benefits provided by UST. In this section, we will further study how UST affects the fluidity in aluminum alloy.

As one of other major factors, the oxide inclusions in the melt are reported to restrain the flow of molten metal [13-15]. Since these non-metallic inclusions are always present in aluminum melt, it is worth to investigate the behavior of oxide inclusions under UST in terms of fluidity.

In order to study this effect, extra aluminum oxide films were mixed into the melt three times (with 30 min interval between each) before UST when the melt was at 760 ˚C. After mixing, the melt was treated by ultrasound (4.0 kW) at 740 ˚C for 10 s, and then cast into the pouring cup at 710 ˚C. The rest of the experimental procedure can be found in section 7.2.

137

The extra oxide films mixed in the melt ('contaminated melt' as distinct from 'clean melt') decreased the fluidity in non-treated alloys, especially in the Al-4 wt% Cu-0.16 wt% Zr-0.06 wt% Ti alloy, as shown in Fig. 7.7. UST at 740 ˚C resulted in a complete recovery in the fluidity in the Al-4 wt% Cu alloy. Although in the Al-4 wt% Cu-0.16 wt% Zr-0.06 wt% Ti alloy, the fluidity in the case of contaminated melt under UST was lower than that in the case of clean melt under UST, ultrasonic processing still shows a promising effect on improving the fluidity of the contaminated melt. The grain size along the fluidity strip in these samples is summarized in Fig. 7.8. UST led to the grain refinement effect in both examined alloys.
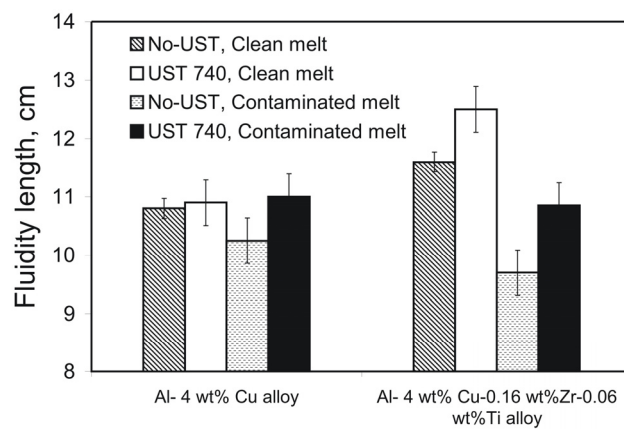

Figure 7.7 The measured fluidity length without and with UST after mixing extra oxide films in the Al-4 wt% Cu alloy melt and in the Al-4 wt% Cu-0.16 wt% Zr-0.06 wt% Ti alloy melt.
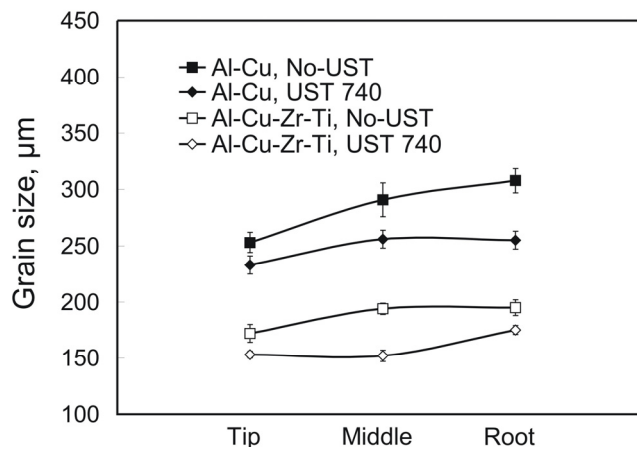

Figure 7.8 The grain size at different positions along the fluidity strips in all studied alloys with extra oxide films.

138

Usually the oxide inclusions in the melt offer resistance to melt flow in the fluidity channel because of the poor wettability of oxide in aluminum melt. These non-wetted oxide inclusions are easy to accumulate around the edge of flowing melt during the tumbling of dendrite crystals during flowing, which provide extra friction during contacting the surface of the mold. When the growing crystals are equiaxed, as shown in Fig.1.2, the oxide inclusions in the melt might also facilitate the coherency of growing dendrites, since they provide extra bridging between the grains. This effect becomes more noticeable when the grain size is smaller. This is a possible reason for the significant decrease of fluidity in the Al-4 wt% Cu-0.16 wt% Zr-0.06 wt% Ti alloy when extra oxides were mixed.

The application of UST, on one hand, improved the wettability of oxide inclusions in the melt. On the other hand, it might result in the fragmentation and dispersion of the mixed oxide films. Therefore, the fluidity was improved when UST was applied to the contaminated melt.

7.4 Degassing effect caused by UST

It is well known that ultrasonic processing results in a degassing effect when it is applied in the melt before casting [1, 2]. Although many parameters have been analyzed by several researchers, such as ultrasonic processing temperature [16, 17], treated melt volume [10, 16, 17] and ultrasonic power [17], this technique has not been applied widely in industrial aluminum castings. In this section, two major parameters affecting degassing, ultrasonic processing time and initial hydrogen content, were selected for a preliminary analysis on ultrasonic degassing.

The effect of ultrasonic processing time is the first discussed here since it determines directly the efficiency of ultrasonic degassing. Four ultrasonic processing times were used in our research: 30, 60, 300 and 600 s. The same amount of Al alloy melt (appr. 0.4 kg) was used for each test. Fig. 7.9 is the density of solidified samples with respect to the ultrasonic processing time. A good degassing effect can already be achieved by ultrasonic processing for 30 s in the case of the melt in dry atmosphere, while followed long-term processing had minor effect on further removal of the hydrogen from the melt. Introducing a higher initial content of hydrogen in the melt with a vapor-rich atmosphere led to an even stronger ultrasonic degassing effect, but the time for reaching the maximum degassing effect increased to 60 s.
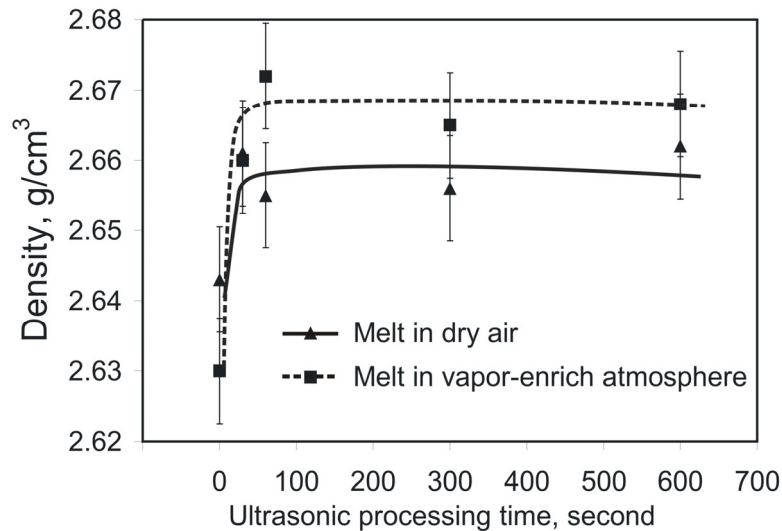
139

Figure 7.9 The density of solidified samples with respect to the ultrasonic processing time in the Al- 4 wt% Mg alloy.

An important message we obtained during this research is the time needed for maximum ultrasonic degassing effect. The efficiency of ultrasonic degassing is mainly related to this parameter. Several factors affecting this parameter have been revealed in reported data, such as ultrasonic processing temperature [16, 17], treated melt volume [10, 16, 17], ultrasonic power [17] etc. Our results show this parameter is also affected by the initial content of hydrogen in the melt.

The cavitation and acoustic streaming in the melt caused by UST is considered as the main mechanism of ultrasonic degassing. The cavitation bubbles existing in the melt promote the diffusion of dissolved hydrogen into the bubbles. The coalescence of these bubbles as a result of acoustic streaming facilitates the formation of larger bubbles which exceed the critical size for floating up. These larger bubbles containing molecular hydrogen float up and out of the melt.

A high content of hydrogen in the melt, on one hand, decreases the threshold of cavitation [18], on the other hand, increases the hydrogen diffusion into the bubbles and facilitates the formation of larger bubbles. Thus, it results in a better degassing effect, as shown in our experiments.

The removal of hydrogen can also be reflected in the microstructure beside the density of the solidified sample, as shown in Fig. 7.10 and Fig. 7.11. In the non-treated alloys, many pores can be clearly observed, especially in the alloy which was exposed to the vapor-enriched furnace atmosphere (Fig. 7.11 (a)). With the help of ultrasound, the volume percentage of the pore decreased dramatically.

Figure 7.10 The grain structure in the middle of the solidified samples in case of dry atmosphere: (a) without UST; (b) UST for 30 s; (c) UST for 60 s; (d) UST for 5 min and (e) UST for 10 min.

As for the grain size, as illustrated in Fig. 7.12, a coarsening effect can be observed for long enough UST times. It is worth noting that the melt temperature at the start of UST was 720 ˚C in all experiments. However, although the sonotrode was preheated before being inserted into the melt and the crucible was placed in a resistance furnace during early stage of UST, the melt temperature dropped to 670 ˚C after UST for 30 and 60 s. Longer ultrasonic processing times (300 and 600 s) of the melt resulted in a re-increase of melt temperature to around 790 ˚C due to the ultrasonic energy input in the melt. It is suggested that for long time treated alloys, the effect of ultrasonic grain refinement was fully cancelled by the increased melt temperature.
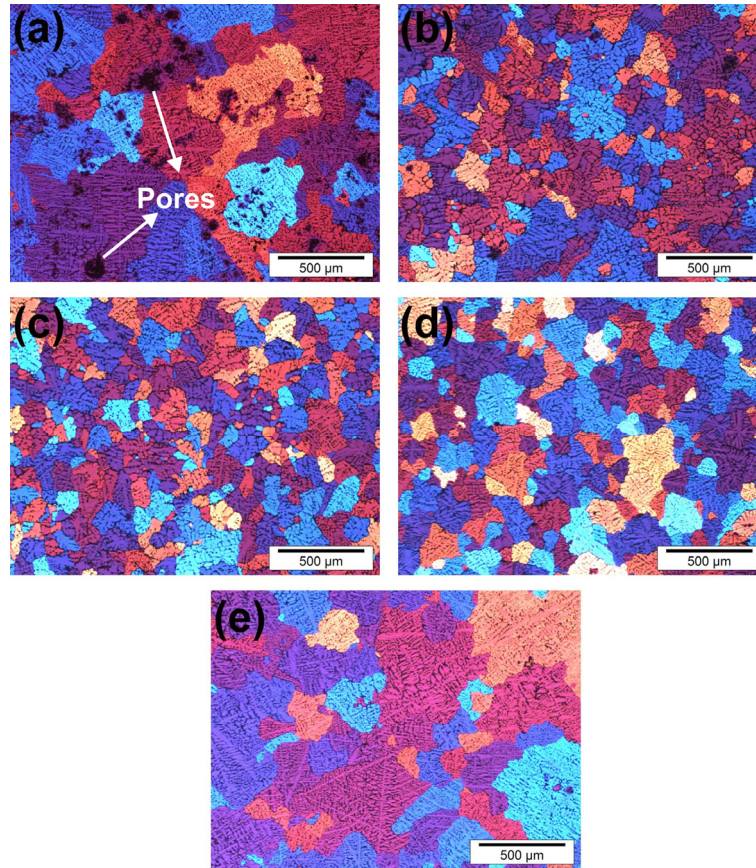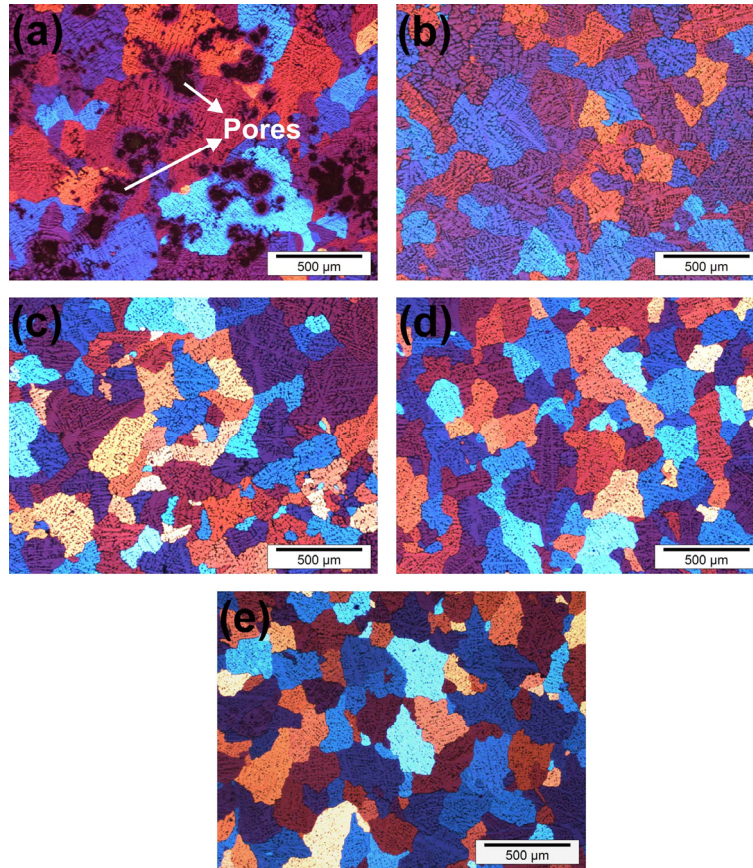
141

Figure 7.11 The grain structure in the middle of the solidified samples in case of vapor enriched atmosphere: (a) without UST; (b) UST for 30 s; (c) UST for 60 s; (d) UST for 5 min and (e) UST for 10 min.
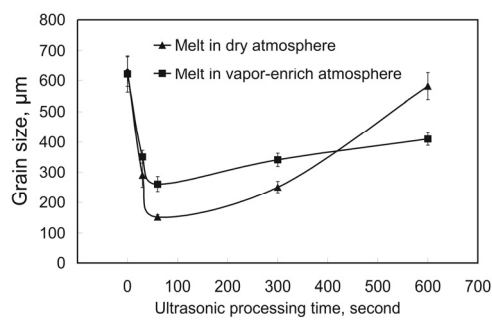

Figure 7.12 The effect of ultrasonic processing time on grain size in the Al- 4 wt% Mg alloy.

7.5 Conclusions

In this chapter, preliminary studies on the effect of ultrasonic processing on fluidity and degassing were presented. The results show that UST improves the melt fluidity through two factors. The first one is the well known ultrasonic grain refinement, which increases the solid fraction at coherency temperature during solidification of aluminum alloys. The second one is the improved wettability and dispersion of oxide inclusions in the melt after UST. The promising degassing effect caused by UST has been confirmed in our research. A relatively higher content of initial hydrogen in the melt results in better degassing effect. This might be related to the mechanism of ultrasonic degassing. A high content of hydrogen in the melt, on one hand, decreases the threshold of cavitation, on the other hand, accelerates the diffusion of hydrogen to the bubbles and facilitates the formation of larger bubbles. In order to have the optimized degassing effect, the required ultrasonic processing time should reflect the melting and casting conditions. Thus, a well planned study on different parameters (initial hydrogen content, casting temperature, melt volume, etc) is necessary before to consider the application of ultrasonic degassing into industry. A too short or excessive ultrasonic processing time will result in insufficient degassing or coarsening of grain structure.

References:

[1] G.I.Eskin, *Ultrasonic Treatment of Light Alloy Melts*. 1998, Amsterdam: Gordon and Breach Science Publishers.

[2] O.V.Abramov, *Ultrasound in Liquid and Solid Metals*. 1994, Boca Raton,FL: CRC press.

[3] A.M.Samuel and F.H.Samuel, *J. Mat. Sci.*, 1992. **27**: p. 6533-6563.

[4] J.Campbell, *Castings Practice: The 10 Rules of Casting*. 2004, Oxford, U.K.: Butterworth-Heinemann.

[5] S.S.Wu, L.F.Liu, Q.Q.Ma, Y.W.Mao, and P.An, *China Foundry*, 2012. **9**(3): p. 201-206.

[6] G.I.Eskin, *Ultrason. Sonochem.*, 1995. **2**(2): p. 137-141.

[7] H.Puga, J.Barbosa, E.Seabra, S.Ribeiro, and M.Prokic, in *Fourth International Conference on Advances and Trends in Engineering Materials and their Applications*. 2009: Hamburg.

[8] A.R.NajiMeidani and M.Hasan, *J. Mat. Proc. Tech.*, 2004. **147**: p. 311-320.

[9] G.I.Eskin, *Ultrason. Sonochem.*, 2001. **8**(2): p. 319-325.

[10] H.B.Xu, Q.Y.Han, and T.T.Meeka, *Mater. Sci. Eng. A*, 2008. **473**: p. 96-104.

[11] AMS, ed. *Metals Handbook, vol. 15: Casting, 9th ed*. Vol. 15. 1988, Materials Park, OH, ASM International. 459.

[12] S.Sánchez, E.Velasco, P.D.Zambrano, and J.L.Cavazos, *Mater. Sci. Forum*, 2006. **509**: p. 159-164.

[13] Y.D.Kwon and Z.H.Lee, *Mater. Sci. Eng. A*, 2003. **360**: p. 372-376.

[14] M.DiSabatino, *Fluidity of Aluminum Foundry Alloys*. 2005, Norwegian University of Science and Technology.

[15] M.DiSabatino and L.Arnberg, *Int. J. Cast Metals Res.*, 2005. **18**: p. 181-186.

[16] H.B.Xu, X.G.Jian, T.T.Meek, and Q.Y.Han, *Mater. Lett.*, 2004. **58**(29): p. 3669-3673.

[17] H.Puga, J.Barbosa, E.Seabra, S.Ribeiro, and M.Prokic, *Mater. Lett.*, 2009. **63**(9-10): p. 806-808.

[18] O.V.Abramov, *Ultrasonics*, 1987. **25**: p. 73-82.

Chapter 8

Concluding remarks

8.1 Concluding remarks

Casting properties are of great importance in the production of aluminum alloys, since they do not only determine whether a successful casting can be achieved with required mechanical properties, but also strongly influence the behavior and properties of aluminum products during and after downstream processing. The objective of the research presented in this thesis is to study the casting properties under the ultrasonic processing in aluminum alloys. Two questions were in focus of this thesis: how does ultrasonic processing affect the casting properties in aluminum alloys and what is the mechanism behind it.

To solve these queries, a systematically study was preformed in order to reveal the effect of ultrasonic processing on casting properties in aluminum alloys. Several features under ultrasonic processing, such as grain structures, size and distribution of intermetallics, macrosegregation in large-scale casting billets, thermal contraction during and after solidification, the fluidity of molten alloy and porosity in as cast products were presented and discussed in this thesis.

One of the most promising effects of ultrasonic processing in aluminum alloy is ultrasonic-aided grain refinement. Our results show that in the aluminum alloys containing transition metals Zr and Ti, the primary intermetallics can be refined dramatically when UST is applied in the temperature range of their primary solidification. It is suggested that both the cavitation-induced fragmentation and the nucleation of primary intermetallics should be considered for explaining the formation of fine primary intermetallics under UST. These refined particles may be involved in a solidification process as nucleation sites and promote the grain refining effect by heterogeneous nucleation under proper casting condition. Whether those particles would result in further grain refining effect in aluminum alloys depends on the undercooling achieved during solidification. The grain refining effect occurs when the undercooling is large enough to activate those refined primary intermetallics. The required undercooling is a function of the crystal structure of the substrate (which characterizes the potency of the grain refiner) and its size (which characterizes the possibility of the free growth).

In the aluminum alloys of eutectic systems, such as in the Al-Mn, Al-Fe and Al-Si alloys, ultrasonic processing is found to facilitate the refinement of primary particles. However, these primary particles have little effect on the refinement of Al grain structure. A significant grain refinement only appeared when ultrasonic processing was performed in the temperature range of primary α-Al phase formation and a relatively long-term treatment is necessary. The cavitation-assisted fragmentation effect of primary α-Al phase is suggested to be the main reason for grain refinement in the aluminum alloys of eutectic systems. Structure coarsening effect caused by ultrasonic processing can be found when UST was applied close to eutectic temperature, for instance, the coarsening of grain structure in near eutectic Al-Mn and Al-Fe alloys, and the coarsening of eutectic phase in the Al-Si alloys. The decreased undercooling caused by UST (extra ultrasonic energy input or enhanced nucleation of primary phases with latent heat evolution) and obstruction of the interdependent relation of nucleation and growth between eutectic phases are suggested to be the main reasons.

146

In order to lay the foundation for industrial application of ultrasonic processing, several ultrasonic parameters were studied as well. Through this research, several suggestions for industrial application of ultrasonic processing in terms of grain refinement can be presented as follows:

(1) A minimum amount of Zr (>0.18 wt %) is necessary for a good ultrasonic refining effect. However, excessive Zr will result in the presence of large particles, visible by optical microscopy, which are considered to be detrimental to the mechanical properties of aluminum alloys. Thus, the composition range 0.18-0.25 wt% Zr is suggested for ultrasonic-aided grain refinement. This amount of Zr is already sufficient for a good grain refining effect without any risk of including too large primary intermetallic particles.

(2) The use of highest ultrasonic power available from the equipment is suggested for obtaining a better effect of grain refinement in the alloys containing Zr and Ti, unless the introduction of ultrasonic energy causes the undesired increase of the melt temperature.

(3) For treating large amounts of melt encountered in industrial castings, it is suggested to place the sonotrode in relative narrow spaces, such as in the launder, to ensure all the melt flows close to it and is treated by ultrasound.

(4) The application of UST to the melt at low enough temperature is recommended to optimize the grain refinement. The sonotrode is not necessary to be located very close to the solidification mold because the effect of ultrasonic processing on the melt remains for a certain time after the end of UST and will still influence the solidifying microstructure.

Based on our results reported above, an extra study of the ultrasonic processing in DC casting was performed. The application of UST in the launder with optimized baffle design resulted in a grain refining effect in DC casting billets, while the distribution of alloy elements in DC casting billet also can be influenced by application of UST in the hot top. However, the limitation of our laboratory scale ultrasonic setup restricted upscaling of the effects, since it could not provide enough powerful streaming as would be required in large scale DC casting. Therefore, an extended analysis was performed using different melt feeding schemes in real industrial DC casting billets in order to simulate the application of powerful UST at different positions in the liquid pool during DC casting. The experimental and computer simulation results showed that the modification of flow patterns and the geometry of the sump caused by different melt feeding scheme resulted in significant changes in the distribution of grain structures and macrosegregation across the billet diameter. This research provides us with very useful information that if the UST could be powerful enough and placed in proper positions of liquid pool during DC casting, the flow patterns in the liquid and slurry zone, even the geometry of the sump can be optimized in the way suitable for controlling macrosegregation and structure. In this case, both grain refinement effect and uniform distribution of alloying elements in the billets can be achieved through ultrasonic processing in DC casting.

The contraction of aluminum alloys has a decisive effect on the quality of casting products. In this thesis, the effect of ultrasonic processing on the contraction behavior of aluminum alloys during and after solidification was studied as well. The results show that the UST resulted in the decreasing of the contraction onset temperature and the amount of thermal

147

contraction during solidification. The suggested mechanism is related to ultrasonic-aided grain refinement and the gas evolution under the ultrasonic processing. Grain refinement caused by UST may also be responsible for the apparent decrease of the thermal contraction coefficient at high temperature close to non-equilibrium solidus. At lower temperature in the solid state, UST has no obvious effect on the thermal contraction coefficient.

The study of other casting properties under ultrasonic processing, such as fluidity and porosity, were also presented in this thesis. The results show that UST improved the melt fluidity through two factors. The first one is the well known ultrasonic-aided grain refinement, which increases the solid fraction at coherency temperature during solidification of aluminum alloys. The second one is the improved wettability and dispersion of oxide inclusions in the melt after UST. The promising degassing effect caused by UST had been confirmed in our research. A relatively higher content of initial hydrogen in the melt results in better degassing effect. A high content of hydrogen in the melt, on one hand, decreases the threshold of cavitation, on the other hand, accelerates the diffusion of hydrogen to the bubbles and facilitates the formation of larger bubbles.

8.2 Outlook

This study has shown a promising application prospect of ultrasonic processing in aluminum alloys. Nonetheless, the study also faced some important problems. One of the problems encountered is the lack of direct observation and measurements of the interaction between ultrasound and growing crystals/bubbles in the liquid melt and during solidification. This is largely because of the complexity of the cavitation process and the non-transparent nature of aluminum melt. In this thesis we formulate the most logical mechanisms based on experimental observations of the grain structure, the distribution of intermetallics and other final properties after solidification. These observations give only indirect indications of the reactions taking place in the melt. Therefore, a more complete understanding of ultrasonic processing in aluminum alloys can be achieved by using in-situ techniques, which provide direct observation of the solidification processing under ultrasonic processing, although the limitation of the sample size and the method of introduction of ultrasonic processing during in-situ observation in the melt might be challenging.

Another shortage of this thesis is that most of experiments are preformed in laboratory scale. Ultrasonic processing usually results in significant effects when it is used for treating small volume of the melt. However, these effects have been shown to be weakened in large scale application, for instance, the presented results on DC casting trials under ultrasonic processing. Therefore, further study on large scale industrial application is suggested both through the experiment and computer simulation, with the aim of improving the effectiveness and efficiency of ultrasonic processing in large volumes of aluminum alloys.

Finally, the results of the extended research using different melt feeding schemes in industrial scale DC casting in Chapter 5 is worth paying more attention. This research provides us a possibility for controlling macrosegregation and structure in DC casting billets through ultrasonic processing. Therefore, the further analysis of the application of powerful ultrasonic processing in the liquid pool during DC casting is recommended.

Summary

This thesis presents a systematic research on ultrasonic processing during the casting of Al alloys. The principle of ultrasonic processing is introduction of acoustic waves with a frequency higher than 17 kHz into liquid metal. Several promising beneficial effects caused by ultrasonic processing in Al alloys were demonstrated and analyzed, mainly through experimental research.

The primary objective of this study was to achieve a more complete understanding of ultrasonic-aided grain refinement. Cavitation-assisted fragmentation of primary phases is considered as the main mechanism of grain refinement caused by the introduction of ultrasonic waves in liquid metal. Depending on the Al alloy systems, the primary phases can be intermetallics or Al dendrites. When ultrasonic processing is applied in the solidification ranges of these primary phases, the growing crystals will be fragmented due to the cavitation.

In the Al alloys containing Zr and Ti, the refined primary intermetallics, e.g. Al_3Zr in the studied alloys, can evolve during further solidification under proper casting conditions into nucleation sites, which promotes the grain refinement. There are four factors acting in achieving the optimum grain refining effect in Al alloys with Zr and Ti under ultrasonic processing. Firstly, the amount of Zr should be sufficient to produce primary intermetallics and the ultrasonic processing should be applied in the temperature range of their formation to assure their refinement. Secondly, Ti should be added and be dissolved in Al_3Zr so that the nucleating undercooling during solidification will be adequate to the size of intermetallics. And thirdly, other solute elements should contribute to this grain refinement by restricting the growth of Al grains. Last but not least, the melt undercooling should be large enough to turn the refined intermetallics or other potent substrates into nucleation sites during solidification.

In the Al alloys of eutectic systems, the fragmentation of primary Al dendrites is considered as the main reason for ultrasonic-aided grain refinement. The refinement of primary particles in Al-Mn, Al-Fe and Al-Si alloys can be achieved by ultrasonic processing, but these primary particles have little effect on the refinement of Al grain structure.

The effects of the parameters of ultrasonic processing on the as-cast microstructure were studied as well in order to determine optimum conditions for industrial application. The power of an ultrasonic generator, initial sonotrode temperature, melt temperature, holding time after ultrasonic processing and cooling rate during solidification were the process parameters that were experimentally studied in Al alloys containing Zr and Ti. The results show that smaller grains can be obtained by increasing the power of the ultrasonic generator, decreasing the initial sonotrode temperature and melt temperature, or cooling faster during solidification. The holding time after ultrasonic processing has minor effect on the microstructure. Based on these observations, several suggestions for industrial application of ultrasonic processing in terms of grain refinement are made and the preliminary research of ultrasonic processing during pilot-scale DC casting is presented in this thesis.

The thesis also presents an extended analysis on the microstructure and macrosegregation in industrial DC casting billets of AA7050 cast using different melt feeding schemes. The aim of this study was to simulate the application of powerful ultrasonic processing at different positions in the liquid pool during DC casting. Experimental and computer simulation results show that the modification of flow patterns and geometry of the sump caused by changing the melt feeding scheme results in significant differences in the grain structures and macrosegregation profile across the billet diameter. This research provides us with the very useful information that if ultrasonic processing is powerful enough and the sonotrode is placed at proper positions in the liquid pool during DC casting, the flow patterns in the liquid and slurry zone, and even the geometry of the sump can be optimized in the way suitable for simultaneously controlling macrosegregation and structure.

Other casting properties of Al alloys, such as thermal contraction during and after solidification, fluidity of molten melt and porosity, also have a decisive effect on the quality of casting products. In the second half of this thesis, the influence of ultrasonic processing on these casting properties is investigated using Al-Cu-Zr-Ti or Al-Mg alloys. Results show that ultrasonic processing has several beneficial effects during and after casting, such as reducing the thermal contraction during solidification, improving the fluidity of Al melt and decreasing the hydrogen porosity.

Through the research in this thesis, a promising application prospect of ultrasonic processing is clearly presented. The systematic study of the influence of ultrasonic processing parameters for various casting conditions on the microstructure and casting properties allows us to achieve a better understanding of ultrasonic processing in Al alloy. It provides valuable information for optimization of ultrasonic processing parameters in industrial application.

Samenvatting

Dit proefschrift beschrijft een systematisch onderzoek naar de ultrasone behandeling bij het gieten van aluminium legeringen. De methode van het ultrasoon behandelen is het aanbrengen van geluidsgolven met een frequentie hoger dan 17 kHz in vloeibaar metaal. Door middel van experimenteel onderzoek beschrijft en analyseert het proefschrift enkele veelbelovende voordelen van deze ultrasone behandeling van aluminium legeringen.

Het voornaamste doel van deze studie was om een beter begrip te krijgen van korrelverfijning door middel van een ultrasone behandeling. Fragmentatie van primaire fases door cavitatie wordt beschouwd als het voornaamste mechanisme voor korrelverfijning veroorzaakt door de ultrasone geluidsgolven in het vloeibare metaal. Afhankelijk van het aluminium legeringssysteem kunnen deze primaire fases beschreven worden als intermetallische verbindingen of aluminium dendrieten. De groeiende kristallen worden gefragmenteerd als gevolg van de cavitatie wanneer de ultrasone behandeling toegepast wordt op de kiemplaatsen van deze primaire fases.

In de aluminium legeringen die Zr en Ti bevatten kunnen de verfijnde primaire intermetallische verbindingen, zoals Al_3Zr in de onderzochte legeringen, zich ontwikkelen tot kiemplaatsen gedurende het verdere stollingsproces mits dit gebeurd onder de juiste voorwaarden tijdens het gieten. Deze nucleatie bevordert de korrelverfijning. Vier factoren zijn van belang voor optimale korrelverfijning in aluminium legeringen met Zr en Ti door middel van ultrasone behandeling. Allereerst moet de hoeveelheid Zr, die in de legering aanwezig is voldoende zijn om primaire intermetallische verbindingen te produceren op voorwaarde dat de ultrasone behandeling is toegepast bij een temperatuur die voor verfijning van de samenstelling zorgt. In de tweede plaats dient Ti toegevoegd te worden en opgelost te zijn in Al_3Zr zodat de onderkoeling tijdens de stolling toereikend is voor de grootte van de intermetallische verbindingen. Ten derde dienen andere opgeloste elementen bij te dragen aan korrelverfijning door het beperken van de groei van de aluminium korrels. Ten laatste dient de afkoelingssnelheid van de smeltbehandeling voldoende groot te zijn om de verfijnde intermetallische verbindingen of andere krachtige substraten, als kiemplaats te activeren.

De fragmentatie van primaire aluminium dendrieten wordt in aluminium legeringen van eutectische systemen beschouwd als de voornaamste aanleiding voor het gebruik van ultrasone geluidsgolven. De verfijning van primaire deeltjes in Al-Mn, Al-Fe en Al-Si legeringen kan met behulp van ultrasone behandeling worden bereikt, maar de invloed van deze deeltjes op de verfijning van de aluminium korrelstructuur is slechts marginaal.

Tevens is het effect van de parameters van ultrasone behandeling op de microstructuur van het gietwerk onderzocht om zodoende de parameters te optimaliseren voor industrieel gebruik. De parameters die experimenteel onderzocht zijn bij aluminium legeringen met Zr en Ti zijn: het vermogen van de ultrasone generator, de begintemperatuur van de sonotrode, de smelttemperatuur, de standtijd na ultrasone behandeling en de afkoelsnelheid gedurende de stolling. De resultaten tonen aan dat kleinere korrels verkregen kunnen worden door het vermogen van de ultrasone generator op te voeren, door de begintemperatuur van de sonotrode en de smelttemperatuur te verlagen, of door de afkoelsnelheid gedurende de

151

stolling te verhogen. De standtijd na ultrasone behandeling heeft slechts een gering effect op de microstructuur. Op basis van deze resultaten geeft het proefschrift enkele aanbevelingen voor het industrieel gebruik van een ultrasone behandeling voor korrelverfijning en de resultaten van de proefopstelling voor ultrasone behandeling tijdens direct chill (DC) gieten.

Daarnaast biedt het proefschrift een uitgebreide analyse naar de microstructuur en macrosegregatie van industriële DC AA7050 billets met verschillende smelttoevoersnelheden. Het doel van dit onderzoek was om de toepassing van krachtige ultrasone behandelingen op verschillende posities in de vloeibare 'sump' gedurende het DC gietproces te simuleren. De resultaten van experimentele- en computersimulaties tonen aan dat de aanpassing van stroompatronen en de geometrie van de 'sump', veroorzaakt door veranderingen in de smelttoevoersnelheid, significante verschillen in korrelstructuren en macrosegregatie profielen over de diameter van de billets tot gevolg hebben. Dit resultaat geeft ons het inzicht dat stroompatronen in de vloeibare en grensgebieden, en de geometrie van de 'sump', desgewenst geoptimaliseerd kunnen worden om tegelijkertijd de macrosegregatie en structuur te beheersen indien ultrasone behandeling krachtig genoeg is en de sonotrode op de juiste posities in de vloeibare 'sump' geplaatst is gedurende het DC gietproces.

Andere eigenschappen van aluminium legeringen, zoals thermische contractie gedurende en na stolling, vloeibaarheid van de smelt en poreusiteit, hebben ook een cruciaal aandeel in de kwaliteit van het gegoten product. In het tweede deel van het proefschrift wordt de invloed van ultrasone behandeling op deze eigenschappen van gietstukken onderzocht met gebruik van Al-Cu-Zr-Ti of Al-Mg legeringen. De resultaten tonen aan dat ultrasone behandeling enkele voordelen kent, gedurende en na het gietproces, zoals het verminderen van thermische contractie gedurende stolling, het verbeteren van de vloeibaarheid van de aluminium smelt en het verlagen van de waterstof poreusiteit.

Het onderzoek in dit proefschrift presenteert een helder en veelbelovend vooruitzicht voor de toepassing van ultrasone behandelingen. De systematische studie van de parameters van ultrasone behandelingen in gietprocessen onder verschillende omstandigheden en de effecten op de microstructuur en de eigenschappen van het gietproces geven een beter inzicht in de ultrasone behandeling van aluminium legeringen. Dit inzicht is in het bijzonder waardevol voor de optimalisatie van de parameters van ultrasone behandeling voor industrieel gebruik.

List of publications

(1) **L. Zhang**, D.G. Eskin, A. Miroux, T. Subroto and L. Katgerman: *Influence of melt feeding scheme and casting parameters during direct-chill casting on microstructure of an AA7050 billet, Metall. Mater. Trans. B,* 2012, 43(6), pp. 1565-1573.

(2) **L. Zhang**, D.G. Eskin, A. Miroux, and L. Katgerman: *Role of solute and transition metals in grain refinement of aluminum alloys under ultrasonic melt treatment, Proc. Of the 13th international conference on aluminum alloys,* 2012, pp. 1389-1394.

(3) **L. Zhang**, D.G. Eskin, A. Miroux, T. Subroto and L. Katgerman: *Effect of inlet geometry on macrosegregation during the direct chill casting of 7050 alloy billets: experiments and computer modelling, IOP Conf. Ser.: Mater. Sci. Eng.,* 2012, 33, 012019, pp. 1-8.

(4) **L. Zhang**, D.G. Eskin, A. Miroux, and L. Katgerman: *Formation of microstructure in Al-Si alloys under ultrasonic melt treatment, Light Metals 2012: cast shop for Aluminum production, TMS2012, Warrendale,* 2012, pp. 999-1004.

(5) **L. Zhang**, D.G. Eskin, A. Miroux, and L. Katgerman: *On the mechanism of the formation of primary intermetallics under ultrasonic melt treatment in an Al-Zr-Ti alloy, IOP Conf. Ser.: Mater. Sci. Eng.* 2011, 27, 01200, pp.1-6.

(6) **L. Zhang**, D.G. Eskin, and L. Katgerman: *Influence of ultrasonic melt treatment on the formation of primary intermetallics and related grain refinement in aluminum alloys, J. Mater. Sci.,* 2011, 46(15), pp.5252-5259.

(7) D.G. Eskin, T.V. Atamanenko, **L. Zhang** and L. Katgerman: *Ultrasonic Treatment of Aluminum Alloys for Grain Refining, Proc. Of the 11th international aluminium conference,* 2010, IOS Press, pp. 281-288.

(8) T.V. Atamanenko, D.G. Eskin, **L. Zhang** and L. Katgerman: *Criteria of Grain Refinement Induced by Ultrasonic Melt Treatment of Aluminum Alloys Containing Zr and Ti, Metall. Mater. Trans. A,* 2010, 41A, pp. 2056-2066.

(9) D.G. Eskin, T.V. Atamanenko, **L. Zhang** and L. Katgerman: *On the mechanism of grain refinement by ultrasonic melt treatment in the presence of transition metals, Light Metals 2010: cast shop for Aluminum production, TMS2010, Warrendale,* 2010, pp. 607-611.

(10) **L. Zhang**, D.G. Eskin, M. Lalpoor and L. Katgerman: *Factors affecting thermal contraction behavior of an AA7050 alloy, Mater. Sci. Eng. A,* 2010, 527, pp. 3264-3270.

Acknowledgements

Four years ago, I never imagined that today I am able to finish this thesis. During four-year's study at Delft University of Technology, I got lots of sincere help and support from many people. Without their efforts, this thesis could not be realized.

First of all, I would like to thank my promoter Professor Laurens Katgerman for his stimulating suggestions and kind encouragements. He impressed me as a gracious supervisor with great wisdom. He always uses a simple example, sometimes even a joke, to let me understand a complicated query and gives me so much confidence.

I always feel extraordinarily lucky to have two wonderful daily supervisors during my PhD study: Professor Dmitry Eskin and Dr. Alexis Miroux. I would like to express my special appreciation to them. Professor Dmitry Eskin brought me into the casting world. He step by step taught me how to perform experiments, analyze data, and write a real scientific paper. One can imagine how hard it could be to teach a person with awful English listening and speaking a complex scientific theory. But Dmitry did it with great patience! I am very grateful for all of his quick feedbacks and guidance during this period. Dr. Alexis Miroux started to supervise me since the third year of my PhD. He accommodated himself on my project quickly and started to guide me effectively. He helped me all the way to overcome the difficulties I faced during the last two years and spent quite a lot of time on discussing with me, reviewing my paper and providing valuable comments.

Other two important persons who deserve special thanks are my supervisors Professor Linzhong Zhuang and Professor Jishan Zhang at University of Science and Technology Beijing, China. Without their support and recommendation, I would not be able to study here, let alone to finish this thesis. They provided me as much help as they can and gave me motivation for the next step.

I would also like to thank our technicians Jan van Etten and Jack Jansen for their kind technical supports in my experiments. Thank you very much for maintaining the casting lab in a good condition, which allowed me to perform my experiments without any problem. Special thanks to Jan van Etten for translating the proposition of my thesis to Dutch. Also many thank to Dr. Tetyana Atamanenko, who did a nice former exploratory research on this topic. This enabled me to have a clear roadmap in this further project.

My thanks are also given to Lambert Schipperheijn, Sander Leeflang, Kees Kwakernaak and Erik Peekstok for their kind helps in my experiments and data analysis. I would also like to thanks our secretaries Olga Wens-van Swol and Annemart Berendse for their kind helps in everything.

Our industrial partner Tata steel and Aleris fully supported our research. Their participation and contribution are greatly appreciated. Dr. Demian Ruvalcaba in Tata steel and Dr. Roger Sauermann in Aleris, thank you very much for your valuable comments and suggestions.

Also I express my appreciation to all of my friends and colleagues at the university. I had a great time working with them, going to lunch with them. Abbas Bahrami, Qingshi Song, Zhan Zhang, Andrea Bojack, Bogdan Necula, Yiangxia Qu, Guoliang Zhu, Jai Gautam,

Curriculum Vitae

Liang Zhang

Born on 26 January, 1985

In JiuJiang, Jiangxi Province, China

➢ **Since 2009**

PhD Candidate at Department of Materials Science and Engineering, Delft University of Technology and **PhD researcher** at Materials innovation institute (M2i), under the supervision of *Prof. L. Katgerman*, *Prof. D. G. Eskin* and *Dr. A. Miroux.*

Major: Materials Science and Engineering

Research Topic: The effect of ultrasonic processing on as-cast properties in aluminum alloys

➢ **2006-2009**

Master and PhD. Candidate of University of Science and Technology Beijing, China (USTB) under the supervision of *Prof. J. S. Zhang.*

Major: Materials Science and Engineering

Research Topic: Preparation technique of high-strength magnesium alloys

➢ **2002-2006**

Bachelor of Engineering, Nanchang University, China (NU).

Major: Materials Science and Engineering